UNIVERSITY OF LEEDS

Studying the uncertainty in Specific Differential Phase (K_{DP}) from weather radar measurements

by

Joshua Mark Ralph-Hampton

Submitted in accordance with the requirements for the degree of Doctor of Philosophy

The University of Leeds
School of Earth and Environment

February 2022

Declaration of authorship

The candidate confirms that the work submitted is his own and that appropriate credit has been given where reference has been made to the work of others.

This copy has been supplied on the understanding that it is copyright material and that no quotation from the thesis may be published without proper acknowledgement.

The only way of discovering the limits of possible is to venture a little way past them into the impossible.

ARTHUR C. CLARKE

Acknowledgements

Firstly, I would like to express my greatest appreciation and thanks to my supervisors Dr Ryan Neely III, Dr David Dufton, and Prof. Alan Blyth, for their support, guidance and enthusiasm without which this research could not have been completed. Your passion, knowledge, and optimism have greatly encouraged me throughout, and helped motivate me to persevere. Thank you for all you have given me throughout the course of my PhD, and particular thanks for the whiskey and the cricket.

I would like to extend my thanks and gratitude to Dr Lindsay Bennett, whose expertise and perseverance kept NXPol-1 going through many challenges. Through terrible weather, relocation, and seemingly everything breaking, your determination to keep the radar going has known no end, and without which my research, and much more, could not happen. Thanks also to the rest of the NCAS radar group, whose thoughts, ideas, and encouragement has helped to keep me going and provided new inspiration when needed.

Special thanks to Alex and Jacob, your friendship has given me the perfect distractions and getaways to help me enjoy all that is going on. I never thought I would have enjoyed racing virtual cars as much as I do, and staying up late far too many times watching American Football, even if I chose to support the Browns.

To my family, Mum, Dad, Martha, and Marie, the love and support you have all given me through these last years and beyond has made this all possible. I know that you are always there for me, always support me, no matter what. I could not have done this without you.

And finally, as C-3PO would say, although I think I refer to a different being, “Thank the maker!”

Abstract

Dual-polarisation weather radars have become more common through the last 15 years, as operational networks in the USA, UK and across Europe have been upgraded with this capability. The distribution of dual-polarisation radars, and their wide spatial coverage, provide a wealth of information for understanding and nowcasting high impact weather, including quantitative precipitation estimation (QPE), hail detection and the potential for use in data assimilation.

One variable from these radars is Specific Differential Phase (K_{DP}). There have been many studies into the uses of K_{DP}, including QPE, hydrometeor classification, and liquid and ice water content estimations, with K_{DP} often preferred over reflectivity based measurements due to being less dominated by larger, but fewer, targets. However, K_{DP} is not directly measured by the radar, rather it is derived from the total phase shift measured, which has a number of other contributors including backscatter differential phase and noise, and therefore estimating K_{DP} is difficult.

To explore the uncertainty associated with this estimation, a number of different estimation methods are studied, and it is shown they all struggle to accurately estimate K_{DP}, especially when there is noise present. Being a difference between two orthogonal observations, K_{DP} is affected by the viewing geometry of non-spherical targets. This is confirmed through observations of ice hydrometeors through a range of elevation angles, and the effect of elevation angle on K_{DP} is shown through a hydrometeor classification algorithm, where adjusting K_{DP} at high elevation angles changes the output from the algorithm. Finally, output from a radar forward operator using high resolution model simulations is compared with radar observations to study how well simulated fields can recreate estimated K_{DP}. The generalisation of ice in microphysical schemes and the forward operator mean that radar signatures present in the observations are not replicated in the output of the forward operator.

Contents

List of Figures

List of Tables

Abbreviations & Symbols

CEDA	Centre for Environmental Data Analysis
CR-SIM	Cloud-resolving model Radar Simulator
c	Speed of light
D	Diameter of hydrometeors
e	Partial pressure of water vapour
FAAM	Facility for Airborne Atmospheric Measurement
f	Radar transmit frequency
IWC	Ice water content
$\|K\|^2$	Dielectric constant of scatterers
K_{DP}	Specific differential phase
LDR	Linear depolarisation ratio
LWC	Liquid water content
l_x	Loss in x polarisation due to attenuation
l_r	Range weighting function loss
M	Number of pulses
NWP	Numerical weather prediction
NCAS	National Centre for Atmospheric Science
n	Refractive index
P	Air pressure
P_y^t	Power transmitted in y polarisation
P_{xy}	Power received at radar in x polarisation after transmission in y polarisation
PPI	Plan position indicator
QPE	Quantitative precipitation estimation
R	Rainfall rate
RHI	Range height indicator
r_0	Distance between radar and targets
s_{xy}	Backscattering coefficient of a scatterer, backscattered polarisation is x, incident polarisation is y
T	Temperature
T_s	Pulse repetition period
UKMO	UK Met Office
v_{DOP}	Doppler velocity
WRF	Weather Research and Forecasting
Z_{xy}	Radar reflectivity measured in x polarisation after transmission in y polarisation in logarithmic units

z_{xy}	Radar reflectivity measured in x polarisation after transmission in y polarisation in linear units
Z_{dr}	Differential reflectivity in logarithmic units
z_{dr}	Differential reflectivity in linear units
δ	Backscatter differential phase
θ	Radar elevation angle
θ_1	Radar beamwidth
λ	Radar wavelength
ρ_{hv}	Co-polar correlation coefficient
σ_v	Spectrum width
σ_{vn}	Normalised spectrum width
τ	Pulse width of transmitter
Φ_{DP}	Differential phase due to forward propagation
φ	Phase of beam returned from scatterer
φ_{aa}	Total phase shift in a polarisation
Ψ_{DP}	Total differential phase shift
ψ_0	Radar system phase difference

Chapter 1

Introduction

One of the largest areas of uncertainty in numerical weather forecasts comes from a poor understanding and parameterisation of ice, and ice microphysics, and how that contributes to precipitation (Morrison et al. 2015). In-situ measurements of ice are difficult and expensive to obtain; however, remote instruments such as radars can provide an insight into the ice regions of clouds (Bukovčić et al. 2018). Weather radars give a unique opportunity to observe the growth, development and maturity of clouds, by providing large spatial coverage and high temporal resolution of the column of atmosphere surrounding each radar. This wealth of data has resulted in the detection of hail in convective storms (Aydin et al. 1986), the identification of the melting layer (Austin and Bemis 1950), the development of rain rate estimates (Meneghini 1978), and improved issuance of severe storm warnings (Simmons and Sutter 2005).

Until recently, most operational weather surveillance radars transmitted an electromagnetic beam with a single polarisation. This allows for detection of objects and the reflectivity of those objects, which is related to their size; however, it can not measure the variety of shapes seen in ice. The research, development, and operational implementation of dual-polarisation radars overcomes this deficiency, resulting in measurements of differential reflectivity, correlation coefficients between the two polarisations, phase measurements, and depolarisation ratios, all containing information about the size and shape of what is being observed. This additional polarimetric information has huge, although yet not fully realised, potential to improve forecasts, severe weather detection, and our microphysical knowledge of cloud development (Zhang et al. 2019; Ryzhkov et al. 2020).

1.1 Specific Differential Phase

One of the variables returned from the observations of dual-polarisation radars is Specific Differential Phase (K_{DP}), which is a calculation of how the phase of the electromagnetic wave changes in each polarisation as it travels through targets away from the radar (Seliga and Bringi 1978). As a comparison between the two orthogonal polarisations, K_{DP} is related to the size, shape, and number of of the targets the beam propagates through. K_{DP} has benefits over other radar measurements due to being unaffected by radar calibration issues or partial attenuation, and therefore can be used to help correct other radar measurements for attenuation. Thus, K_{DP} appears favourable for estimations of precipitation and microphysical retrievals when compared to reflectivity measurements (Aydin et al. 1995; Bukovčić et al. 2018); however, there are uncertainties associated with measurements of K_{DP} which, if not accounted for, can negatively affect these retrievals. These uncertainties are relatively unexplored and need to be addressed if the potential of K_{DP} is to be realised.

1.2 Polarimetric Observations of Ice

Ice crystal habit type can be particularly sensitive to small changes in the temperature and ice saturation, as extensively shown by Bailey and Hallett (2009). With the additional size and shape information offered by polarimetric data, our understanding of the current state of the atmosphere, and the microphysical processes that determine the life cycle of ice particles, can develop, in turn improving how ice crystal properties are represented in microphysical schemes in numerical weather prediction models.

However, there are factors which limit the use of the polarimetric observations. One is in the verification of our interpretation of the observations. There is limited data available of ice within clouds, as in-situ measurements can only take place at high-altitude observations, for example at Jungfraujoch in the Alps (Lloyd et al. 2015) or during flight campaigns. These campaigns are relatively few in number, can not cover extensive spatial areas, and are prone to instrumental measurement error (Field et al. 2003; McFarquhar et al. 2007). Another limitation is errors in the radar measurements. Issues surrounding the calibration of the radar, accuracy of processing algorithms, and a lack of knowledge in how the radar beam interacts with melting hydrometeors, result in uncertainties that make comparisons between radar data, microphysical measurements, and theory challenging (Zhang et al. 2019). A mismatch in the sampling volume between radar and aircraft measurements can also cause issues when trying to use po-

larimetric observations. Radar measurements cover a large three-dimensional volume, typically observing the same location every 5-10 minutes, whereas an aircraft takes measurements along a line in space, and depending on the flight schedule may not return to the same location.

Pronounced radar signatures, including an increase in K_{DP}, occur where dendritic crystals are growing, crystals which grow in areas of enhanced ice supersaturation at around -15 °C (Kennedy and Rutledge 2011), and in regions where secondary ice production may be occurring, typically between -3 °C and -8 °C (Sinclair et al. 2016), where observed ice crystal concentrations are orders of magnitude greater than the concentration of ice nucleating particles. Hydrometeor classification algorithms are able to distinguish different types of ice crystals based on the polarimetric data. K_{DP} is particularly useful for studying ice regions in clouds, with areas of enhanced K_{DP} at both locations of dendritic crystal growth and secondary ice production.

Dendritic ice crstyals are ice crystals that have a hexagonal core, with branches extending out from the core, which themselves have branches protruding outward (Botta et al. 2013) . The presence of dendritic ice crystals as suggested by increased K_{DP} at around -15 °C is well correlated with increased surface precipitation in stratiform weather (Bechini et al. 2013). Secondary ice production is a term for a number of mechanisms that produce new ice crystals in the presence of preexisting ice without the action of ice nucleating particles, which accounts for the difference between observed ice concentrations and those predicted from primary ice nucleation (Field et al. 2017). Accurate representation of ice concentrations in numerical weather prediction is important with the development of double-moment microphysics schemes (for example (Thompson et al. 2008)) and for understanding the evolution of some types of clouds (for example Connolly et al. (2006)).

1.3 Model Representation

Another obstacle in the use of polarimetric data to improve numerical weather prediction is the difference in how models and radars represent hydrometeors. Microphysical schemes used in models have increased in complexity, with many schemes now predicting mixing ratio and number concentration for hydrometeors (Thompson et al. 2008; Morrison et al. 2009). The number of hydrometeor species being predicted by the microphysics schemes, plus the processes being modelled, are also increasing, adding to the complexity of the schemes, but also increasing the need for them to be well

constrained. While the large amount of data provided by dual-polarisation radars at first seems optimal for this, the problem is that radars do not measure mixing ratio and number concentration of different hydrometeor species, instead they provide reflectivity and phase measurements of all the objects within a volume. Therefore, an operator is needed to convert from one to the other. Forward operators take the model information and transform it into radar observations, while an inverse operator would go from radar observations to model data (Zhang et al. 2019). However, the accuracy of these operators is not fully known, and add another element of error into comparing the data. Additionally, different sizes, shapes and habit types of ice crystals result in different radar measurements; however, most microphysical schemes group ice into one category. This difference between radar observations and model output increases the challenge and uncertainty in forward operators.

1.4 Thesis Outline

This thesis will focus primarily on assessing the uncertainty in the measurements of one polarimetric variable, specific differential phase (K_{DP}), and how well it can be estimated through a forward operator from numerical weather prediction models. In Chapter 2, the underlying concepts of dual-polarisation radar measurements are outlined, along with a brief introduction to polarimetric radar forward operators. The data and methods used throughout this thesis are described in Chapter 3. Chapter 4 tests and compares a number of different methods used to estimate K_{DP}, highlighting strengths and weaknesses of each method. This chapter uses first an artificial truth, and then observational data, to study how well each of the chosen methods estimates K_{DP}. Chapter 5 studies how estimated K_{DP} can change due to the unique geometry of radar observations, through looking at observations through the full range of radar elevation angles, being the first study to compare such observations with the theoretical relation between K_{DP} and elevation angle. Finally, in Chapter 6, K_{DP} from the radar is compared against K_{DP} as estimated from a numerical weather prediction model through a forward operator, looking at how well models and forward operators replicate radar observations. All of these sections highlight uncertainties with K_{DP}, and steps to overcome them, and their results are summarised in Chapter 7.

Chapter 2

Background

2.1 Weather Radar

During the Second World War, inspired by the need to detect enemy planes and submarines, technology developed to improve radars. Previously, these were large devices with poor resolution, however the development of the magnetron meant radars could be made much smaller, and could easily be moved or mounted on aeroplanes. These radars were detecting large, unknown patches, which could block any signal from enemy aircraft. It was deduced that these patches were precipitation, and meteorologists, who were working as part of the military due to the strategic advantage of weather forecasts, realised the potential. Research groups were set up to further explore the use of radar in weather, the beginning of radar meteorology.

A radar works by transmitting an electromagnetic wave of known frequency, duration, polarisation and power, focused in a single direction by an antenna, and then measuring the power and the phase of the signal that is detected from backscattering from targets. For weather surveillance radars, these targets are typically hydrometeors. One of the most significant recent advancements in radar technology is the ability to send and receive signals in two polarisations, known as dual-polarisation radar (Kennaugh 1952; Huynen 1970; Boerner et al. 1981; Ryzhkov et al. 2005b). Dual-polarisation radars transmit waves with orthogonal polarisations, typically one in which the oscillation of the wave is parallel to the ground (horizontal polarisation) and the other with an oscillation perpendicular to the ground (vertical polarisation); however, use of circular polarisation has also been tested (e.g. Bebbington et al. (1987); Holt and McGuinness (1990)). While single-polarisation radars could only measure the power and phase of the returned signal in one polarisation, dual-polarisation radars measure these signals from two, often orthogonal polarisations, allowing for a range of new measurements

which compare the power and phase of the return signals in each polarisation, resulting in better discernment of the size and shape of targets.

When the radar observes a volume, the signal returned to the radar is a combination of individual returns from all scatterers within that volume. The returns from each individual scatterer interfere with each other, either constructively or destructively, and the radar measures the amplitude and phase of the returned signal. However, if the targets are moving, then a second observation would measure a different amplitude and phase. Therefore, multiple observations are needed to reduce uncertainty in polarimetric measurements. However, taking multiple measurements of the same location takes time, and as such results in a trade off between increasing statistical accuracy, the maximum range that can be measured along a beam, and the temporal resolution of radar measurements; increasing one of these will need a compromise from one or both of the others.

The frequency of the transmitted wave impacts what can be usefully detected by the radar. In the Rayleigh scattering regime, where the scatterer is much smaller than the wavelength, the volume scattering coefficient is proportional to the sixth power of the diameter of the scatterer divided by the fourth power of the wavelength (Fabry 2015). This leads to two important factors: larger targets scatter much more than smaller ones, so the signal received by the radar is dominated by larger targets, and for a given size of scatterer, a shorter wavelength will produce greater scattering. However, large scatterers may fall outside of the Rayleigh regime, into the Mie scattering regime. Here, the volume scattering coefficient fluctuates depending on the exact value of wavelength and object size, and the power of the returned wave no longer increases with object size. At X band frequency (8-12 GHz), formulae derived for the Rayleigh regime are valid for rain with a maximum diameter of 2.3 mm and graupel/hail with a maximum diameter of 3 mm (Table 5.1 in Ryzhkov and Zrnić (2019)). Kumjian et al. (2018) show the impact of Mie scattering resonance for larger hydrometeors, and the differences in the resonance response for small changes of frequency within the X band range.

Measurements from a radar fall into one of three general categories - power based, Doppler based, or phase based.

2.1.1 Power Measurements

A form of the weather radar equation is given as

$$P_{hh} = \left(\frac{\pi^3 P_h^t g^2 c \tau \theta_1^2}{2^{10} \lambda^2 l_r \ln 2} \right) \frac{|K|^2}{r_0^2 l_h^2} \, \bar{z}_{hh}, \tag{2.1}$$

where P_{hh} is the co-polar power received in the horizontal polarisation. The terms inside the brackets are constants or radar dependent variables, all of which need to be well known - P_h^t is the power transmitted in the horizontal polarisation, g is the antenna gain, c is the speed of light, τ is the pulse width of the transmitter, θ_1 is the beamwidth, λ is the radar wavelength, and l_r is the range weighting function loss. The terms outside the brackets are dependent on the path of the beam and the targets encountered - r_0 is the distance between the radar and the targets, $|K|^2$ is the dielectric constant of the scatterers, l_h^2 is the loss due to attenuation along the path, and $\bar{z}_{hh}$ is the radar reflectivity factor. $|K|^2$ varies significantly depending on what the scatterer is, with a factor of 5 between liquid water and solid ice (Table 3.1 in Fabry (2015)). Therefore, $|K|^2$ is replaced with the dielectric constant of liquid water ($|K_w|^2$), and $\bar{z}_{hh}$ becomes the equivalent radar reflectivity factor, as the exact nature of the scatterers are usually unknown. This equation forms the basis for all power-based observations and analysis from weather radar.

Radar Reflectivity

Rearrangement of equation 2.1 shows that reflectivity in a given polarisation is proportional to the power received in that polarisation divided by the power transmitted in a given polarisation, i.e. $\bar{z}_{hh} \propto P_{hh}^r / P_{hh}^t$. In practice, the effects due to attenuation are ignored, resulting in the measured, attenuated reflectivity $z_{hh} = \bar{z}_{hh} / l_h^2$. Correcting for attenuation is not a trivial undertaking, and there is much research into how this should be done (for example Vulpiani et al. (2008) and Gu et al. (2011)).

This equation gives reflectivity in linear units, that is $mm^6 m^{-3}$. Using these units gives a large range of values for reflectivity, from 0.01 $mm^6 m^{-3}$ in liquid cloud to over 10^6 $mm^6 m^{-3}$ in hail (Fabry 2015). For convenience, reflectivity is often expressed in units of decibels, such that

$$Z_{hh} = 10 \, log_{10}(z_{hh}). \tag{2.2}$$

Using equation 2.2, the liquid cloud has a reflectivity of -20 dBZ, and hail now has a reflectivity of 60 dBZ.

Reflectivity is related to the drop size distribution as:

$$Z = \int D^6 N(D) dD, \tag{2.3}$$

where $N(D)$ is the number of hydrometeors with a diameter of D in a unit volume. Reflectivity is dominated by larger droplets, for example while one droplet with a diameter of 2 mm has a similar reflectivity factor to 64 drops with a diameter of 1 mm (Fabry 2015), there is a greater volume of water in the 64 smaller drops, and the one larger drop would need to fall 8 times faster than the 64 smaller ones to produce the same rain rate. This highlights some of the problems in using reflectivity to estimate rain rate. Marshall and Palmer (1948) showed that the rain rate varies with drop size distribution. As a result, a number of relationships exist between Z and R, mostly of the form $Z = aR^b$. These include the Marshall-Palmer Z-R relationship $Z = 200R^{1.6}$, and the NEXRAD (USA national radar system) default $Z = 300R^{1.4}$. However, there are many different versions of this equation, slightly different due to different dominant dynamical and microphysical processes occurring in different regions (Stout and Mueller 1968; Smith and Krajewski 1993; Amitai 2000; Kim et al. 2021). Figure 2.1 shows some plots of radar reflectivity from the NCAS X-band mobile radar.

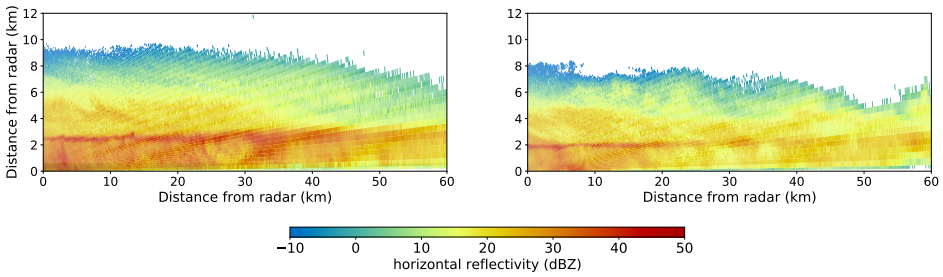

Figure 2.1: RHI plots of reflectivity from NCAS X-band mobile radar. The plot on the left shows data from 11:36:14 UTC 17 May 2017, the plot on the right from 17:02:31 UTC 14 February 2018.

There are a number of factors that can negatively affect the quality of reflectivity measurements. Firstly, the radar needs to be correctly calibrated, identifying the unknown system error caused by the transmitter, receiver, and antenna, otherwise biases introduced in the reflectivity measurements will be propagated through to rainfall estimations. Calibration needs to be done on a regular basis, as environmental and instrument changes will affect the correction. A number of methods exist for calibration, including measurement of a known signal source, using a highly reflective metal sphere as a known reference target (e.g. Sarabandi and Ulaby (1990); Yin et al. (2019)), or self-consistency

with differential reflectivity and specific differential phase (e.g. Gourley et al. (2009); Trabal et al. (2014); Louf et al. (2019)). Secondly, if the radar uses a radome, moisture on the radome can bias reflectivity measurements by a few dB (Schneebeli et al. 2012; Mancini et al. 2018). This bias is variable, changing with the weather. Use of hydrophobic paint on the radome can significantly reduce the effect (e.g. Dietrich and West (1988)), or data-based consistency methods can highlight biases caused by a wet radome. Thirdly, obstacles such as buildings or terrain can block the radar beam. In the case of total blockage, there is no signal received by the radar down-radial from the blockage, and no data can be collected. However, if the blockage is only partial, then the radar will still receive some signal, although significantly weaker beyond the blockage. Reflectivity can be corrected by estimating the degree of blockage, and adding a correcting factor to the measured reflectivity (equations 6.50-6.52 in Ryzhkov and Zrnić (2019)). Finally, attenuation of the beam can significantly reduce the power of the radiation received by the radar. As previously mentioned, correcting for attenuation is not straightforward; however, with no correction, precipitation estimates could be severely biased. There are a number of algorithms that attempt to correct for reflectivity, using other measurements such as differential phase measurements or those from another radar. However, these methods work best in rain, and correcting for attenuation through the melting layer is still a significant challenge.

While all of these factors negatively impact on power-based measurements, they do not have the same impact on phase-based measurements (with the exception of total blockage of the beam). Therefore, phase measurements such as Specific Differential Phase are being used to replace reflectivity in rain rate measurements (Timothy et al. 1999; Paulitsch et al. 2009), and to correct reflectivity measurements for these issues (Overeem et al. 2021).

Differential Reflectivity

Dual-polarisation radars can measure received power for each polarisation state they can receive. The ratio of the power returns in the horizontal and the vertical polarisations gives differential reflectivity, that is

$$\bar{z}_{dr} = P^r_{hh}/P^r_{vv}. \tag{2.4}$$

Ignoring attenuation again, this becomes

$$z_{dr} = z_{hh}/z_{vv}, \tag{2.5}$$

or after converting to decibel units,

$$Z_{dr} = 10 \log_{10}(z_{hh}/z_{vv}) = Z_{hh} - Z_{vv}. \tag{2.6}$$

As reflectivity gives information about the size of the detected targets, differential reflectivity therefore is related to the axis ratio of targets, where a differential reflectivity of 0 dB means that $Z_{hh} = Z_{vv}$, and the measured targets are spherical. Typical values of differential reflectivity range from 0 dB to 5 dB in rain, increasing with increasing drop size, from 0 dB to 3 dB in snow. Non-meteorological targets can return larger differential reflectivity values, ranging from -4 dB to 6 dB (Fabry 2015). As most hydrometeors fall with their longest axis horizontal due to aerodynamic stability in free fall (Willmarth et al. 1964; Westbrook et al. 2010), differential reflectivity is rarely less than 0 dB in the atmosphere, with the exception of vertically-orientated ice crystals which can occur in the presence of a strong electric field within a cloud, or occasionally in hail Aydin and Zhao (1990); Picca and Ryzhkov (2012). As hail tumbles as it falls, and can fall with its largest axis vertical, differential reflectivity values in hail are often low. Near zero differential reflectivity in the region of high horizontal reflectivity (i.e. $Z_{hh} > 50\,dBZ$) is a good indicator of the presence of hail. Conversely, insects are much longer in the horizontal than the vertical, and can appear to the radar as elongated water drops. They have a small reflectivity due to their size, but very high differential reflectivity, distinguishing them from light rain and drizzle (Melnikov et al. 2015). Some examples of differential reflectivity measurements are shown in figure 2.2.

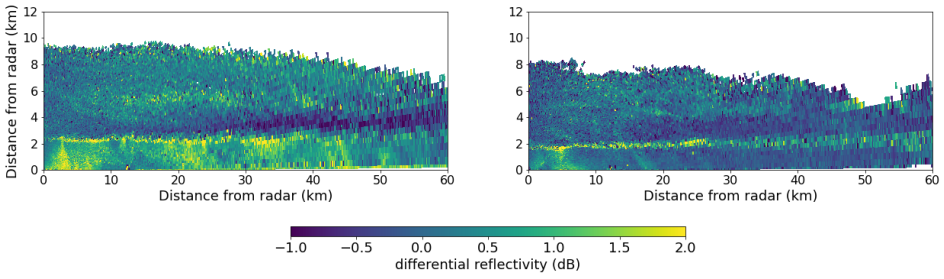

Figure 2.2: RHI plots of differential reflectivity from NCAS X-band mobile radar. The plot on the left shows data from 11:36:14 UTC 17 May 2017, the plot on the right from 17:02:31 UTC 14 February 2018.

Unlike reflectivity, differential reflectivity is not usually affected by absolute miscalibration of the radar transmitter or receiver, as the miscalibration affects both polarisations (Kumjian 2013); however, biases in the radar hardware toward one polarisation need to be corrected before quantitative use of Z_{dr}. Z_{dr} calibration is often done through mea-

surement of light rain when the radar is vertically pointing, as when viewed from below falling raindrops appear spherical, thus Z_{dr} should be 0 dB (Gorgucci et al. 1999a; Marks et al. 2011). There are a number of options for Z_{dr} calibration for radars incapable of pointing vertically, including consistency checks with reflectivity in light rain (Tabary et al. 2011), using dry aggregated snow (Ryzhkov and Zrnić 1998b; Ryzhkov et al. 2005a), using clear-air echoes associated with Bragg scattering (Melnikov et al. 2011), and calibration using ground clutter (Borowska and Zrnic 2012). Z_{dr} can also be affected by anisotropic beam blockage, resulting in more of one polarisation being blocked than another, which would bias measurements along the radial beyond the blockage (Kumjian 2013).

Linear Depolarisation Ratio

If a scatterer is not symmetric along the axis of polarisation of the received radar beam, some of the scattered signal will be in the orthogonal polarisation, that is the beam will have been depolarised. Linear depolarisation ratio (LDR), is the ratio between the power of the cross-polar and the co-polar signal measured at the radar (whereas differential reflectivity is the ratio between orthogonal co-polar signals). For a beam transmitted with horizontal polarisation, that is the ratio between the received vertical polarisation and the horizontal polarisation,

$$LDR = 10\log\left(\frac{\langle|s_{hv}|^2\rangle}{\langle|s_{hh}|^2\rangle}\right), \tag{2.7}$$

where s_{ab} is the backscattering coefficient of a scatterer with the backscattered radar beam with a polarisation and incident beam with b polarisation (horizontal h or vertical v), and the angled brackets denote the ensemble average representation of all scatterers in the measured volume. Applications of LDR include identifying electrification in thunderstorms (Sokol et al. 2020), estimating the shape of ice hydrometeors (Matrosov et al. 2001), and distinguishing between stratiform and convective rainfall (Sandford et al. 2017).

As the strength of the cross-polar signal is much smaller than that of the co-polar signal, LDR values are very small. Targets such as small raindrops may produce LDR of -35 dB, with the highest values rarely exceeding -15 dB for non-symmetric targets such as hail (Fabry 2015; Doviak and Zrnić 1993).

For a radar to measure a cross-polar signal, it needs to be able to transmit just one polarisation at a time, and then observe the backscattered signal in two planes. Most

weather radars transmit in both polarisations simultaneously, meaning that the received signal for a given polarisation is the co-polar signal from that polarisation combined with the cross-polar signal from the orthogonal polarisation. As the cross-polar signal is much weaker than the co-polar signal, and the co-polar and cross-polar signals can not be separated, it is assumed that the entire return is co-polar, and therefore LDR can not be measured. Some radars can transmit in one polarisation and listen in both, before switching to transmit in the orthogonal polarisation, and thus allowing for measurement of LDR (for example radars that are part of the UK Met Office radar network (Harrison et al. 2015)); however, this will result in noisy estimates of the other dual-polarisation variables, which depend on simultaneous transmission for accurate measurement, and it requires a polarisation switch in the transmission to switch between polarisations, resulting in a more complex radar design and faster wear rate (Doviak et al. 2000). Therefore, LDR is rarely measured by weather radars (e.g. NEXRAD and the French operational weather radar network (Gourley et al. 2006) do not measure LDR).

Co-polar Correlation Coefficient

The co-polar correlation coefficient (ρ_{hv}) is a measure of how much the returns of the horizontal and vertical polarised beam fluctuate through successive measurements of the same volume, that is

$$\rho_{hv} = \frac{\langle s_{vv} s_{hh}^* \rangle}{\langle |s_{hh}|^2 \rangle^{1/2} \langle |s_{vv}|^2 \rangle^{1/2}}. \tag{2.8}$$

A coefficient of 1 indicates there is no change in the observed targets with time, which would be the case if all scatterers were frozen in place, or if the returned signal is dominated by one scatterer, such as a building or tower which produces a strong return. Values less than 1 occur when scatterers are moving through the volume, or change orientation or shape.

Co-polar correlation coefficient is therefore a measure of the diversity of the targets within the measured volume, including characteristics such as the size, shape, orientation and phase. In pure rain, changes in shape and orientation are small. Values of ρ_{hv} in pure rain are very high, typically >0.98 (Kumjian 2013; Ryzhkov and Zrnić 2019). Values are slightly below 1 due to advection of raindrops through the volume, small changes in orientation and shape (Ryzhkov and Zrnić 2019), and slight wobbling as the raindrops fall (Kumjian 2013), resulting in small changes between measurements. However, theoretical values of ρ_{hv} drop to 0.93 at C band due to resonance effects of

droplets greater than 5 mm (Ryzhkov and Zrnić 2019).

Ice and snow can also have a high co-polar correlation coefficient; however, changes in phase or ice crystal habit can reduce this. Most notable is in the melting layer, where snow is melting into rain. Due to the large variability in the size, shape and phase of hydrometeors in this region, ρ_{hv} can reduce to 0.8 (Fabry 2015). Compared to the high values observed in rain and snow on either side, this change in ρ_{hv} stands out, making for easy visual detection of the melting layer in ρ_{hv} plots. Other causes of low ρ_{hv} can include insects and lofted debris associated with tornadoes; in both cases there is a large amount of movement by scattering objects, and measuring ρ_{hv} at 0.4 is common. This is one of the key parts of the Tornado Debris Signature, used by the USA National Weather Service to confirm the presence of a tornado through polarimetric radar data (Ryzhkov et al. 2005c; Houser et al. 2016).

2.1.2 Doppler Measurements

Doppler measurement capability started to be added to weather radars in the 1990s, and since has become the standard. In addition to reflectivity, these radars can also measure the radial velocity of targets, which can be useful in detecting severe weather conditions, storm motion and the presence of strong mesocyclones that could produce a tornado (Rinehart and Garvey 1978; Trapp et al. 2020).

Doppler velocity

Doppler velocity uses the principle of Doppler shift to measure the movement of targets toward or away from the radar. As targets move within the volume measured, the phase of the returned electromagnetic beam shifts slightly between successive measurements of the same location, depending on the mean movement of the targets. By measuring these small changes in phase from successive returns, the Doppler velocity is retrieved:

$$\frac{d\varphi}{dt} = -\frac{4\pi f n}{c} v_{DOP}, \tag{2.9}$$

where $d\varphi$ is the change in the phase of a target between successive transmitted pulses, dt is the time between those successive pulses, f is the radar transmit frequency, n is the average refractive index along the path, c is the speed of light, and v_{DOP} is the Doppler velocity of the target. By being able to measure the rate of change of the phase, Doppler velocity can be estimated, with assumptions made about the refractive

index of air. The refractive index depends on pressure, temperature, and humidity, and for microwaves in the lower atmosphere can be estimated by

$$n = 1 + 10^{-6}\left(\frac{0.776P}{T} + \frac{3.73 \times 10^3 e}{T^2}\right), \tag{2.10}$$

where P and e are air pressure and partial pressure of water vapour in Pascals, and T is temperature in Kelvin. The refractive index is approximately 1.0003 near sea level, and decreases with height.

The change in phase that can be measured by a radar ranges from -π to π. Rearrangement of Equation 2.9 therefore gives a maximum range of measured Doppler velocity as

$$v_{DOP} = \pm\frac{c}{4fndt}, \tag{2.11}$$

known as the Nyquist velocity. The Nyquist velocity can be increased by decreasing the time between measurements; however, this results in a decrease to the maximum range that can be observed from the radar. This trade off between maximum detectable range and maximum unambiguous velocity, and what the operator expects to observe, needs to be considered when setting up a radar.

Doppler velocity is typically defined using the convention of positive velocity for movement away from the radar, and negative velocity for toward; however, not all radars follow this convention. The Doppler velocity also gives just one part of the three-dimensional wind field; however, use of overlapping measurements from another viewing angle can give the entire wind field structure. One method of gaining this extra viewing angle is by using another Doppler radar (Trapp et al. 2020). The area over which the three-dimensional wind field can be retrieved can be increased by increasing the distance between the radars to a point, but increasing the distance will reduce the resolution of the retrievals, and reduce the ability to retrieve the wind field in the lowest scans.

Spectrum Width

The many targets present within a volume measured by the radar do not all move with the same speed. This means that the Doppler velocity measurements fluctuate slightly with successive measurements, as the interference pattern changes slightly between returns. The rate at which fluctuations occur is the spectrum width, and is a measure of the spread in the Doppler velocity of the targets in the measured volume. Wind

shear, differences in fall speeds of hydrometeors, changes of hydrometeor orientation, and turbulence can all contribute to spectrum width (Li and Zhang 2022). Turbulence is a main contributor to spectrum width (Istok and Doviak 1986), and as such spectrum width is often used to detect unsafe regions for aircraft (Fang et al. 2004).

2.1.3 Phase Measurements

While Doppler retrievals consider the change in the measured phase of the radar beam through successive measurements of the same volume, the phase of the beam also changes as the beam propagates away from, and then back toward, the radar. Consideration of how the phase changes due to propagation for each orthogonal component of the beam results in a number of different variables.

Total Differential Phase Shift

As the radar beam passes through and encounters targets, the phase of each polarisation of the electromagnetic beam changes. The total differential phase shift is given as

$$\Psi_{DP} = \varphi_{HH} - \varphi_{VV}, \tag{2.12}$$

where Ψ_{DP} is the total differential phase shift, and φ_{HH} and φ_{VV} are the total phase shifts in the horizontal and vertical polarisations respectively. There are three components that influence phase shift along the radial. Firstly is the phase difference between the two polarisations at the point of transmission from the radar (ψ_0), which is a function of hardware and software in the radar, is unique to each radar, and is often taken as the total phase shift measured by the radar at range zero. Secondly, a shift in phase occurs in the backscattered wave upon reflection from the scatterers (δ, Trömel et al. (2013)). Thirdly, there is a change in phase due to changes in forward propagation velocity as the beam moves through changing mediums (Φ_{DP}, Kumjian (2013)).

Total differential phase shift can therefore also be written as

$$\Psi_{DP} = \Phi_{DP} + \delta + \psi_0, \tag{2.13}$$

Ψ_{DP} generally increases with range; however, large changes of backscatter differential phase or interactions with some scatterers can change that.

While Ψ_{DP} is the quantity measured by the radar, it is the individual components that

are of greater interest, usually the range derivative of Φ_{DP}, and so these variables are often packaged with measured variables (such as reflectivity) in radar data files.

Backscatter Differential Phase

As the radar beam is scattered back to the radar from targets, each polarisation of the beam may encounter a shift of phase due to the scattering interaction. The magnitude of backscatter differential phase depends on the wavelength of the radar beam and temperature, as well as hydrometeor type and size. For S-band radars, backscatter differential phase is negligible except for the very largest hydrometeors (raindrops greater than 7 mm diameter and melting hailstones greater than 5 cm diameter, Ryzhkov and Zrnić (2019)); however, for C-band and X-band it becomes non-negligible for smaller raindrop sizes (4.5 mm and 2.5 mm respectively), with the magnitude of backscatter differential phase dependent on both drop size and temperature (Trömel et al. 2013).

Backscatter differential phase is negligible at S-, C- and X-band for most ice hydrometeor types, due to the small imaginary part of the ice dielectric constant (Trömel et al. 2013). However, large, dry hailstones have notable backscatter differential phase, which can be much greater, or negative at certain sizes, for wet hailstones (Aydin et al. 1991). Within the melting layer, backscatter differential phase can be significant. Modelling work by Trömel et al. (2013) showed that the backscatter differential phase within the melting layer can reach 1°, 2°, or 4° at S-, C- and X-band respectively; however, the model they used assumed mixed phase particles do not interact, and wet snowflakes do not aggregate. Including aggregation in the model is challenging; however, further work by Trömel et al. (2013) with disdrometer data suggests that backscatter differential phase can reach 10° in the melting layer, which is a large contribution to the Ψ_{DP} measurements.

2.1.4 Specific Differential Phase

As the radar beam propagates forward through scatterers, the phase of each polarisation of the radar beam changes due to the beam travelling through changing mediums. This differential phase shift due to forward propagation (Φ_{DP}) accumulates with range from the radar. Thus, it is more useful to know how this phase shift changes along the range of the radar beam. Specific Differential Phase (K_{DP}) is defined as the one-way range

derivative of the forward propagation differential phase shift,

$$K_{DP}(r) = \frac{1}{2}\frac{d\Phi_{DP}(r)}{dr}. \tag{2.14}$$

Specific differential phase is the difference between the change in phase of the horizontal polarisation and vertical polarisation due to passing through targets (Seliga and Bringi 1978). Hydrometeors falling under the influence of gravity are generally oriented with their longer axis roughly parallel to the ground (Westbrook et al. 2010). This means that the horizontal component of the radar beam has a greater encounter with the hydrometeors than the vertical component, therefore a greater phase shift in the horizontal than the vertical, resulting in positive specific differential phase. The two main exceptions to this are in clouds with strong electric fields, within which ice crystals can be vertically oriented along the electric field, and large hail which tumbles as it falls, resulting in near zero or negative specific differential phase. Specific differential phase tends to increase with increasing hydrometeor size; however, due to the dielectric constant of ice being lower than that of water, K_{DP} increases slower with diameter in snow than in rain (Ryzhkov and Zrnić 2019). Figure 2.3 shows some examples of K_{DP} estimation.

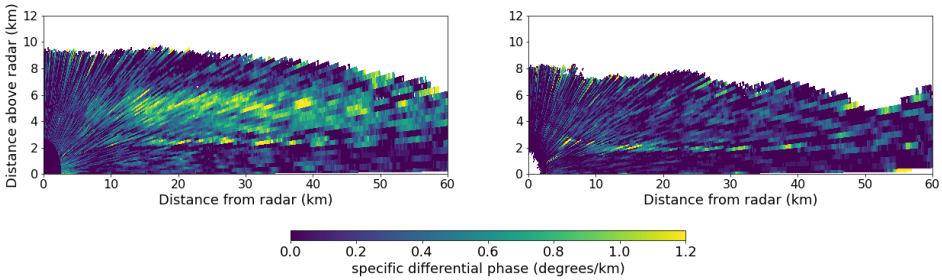

Figure 2.3: RHI plots of specific differential phase from NCAS X-band mobile radar. The plot on the left shows data from 11:36:14 UTC 17 May 2017, the plot on the right from 17:02:31 UTC 14 February 2018.

As mentioned in Section 2.1, the observation of a volume of scatterers needs multiple measurements to reduce statistical errors. The standard deviation for Φ_{DP} is given by equation 6.80 in Ryzhkov and Zrnić (2019) as

$$SD(\Phi_{DP}) = 30.3\left(\frac{\rho_{hv}^{-2} - 1}{\sigma_{vn} M}\right)^{1/2} \tag{2.15}$$

which propagates through to the standard deviation for K_{DP}, which from equation

6.82 in Ryzhkov and Zrnić (2019)

$$SD(K_{DP}) = \frac{\sqrt{3}\, SD(\Phi_{DP})}{M_r^{3/2}\Delta r} \tag{2.16}$$

where $\sigma_{vn} = 4\sigma_v T_s/\lambda$ is the normalised spectrum width, σ_v is the spectrum width λ is the wavelength in metres, T_s is the pulse repetition period in seconds, M is the number of pulses, and M_r is the number of range samples used in the K_{DP} estimation. Increasing the number of pulses, the pulse repetition period, and the distance over which K_{DP} is estimated all decrease the standard deviation of the K_{DP} estimation; however, as discussed in section 2.1, these have the trade off of reducing the maximum range from the radar of measurement or increasing the time that lapses before the next measurement of that region. For the NEXRAD radars, with a spectrum width of 1 ms^{-1} and ρ_{hv} of 0.99, the standard deviation in Φ_{DP} is 3.1 °, which equates to a standard deviation in K_{DP} of 0.17 $°km^{-1}$ when reflectivity is less than 40 dBZ (K_{DP} is estimated over 25 range gates with a spatial resolution of 0.25 km, T_s is 0.003 seconds, and M is 17). Given that, especially for S band radars, K_{DP} can often be less than 1 $°km^{-1}$, this is a large statistical error, and motivates further need to reduce the effect of noise in K_{DP} estimations.

Specific differential phase may be closely, although not exactly, related to rainfall rate. Computations based on a large set of drop size distributions measured by disdrometers in Oklahoma (Schuur et al. 2005) suggest K_{DP} is proportional to the number of drops of diameter D multiplied by D^a, where a is between 4.3 and 4.9, slightly dependent on wavelength and drop size. For rainfall rate, a is approximately 3.67, and for reflectivity a is equal to 6 (Fabry 2015; Ryzhkov and Zrnić 2019). A number of studies have used K_{DP} to measure rainfall rate, either solely or in combination with Z and/or Z_{dr} (Aydin et al. 1995; Zrnic and Ryzhkov 1996; Matrosov et al. 2006). K_{DP}-R relationships are also more favourable over Z-R relationships because, being a phase measurement, K_{DP} is not dependent on the strength of the return signal, and so is immune to radar miscalibration, attenuation, and partial beam blockage (Kumjian 2013). These benefits of K_{DP} can also help correct reflectivity for attenuation (Vulpiani et al. 2008; Snyder et al. 2010), or to help with radar calibration (Gourley et al. 2009; Trabal et al. 2014; Louf et al. 2019). However, for C-band radars (4-8 GHz frequency), resonance-sized raindrops (5-7 mm in diameter) result in different values of K_{DP} depending on the temperature, and so can cause erroneous estimations of rainfall. These temperature-dependent resonance effects are also present at X-band for raindrops 3-5 mm in diameter, although the difference due to temperature is less at X-band than C-band, and at S-band it is negligible for raindrops with a diameter less than 7 mm

(Ryzhkov and Zrnić 2019).

As well as rainfall rate, K_{DP} has the potential to provide accurate estimations of microphysical properties such as liquid and ice water content (LWC and IWC). The same disdrometer data set from Oklahoma (Schuur et al. 2005) showed that $K_{DP} = a\,LWC^b$, where a and b are dependent on radar wavelength. For frozen hydrometeors, Vivekanandan et al. (1994) and Ryzhkov et al. (1998) showed that K_{DP} is almost linearly proportional to IWC, assuming that K_{DP} is positive. In the case where K_{DP} is negative, K_{DP} can provide information about electrical processes in clouds (Ryzhkov and Zrnić 2019).

Specific differential phase is also used in hydrometeor classification (e.g. Liu and Chandrasekar (2000); Thompson et al. (2014)). An example of this is in the detection of hail. As mentioned previously, K_{DP} is close to zero in regions of hail, but is large for heavy rain, whereas for both hail and heavy rain reflectivity is often greater than 50 dBZ (Liu and Chandrasekar 2000). Large K_{DP} values can also be found in the ice region where dendritic ice crystals are dominant, and where secondary ice production may be occurring (Field et al. 2017).

Determining K_{DP} is not necessarily as straightforward as taking the derivative of the measured total differential phase shift. Even if the backscatter differential phase is negligible, the differential should be calculated from measurements over a number of resolution volumes in order to reduce errors and noise (Hubbert and Bringi 1995). In the case where backscatter differential phase is not negligible or is unknown, it must be accounted for and removed from the measured Ψ_{DP} profile to obtain a Φ_{DP} for calculating K_{DP}. Failure to correctly remove backscatter differential phase results in incorrect estimations of K_{DP}, and these errors will be propagated through to any products in which K_{DP} is used in their derivation, for example rainfall rate (Trömel et al. 2013). A number of different algorithms have been developed to estimate K_{DP}, with different levels of complexity and with different assumptions made (e.g. Hubbert and Bringi (1995); Vulpiani et al. (2012); Schneebeli et al. (2014)). The estimation methods used in this thesis are described in in Section 3.3.

2.2 Numerical Weather Prediction

Mathematical models and equations governing the physics of the atmosphere are used to predict the weather, taking the initial weather conditions and calculating their change in time. This was first published in 1922 by Lewis Fry Richardson (Richardson and

Lynch 2007), using a simplified set of equations with a hydrostatic approximation, which took a period of months, between trips to the front line toward the end of World War 1 (Thompson 1983), to produce a six hour forecast for two places in central Europe. However, his forecast calculated the surface pressure would change by 145 millibars, due to extrapolating an instantaneous pressure tendency and not correctly accounting for natural atmospheric damping through gravity waves (Lynch 2006). Numerical weather prediction (NWP) became more successful and useful with the development of computers in the 1950s. The Met Office produced their first numerical prediction in 1952 using a computer at the University of Cambridge, before installing their own computer in 1959. These forecasts used a 12 x 8 grid, with 260 km between grid spaces, and required four hours to complete a 24 hour forecast (Met Office 2019).

Numerical weather prediction today is much more complex than in the 1950s. Increased knowledge, more data for initial conditions, and powerful computers, have resulted in improved accuracy, higher resolution, and longer lead times for weather forecasts. Rather than using a 12 x 8 grid, modern NWP models can cover the entire globe, with a horizontal resolution of 10 km rather than 260 km, and lead times extended from 1 day up to 16 (Kerns and Chen 2014; ECMWF 2021). Models covering local regions use even higher resolution, with the Met Office using 1.5 km over the British Isles (Ballard et al. 2015). More surface weather stations are collecting data which is used to initialise the models, and more data from within the atmosphere becoming available from aircraft and satellites. Ever-growing computers are needed to support all this, and the Met Office has received £1.2 billion of funding from the UK government for a new supercomputer, which will be in the top 25 of all supercomputers in the world (Met Office 2021).

2.2.1 Microphysics Schemes

Numerical weather prediction models are not written as one block of code, rather different pieces of code relating to different processes are written separately, and can be developed and improved, and in some cases completely changed, without re-writing the entire NWP model. One of these areas, and one of the greatest challenges for atmospheric modelling, is cloud microphysics (Igel et al. 2015). The microphysics scheme controls clouds and precipitation within the model, with different schemes incorporating different levels of complexity. Atmopsheric models can not represent individual cloud and precipitation particles due to the huge number of them ($1m^3$ of cloudy air could contain a few million cloud droplets), and so only a selection of cloud and precipitation

features are predicted (Grabowski et al. 2019). Most microphysics parameterisations are bulk schemes, meaning they assume a shape for the hydrometeor size distribution, and predict one or more moments of the distribution, whereas bin microphysics schemes predict the evolution of the size distribution, but they are computationally expensive, making them infeasible for forecasting applications. However, the additional detail achieved by bin schemes means they are often used as a benchmark for testing bulk schemes (Grabowski et al. 2019). Figure 2.4, taken from Grabowski et al. (2019), highlights the differences between bulk and bin microphysics schemes, and the increasing complexity of those schemes.

Bulk microphysical schemes can generally be classified into one of two categories. Single moment schemes predict the mixing ratios of a number of hydrometeors, representing the size of each hydrometeor class with a defined distribution function (e.g. Lin et al. (1983); Thompson et al. (2004); Straka and Mansell (2005)). Double moment schemes also predict the number concentration of some or all hydrometeor types in the scheme (e.g. Milbrandt and Yau (2005a); Morrison et al. (2005); Thompson et al. (2008)). This gives more flexibility in the size distribution, and allows the mean diameter to change. Despite requiring more computational work, double moment schemes are favoured as the better representation of hydrometeor growth and processes result in significant improvements to predicted surface precipitation and storm evolution (Loftus et al. 2014; Igel et al. 2015).

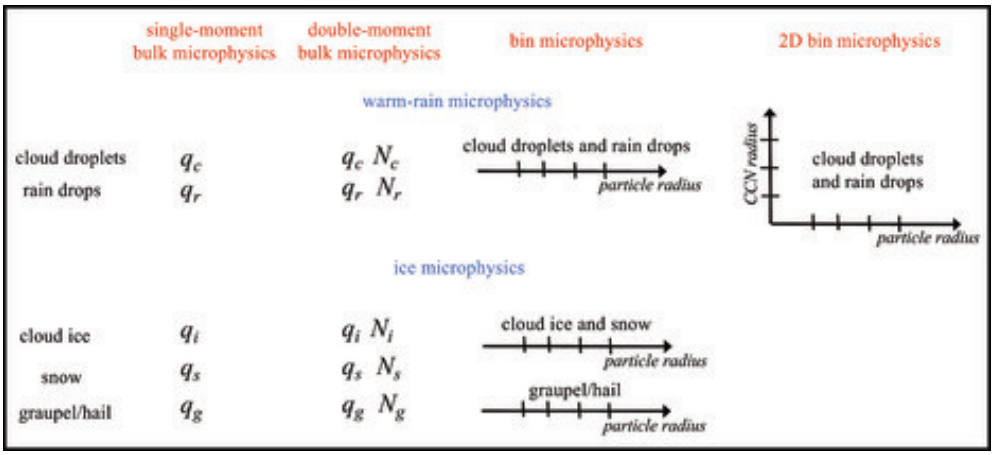

Figure 2.4: Figure 1 from Grabowski et al. (2019): General diagram of the increasing complexity of microphysics schemes. Single-moment bulk microphysical schemes predict only the mass mixing ratios q of certain cloud and precipitation categories, whereas double-moment schemes also predict the number concentration N. Bin microphysical schemes represent a size distribution for each category, with multi-dimensional distributions used if more detail is needed.

A few triple moment bulk microphysics schemes have been developed, with the third moment in these schemes being radar reflectivity (Milbrandt and Yau 2006a,b; Loftus et al. 2014; Loftus and Cotton 2014). The initial studies of these schemes focused on hail in convective storms, and reported promising results with regards to location,timing and size of hail in the studied storms. The Milbrant-Yau scheme has also been tested on an orographic precipitation event (Milbrandt et al. 2008). While the simulated reflectivity structure compared well against the radar observations and the spatial distribution of hydrometeors was realistically simulated, the simulations generally over-predicted the amount of precipitation and snow mass concentration aloft, and under-predicted the pockets of cloud liquid water. While the prediction of an additional moment can further improve the microphysical representivity in the model, this comes at the cost of additional computational time, with Loftus and Cotton (2014) noting that their scheme requires about 30% more computational time compared to a double-moment scheme.

2.2.2 Forward Operators

In the absence of triple moment microphysics schemes, there is no direct way to compare the output from numerical weather prediction models to the observations from weather radar, and even then only reflectivity is available for comparison. Forward operators take the output from NWP models and convert the output to radar observables, and can be expressed either as one value for each radar observable as the radar would measure or separated out for each hydrometeor resolved in the microphysics scheme (examples include Jung et al. (2008); Ryzhkov et al. (2011); Oue et al. (2020)). This information can then be used to optimize numerical weather prediction models through data assimilation; however, this use of polarimetric radar data is still a new area of research, or for improving microphysical parameterisation (Ryzhkov et al. 2020).

With the exception of the bulk adaptive habit model (Harrington et al. 2013), the aspect ratios of hydrometeors are not predicted in NWP microphysics schemes, and neither are the distributions of hydrometeor orientations. While some suggestions have recently been put forward for changing the aspect ratio of melting snowflakes and hail as a function of mass water fraction (Jung et al. 2008; Ryzhkov et al. 2011), generally forward operators make assumptions on the aspect ratio and hydrometeor orientation based on hydrometeor type. The operators also need to account for radar wavelength, elevation angle, the width of the canting angle distribution, and sometimes temperature, before calculating radar observables, either by performing scattering calculations or through the use of lookup tables.

While forward operators can reproduce some polarimetric radar observables, they can not account for all artifacts seen in the radar measurements. Attenuation in each polarisation of the radar beam can be accounted for, and is often returned by the forward operator; however, miscalibration, beam blockage, and the presence of microwave noise from the radar and the atmosphere can not be accounted for, neither can the echoes from non-meteorological sources such as birds and insects, which adds to the complexity in comparing between the model and the radar (Oue et al. 2020; Ryzhkov et al. 2020).

Radar forward operators also can not reproduce all radar signatures just using the data straight from the microphysics schemes. The schemes rarely include any mixed phase hydrometeors, meaning signatures in radar data that are due to melting, for example the radar bright band in the melting layer, are not seen in the output from forward operators. Jung et al. (2008) and Dawson et al. (2014) suggest creating artificial classes to fix this, taking some amount of water and ice from the pure liquid and ice classes to create "melting snow" and "melting hail".

The output from forward operators is dependent on a lot of fine, microscale detail, including information related to the microphysical properties at each grid location (for example, the number and mass concentrations of each hydrometeor type), and how that translates into interactions with a radar beam. Meanwhile, the accuracy of a forward operator output when compared to radar observations is also dependent on the accuracy of NWP models. These models contain uncertainty on a macroscale, such as timing and location of weather, which can be affected by model initial and boundary conditions, as well as the dynamics of the model itself.

Forward operators are key to the potential for using radar observations in data assimilation to initialise NWP model runs (Jung et al. 2008; Xiao et al. 2008). Data assimilation is the process of combining a background state, usually from a previous model run, with new observations, to create the best guess of the current state of the atmosphere to use as initial conditions for starting a new run of the model, while also reducing the associated uncertainty from both the model and the observations. Assimilation of reflectivity and Doppler velocity have been shown to be useful, producing realistic storm-scale structures and helping reduce the spin-up time needed in the model (Sun and Crook 1997; Dowell et al. 2011; Wang et al. 2013); however, reflectivity alone is not sufficient to analyse all the variables included in multi-moment microphysics schemes (Zhang et al. 2019). Polarimetric radar data may help with this, however there needs to be an improvement in how the additional data is assimilated,

and how forward operators and microphysics schemes treat frozen and mixed-phase hydrometeors (Zhang et al. 2019).

Chapter 3

Methods and Data

The primary dataset in this study comes from National Centre for Atmospheric Science's dual-polarisation Doppler mobile X-band radar (NXPol-1), with the observations collected while the radar was based at Chilbolton Observatory (section 3.1). This is supported with model data from the UK Met Office (section 3.2) and the Weather Research and Forecasting (WRF) model (section 3.4), and with observations from the Facility for Airborne Atmospheric Measurements (FAAM) aircraft (section 3.6). Also discussed in this chapter are the forward operator used to convert WRF model data to radar observables in Chapter 6 (section 3.5), and the different methods to estimate K_{DP} which are compared in Chapter 4 (section 3.3).

3.1 NXPol-1 Radar

The main instrument used throughout this study is a movable, dual-polarisation, X-band Doppler weather radar operated by the National Centre for Atmospheric Science (NCAS), which operates with a frequency of 9.375 GHz (a wavelength of 3.2 cm).

The radar is a Meteor 50DX model, manufactured by Selex Systems Integration GmbH, now Leonardo Germany GmbH, with a larger 2.4 m antenna dish. The larger dish means that the half-power beamwidth is reduced to 0.98° compared to 1.5° for the 1.8 m antenna dish model, allowing for higher resolution data collection; however, it means that a radome can not be fitted to the radar. While the issue of radome attenuation is eliminated, the removal of the radome means the radar is more susceptible to damage, both in transit and in high-wind conditions. As such, the radar must be stowed when wind speeds exceed 55 mph, and no data can be collected.

The radar operates in a simultaneous horizontal and vertical polarisation mode, meaning that it both transmits and receives both horizontal and vertical polarisations at the same time, and is capable of scanning at any elevation angle between -1° and 181°, unlike many operational radar systems (for instance, the NEXRAD radars in USA have a maximum elevation angle of 20° in operational usage). With an antenna speed of up to 36° per second and a maximum range of 150 km, the NXPol-1 radar is well suited for the study of cloud evolution, being able to rapidly scan large sections of the atmosphere. A complete description of the NXPol-1 radar can be found in Neely III et al. (2018).

3.1.1 Observations from Chilbolton Atmospheric Observatory (CAO)

The data used through this study were collected when NXPol-1 was located at Chilbolton Observatory (51.145 °N, 1.427 °W), a facility in the south of the United Kingdom that enables research in areas such as atmospheric science, radiocommunications, and astronomy (Goddard et al. 1994; Ladd et al. 2017). NXPol-1 was collecting data at Chilbolton Observatory from 1st November 2016 through to 4th June 2018, and that data can be accessed online through the Centre for Environmental Data Analysis (CEDA) catalogue (Bennett 2020).

3.1.2 Data Collection

While at Chilbolton Observatory, NXPol-1 collected data using both Plan Position Indicator (PPI) scans and Range Height Indicator (RHI) scans. Ten different elevation angles were used through the PPI scans, the lowest being 0.5° and the highest 20° (figure 3.1). While the maximum height of the beam above the radar using an elevation angle of 0.5° is only 1.3 km, the beam reaches a height of 15 km (likely to be near or above the tropopause in the mid-latitudes) at a horizontal distance of just 41 km with an elevation angle of 20°, resulting in a large portion of the surrounding atmosphere being measured.

A few different strategies were used throughout the campaign when conducting RHI scans. One strategy measured just one RHI scan, with an azimuth of 248°, scanning a full cross section through the atmosphere with elevation angles from -1° through to 181°. Another strategy measured 6 'half RHI' scans, with five scans at 1° azimuth increments between 243.5° and 247.5°, plus one scan at an azimuth of 270°, with all

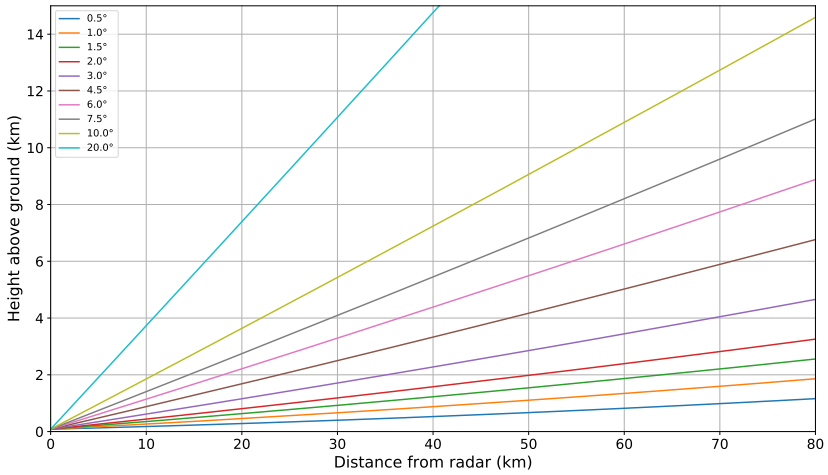

Figure 3.1: Height of radar beam at different elevation angles for increasing distance from the radar.

measuring an elevation range between 0° and 90°. This second strategy was used primarily during the period when the FAAM aircraft was flying, in order to take more measurements in the vicinity of the aircraft.

There are 34 variable fields stored in NXPol-1's processed files:

1. Unfiltered reflectivity from both horizontal and vertical polarisations (dBuZ and dBuZv).

2. Filtered (i.e. clutter-corrected) reflectivity from both horizontal and vertical polarisations (dBZ and dBZv).

3. Differential reflectivity, filtered and unfiltered (ZDR and ZDRu).

4. Radial velocity from both horizontal and vertical polarisations, filtered and unfiltered (V, Vv, Vu, Vvu).

5. Spectral width from both horizontal and vertical polarisations, filtered and unfiltered (W, Wv, Wu, Wvu).

6. Total differential phase, filtered by the Rainbow software (PhiDP).

7. Total differential phase derived by the signal processor, filtered and unfiltered (uPhiDP, uPhiDPu).

8. Specific differential phase derived by the Rainbow software from PhiDP (KDP).

9. Specific differential phase derived by the signal processor, filtered and unfiltered (uKDP, uKDPu).

10. Cross correlation coefficient, filtered and unfiltered (RhoHV, RhoHVu).

11. Degree of polarisation, filtered and unfiltered (DOP, DOPu).

12. Signal Quality Index from both horizontal and vertical polarisations, filtered and unfiltered (SQI, SQIv, SQIu, SQIvu).

13. Signal to noise ratio, from both horizontal and vertical polarisations, filtered and unfiltered (SNR, SNRv, SNRu, SNRvu).

14. Clutter correction ratio from both horizontal and vertical polarisations (CCOR and CCORv).

The data used has been calibrated by Lindsay Bennett, the instrument scientist for the radar, and is made available through CEDA (Bennett 2020).

3.2 Met Office UK Atmospheric High Resolution Model data

Data from a post-processed regional downscaled version of the Unified Model is used to create a temperature field to support the radar observations. This data has an approximate spatial resolution of 0.018°, produces hourly data at the surface and fifteen pressure levels, from 1000 hPa to 30 hPa, and is available on CEDA (Met Office 2016). The radar observations are on a polar coordinate space centred at the radar, and is at higher resolution than the model data, particularly in the vertical direction. To transpose model data from its coordinate space to the radar coordinate space, the following process is used for each radar gate location:

1. The latitude and longitude of the radar gate is found using the Py-ART python package (Helmus and Collis 2016), and from that the closest model grid point in the horizontal plane is obtained.

2. The height of the radar gate is compared to the height of the pressure levels for the model column which contains the nearest grid point, retrieving the temperature in that column for the pressure level directly above and directly below the radar gate. If the radar gate lies below the lowest pressure level, then the 1.5m temperature

is used.

3. Temperature is linearly interpolated between the heights of the pressure levels to the height of the radar gate, to give an estimate for the temperature at that location.

With this process completed for each radar gate location, a linearly interpolated, polar coordinate temperature field is obtained and added to the radar data files. Using temperature as a vertical coordinate, as is done through Chapter 5 means that radar data from different days can be easily compared to each other, as air temperature is one of the factors that influences ice habit (Bailey and Hallett 2009).

3.2.1 Comparison to Radiosonde Observations

To compare the accuracy of this linear-interpolation, radiosonde data collected as part of the PICASSO (Parameterizing Ice Clouds using Airborne obServationS and triple-frequency dOppler radar) campaign are used. Ten radiosondes were launched from Chilbolton Observatory while the radar was collecting data, between 23$^{\text{rd}}$ January and 14$^{\text{th}}$ February 2018. The radiosondes used were RS-41SGP radiosondes made by Vaisala, which use a Platinum Resistor to measure temperature, with an uncertainty of 0.3 °C in sounding data below an altitude of 16 km (Vaisala 2020). These radiosondes took measurements every second during ascent.

Temperature from the radiosonde is compared to the linearly interpolated, polar coordinate temperature field in the radar files, with the nearest radar gate location used for each radiosonde measurement. The results of this are shown in Figure 3.2. The interpolated temperature and the radiosonde-measured temperature agree well, generally within 1 °C up to around -45 °C. The main exception to this is where the radiosonde passes through a front, as the vertical resolution of the provided model data is not sufficient to capture that transition.

A 1 °C error corresponds to a change in height of about 100m in dry conditions, and about 170m in a moist atmosphere. NXPol-1 uses 150m range gates, so when the radar is vertically pointing there may be a 1 °C difference in temperature between the top and bottom of the measurement volume. Similarly, with a 0.98° beamwidth, the width of the measured volume is 100m at a range of almost 5850m from the radar, and 170m at almost 9940m, meaning starting from those distances a 1 °C difference could exist between the top and bottom of the measurement volume when the centre of the radar

beam is parallel to the ground. However, boundaries between hydrometeor types, and the range in which they exist, are not hard and absolute, rather hydrometeors exist across a wide range of temperatures and transition from one to another happens over a few degrees (for example the thickness of the melting layer (Boodoo et al. 2010)), and so a 1 °C temperature error is sufficient for this study.

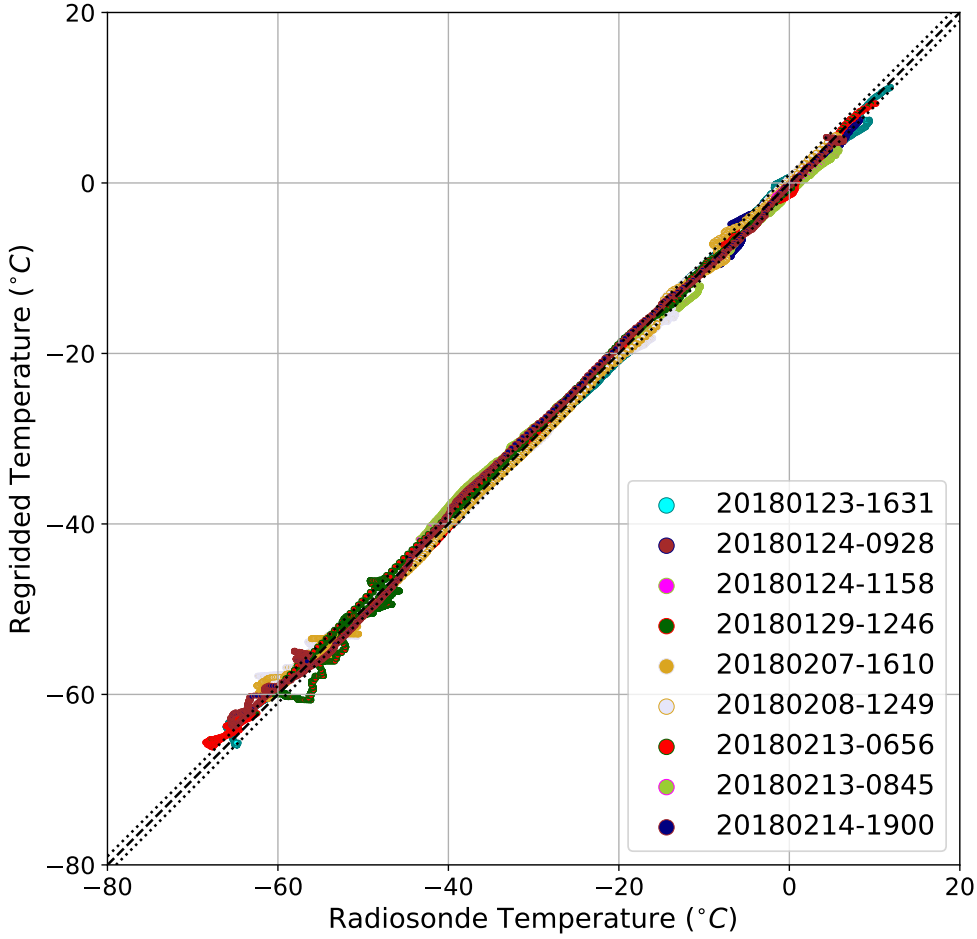

Figure 3.2: Temperature from the Met Office model transposed onto radar grid compared to temperature from radiosondes. The dashed line shows equal temperature between radiosonde and regridded model, with the dotted lines showing ±1 °C.

3.3 K_{DP} estimation methods

As discussed in Section 2.1.4, K_{DP} is not directly measured by the radar, and instead is calculated from the measured total differential phase shift (Ψ_{DP}). There are many different methods in the literature for estimating K_{DP}, with various approaches and

levels of complexity. Some of the methods take the simplest approach possible, by assuming backscatter differential phase (δ) is negligible and then just calculating the slope of the Ψ_{DP} profile over a number of gates. Other approaches include the use of a finite impulse response filter to remove noise and δ from the Ψ_{DP} profile, use of an ensemble of Kalman filters to extract K_{DP} and δ without smoothing the Ψ_{DP} profile, or minimization of a cost function to calculate the most likely profile of K_{DP}.

Eight estimation methods are studied in Chapter 4:

- Rainbow (Hubbert and Bringi 1995; Bringi et al. 2007).
- Bringi (Hubbert and Bringi 1995; Lang et al. 2019).
- Schneebeli (Schneebeli et al. 2013; Helmus and Collis 2016).
- Maesaka (Maesaka et al. 2012; Helmus and Collis 2016).
- Vulpiani (Vulpiani et al. 2012; Helmus and Collis 2016).
- Ryzhkov (Ryzhkov et al. 2005a).
- ωradlib (Vulpiani et al. 2012; Heistermann et al. 2013).
- UK Met Office (UKMO).

The Bringi, Schneebeli, Maesaka, Vulpiani, and ωradlib methods are all available in open source python modules, with the default options being used for all of these methods. The Ryzhkov method was coded based on the description of the method in Ryzhkov et al. (2005b), and the UK Met Office method was provided through personal communication. The Rainbow method is the only one where the underlying code was not available, due to being part of NXPol-1's proprietary signal processing software that produces the radar moments during the operation of the radar.

3.3.1 Rainbow and Bringi Methods

The processing software within NXPol-1 provided by Selex-Gematronik, called Rainbow, includes a method for estimating K_{DP} from Ψ_{DP} based on the method described in Hubbert and Bringi (1995). This method uses an iterative finite impulse response (FIR) filtering method to remove the effects of δ, and is carried out on inidividual range profiles of Ψ_{DP} . This method is described both in Hubbert and Bringi (1995) and in

the handbook as part of the Selex-Gematronik documentation (Bringi et al. 2007).

Before any filtering can take place, Ψ_{DP} is first unwrapped to account for any increase of phase difference over 360°, and then a 'good data' mask is created for each ray. This separates the meteorological and non-meteorological echoes based on the standard deviation of Ψ_{DP} over ten consecutive range samples (< 12 °), the signal-to-noise ration (SNR, $> 3\,dB$), and the copolar correlation coefficient (ρ_{hv}, > 0.8). For 'bad data' segments, Ψ_{DP} is linearly interpolated between the two surrounding 'good data' points.

The Finite Impulse Response (FIR) filter is then applied to reduce the high frequency fluctuations in Ψ_{DP} from one radar measurement to the next along a ray, while keeping the overall pattern of Ψ_{DP} in that range. While a single use of the filter reduces most of the high frequency oscillations, in cases where δ is significant then its effects will still be visible in the filtered Ψ_{DP} signal. Therefore, an iterative process is implemented to remove δ from Ψ_{DP}, leaving the Φ_{DP} profile.

The iterative process is as follows. The initial 'raw' Ψ_{DP} is passed through the FIR to create a new, filtered Ψ_{DP}. Then, a new Ψ_{DP} profile is created by combining the initial profile and the filtered profile, depending on the difference between the two. For each range gate, if the absolute value of the difference between the raw and filtered Ψ_{DP} is below a specified threshold (which is set according to the expected standard deviation of the measurement of differential phase, 3°-5°), then the initial 'raw' Ψ_{DP} measurement is used in the new profile, otherwise the filtered Ψ_{DP} value is used. This new Ψ_{DP} profile is then passed through the FIR filter, and again a new profile is created, and this process is continued to convergence, determined by the change in Ψ_{DP} from one profile to the next being within some tolerance. Hubert and Bringi (1995) found that repeating this process 10 times produced good results; however, for S band, where δ is not significant, the number of iterations can be reduced to two. The outcome of this process is a smoothed profile without the effects of δ, and thus Φ_{DP} has been extracted from Ψ_{DP}.

Finally, K_{DP} is calculated using a least squares linear fit from the obtained Φ_{DP} profile. The value of radar reflectivity (Z_H) is the factor in choosing the number of consecutive range gates to use for the fit (10 gates if $Z_H > 45\,dBZ$, 20 for $30 < Z_H < 45\,dBZ$, and 30 for $Z_H < 30\,dBZ$). This further smooths the K_{DP} field along the ray, particularly in areas of light rain where values of K_{DP} are smaller.

The Bringi method, taken from the CSU Radar Tools GitHub repository with the

function name '*calc_kdp_bringi*' (Lang et al. 2016), is based on the same work by Hubbert and Bringi (1995), but there are a few small differences between this method and the one provided in the Rainbow software.

1. The CSU code assumes Ψ_{DP} has already been unwrapped prior to calling the function.

2. The CSU code only masks data based on the standard deviation of Ψ_{DP}, not including SNR and ρ_{hv} as the Rainbow software does.

3. The coefficients used in the FIR filter in the Bringi K_{DP} differ slightly to those in Hubbert and Bringi (1995). The documentation for the Rainbow software does not state which coefficients they use.

4. The default value for the number of iterations of the FIR filter in the CSU code is 1. Although the Rainbow documentation does not explicitly state how many iterations are used, it does say that it is typically 10 for C and X band radars, and 2 for S band.

5. In the K_{DP} calculation step, the threshold on reflectivity between using 20 and 30 samples is 35 dBZ in the Bringi K_{DP} estimation, compared to 30 dBZ in the Rainbow K_{DP} estimation.

3.3.2 Schneebeli Method

Schneebeli et al. (2014) describe a method of estimating K_{DP} along each ray by using a number of Kalman Filter estimates. Kalman filtering is an optimal estimation algorithm, a way of extracting information about what you can't measure from what you can. In this case, K_{DP} and δ are extracted from the measured Ψ_{DP} profile, with δ considered to be a function of K_{DP}. This method is implemented in the Python ARM Radar Toolkit (Py-ART, Helmus and Collis (2016)).

The Kalman filter is applied a number of times for each ray, with the error covariance matrix scaled by a set of factors a, where $a = 10^b$ and $b = -1, -0.8, -0.6, ..., 0.8, 1$. The filter is also applied to the Ψ_{DP} profile in each direction along the ray for each scaled error covariance matrix, resulting in an ensemble of estimates.

However, for the Kalman filter to work at the start and the end of the rays, 50 gates are added to the start of the ray with values of $0° + \eta$ (assuming $0°$ system offset

in Ψ_{DP}), and 50 gates of $\Psi_{DP}^{end} + \eta$ are added at the end of the profile, where η is a Gaussian noise component. Additionally, differential phase measurements rarely are defined throughout the entirety of the profile, for example spaces of clear air. Missing Ψ_{DP} values are linearly interpolated with a Gaussian noise component added. After completion of the process, estimates of K_{DP} and Φ_{DP} from these sections of the profile are removed.

The final K_{DP} estimate is taken from combining the forward and backward ensembles, taking either the forward or backward ensembles depending on whether K_{DP} is increasing or decreasing along the ray. This process results in a new ensemble of estimates, from which the final K_{DP} estimate is retrieved.

3.3.3 Maesaka Method

Maesaka et al. (2012) produce an algorithm to estimate K_{DP} that assumes a monotonically increasing Φ_{DP}. This assumptions means that the resultant K_{DP} is never negative. This assumption holds reasonably below the melting layer, in areas of rainfall, although in ice regions one might expect to encounter negative K_{DP} in certain regions, namely that where vertically-oriented ice crystals are dominant. This method is also implemented in Py-ART (Helmus and Collis 2016).

The Maesaka method creates a cost function to estimate K_{DP} from Ψ_{DP}. Firstly the lower and upper bounds for Φ_{DP} along the profile are determined through a linear regression over the first (last) 20 gates for the lower (upper) bound. If the slope of the regression line is positive, then the value of the regression line at the first (last) range is used for the boundary condition; however, if it is negative then the median value is used. The cost function is then constructed by comparing the measured differential phase with the boundary conditions, and the unknown solution of Φ_{DP} with the boundary conditions, plus a mean square of a Laplacian of k, which acts a s a low pass filter, where k is related to K_{DP}. K_{DP} is calculated from the solution that minimises the cost function.

3.3.4 Vulpiani Method

The third method used that is taken from Py-ART (Helmus and Collis 2016), the Vulpiani method uses a multistep moving-window range derivative approach, based on the work by Vulpiani et al. (2012). A first guess K_{DP} is obtained by taking half of

the difference of Ψ_{DP} at each end of the moving window divided by the size of that window, which is defined as 10 gates in the Py-ART code.

This first guess of K_{DP} is checked against wavelength-dependent thresholds of K_{DP} to remove phenomena such as aliasing, noise, and δ, with valid K_{DP} defined as greater than -2 $^{\circ}km^{-1}$ and less than 40 $^{\circ}km^{-1}$ for X-band radars. If K_{DP} fails this check, it is set to 0 $^{\circ}\,km^{-1}$. Then, the standard deviation of the estimated K_{DP} is calculated at each location, with the default option in the Py-ART code for the size of the window being 11. K_{DP} is set to zero where the standard deviation is greater than 5 $^{\circ}\,km^{-1}$.

The filtered differential phase from forward propagation estimate is reconstructed as the two way integral of K_{DP}. From this filtered Φ_{DP}, the final estimation of K_{DP} is then obtained, simply as the difference between range gates.

3.3.5 ωradlib Method

In the ωradlib python package (Heistermann et al. 2013), there are a few of options for estimating K_{DP}. The main option is based on the Vulpiani method. However, there are a few key differences in this implementation:

1. Firstly, the data is despeckled, to remove floating pixels between NaNs in the Ψ_{DP} data.

2. After the first guess of K_{DP}, Φ_{DP} is unfolded, based on searching for if K_{DP} is below a defined threshold (-20 $^{\circ}\,km^{-1}$).

3. A second guess of K_{DP} is derived using Lanczos convolution, rather than the simple finite difference scheme.

4. Thresholds are then applied on K_{DP}, with 20 $^{\circ}km^{-1}$ used for the upper threshold of K_{DP} rather than 40 $^{\circ}km^{-1}$.

5. The Φ_{DP} reconstruction and K_{DP} retrieval section is iterated over twice, using the resultant K_{DP} profile from the first iteration to initialise the second.

3.3.6 Ryzhkov Method

A very simple K_{DP} estimation method is described by Ryzhkov et al. (2005b). Ψ_{DP} is unfolded and smoothed along the radial using two different averaging windows, one of

9 gates and one of 25. This produces a 'lightly filtered' and a 'heavily filtered' radial profile. Then, two estimates of K_{DP} are obtained, as a slope of a least squares linear fit from the filtered Ψ_{DP} using the same two range averaging intervals, producing a 'heavy filtered' and a 'lightly filtered' estimate of K_{DP}. Then, for each range gate, the final estimate of K_{DP} is selected based on a reflectivity threshold: if $Z > 40dBZ$, the 'lightly filtered' estimate of K_{DP} is taken, otherwise the 'heavily filtered' estimate is used. With the WSR-88D radar used in their study, this results in a radial resolution of K_{DP} of about 6 km for in low reflectivity, and about 2 km in higher reflectivity.

3.3.7 UK Met Office Method

The UK Met Office use a relatively simple approach to calculating K_{DP}, based on a finite difference schemes of a 'cleaned-up' Ψ_{DP} profile. Two masks are created on the Ψ_{DP} profile, the first using a ρ_{hv} threshold of 0.9 to remove clutter from the profile. The resulting profile has a median filter applied, such that the value at each location is the median of that measurement, the 5 before, and the 5 after. This filtered data is then interpolated to fill in gaps in the Ψ_{DP} profile.

The second mask is created by setting the threshold of ρ_{hv} at 0.97, and then the same process of filtering and interpolating is applied, this time using 4 gates either side instead of 5. The remaining profile is then smoothed twice using a convolution function, firstly with a window size of 5, and secondly of 3. K_{DP} is then calculated from this smoothed profile using a second order central difference scheme along most of the ray, with a first order one-sided scheme used at the ends of the ray. Negative values of K_{DP} are then set to 0 $^{\circ}km^{-1}$.

3.4 Weather and Research Forecasting (WRF) Model

The WRF model is a mesoscale numerical weather prediction (NWP) model, developed primarily by the National Center for Atmospheric Research (NCAR), alongside partners such as the National Oceanic and Atmospheric Administration (NOAA) and the U.S. Air Force, designed as both a model for atmospheric research and operational forecasting (Skamarock et al. 2021). The model is used operationally by the National Centers for Environmental Prediction (NCEP 2022) and many other meteorological agencies and companies, and can be run on almost any computer, ranging from a Raspberry Pi to a high performance supercomputer.

The WRF-ARW model version 4.2.2 is used to simulate the atmospheric conditions on 24$^{\text{th}}$ January 2018. The model is centred over Chilbolton Observatory, utilising triple nested domains with horizontal grid spacing of 10km, 2km and 400m and 350, 401, and 501 grid points respectively in each horizontal direction (Figure 3.3). All of the domains have 81 vertical levels, with the highest level at 50 hPa. The model was run using the JASMIN computer facility, with initial and boundary conditions provided by the Global Forecasting System (GFS) model. The cumulus physics parameterisation used in the outer domain is the Kain-Fritsch parameterisation (Kain 2004), and the cumulus parameterisation is turned off for the smaller two domains due to the grid spacing, as WRF is able to explicitly resolve convection at resolutions of 4 km and higher (Knievel et al. 2004; Rogers 2010; Gao et al. 2017)). More information on all the chosen schemes can be found in Appendix A.

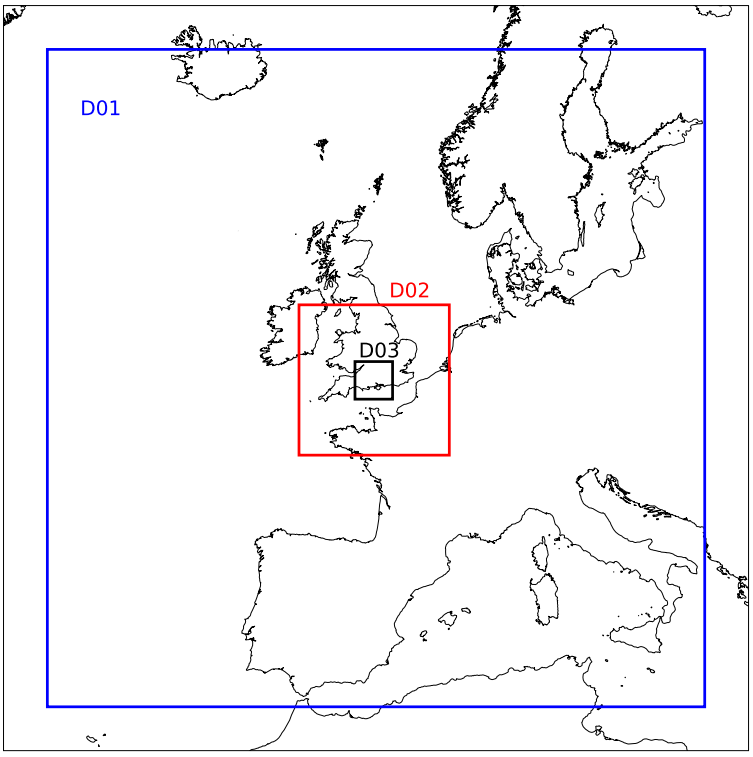

Figure 3.3: Horizontal extent of domains used in WRF model.

3.4.1 Microphysics schemes

One of the advantages of the WRF model is the ability to use a number of different parameterisation schemes. Three different microphysics schemes are used in Chapter 6 for each day simulated by the model - the Thompson scheme (Thompson et al. 2008), the Morrison scheme (Morrison et al. 2009), and the Milbrant scheme (Milbrandt and Yau 2005a,b). All of these schemes are double-moment schemes, which means as well as predicting mixing ratios for a number of hydrometeors (as a single-moment scheme does), they also predict number concentrations, which should increase model accuracy (Loftus et al. 2014). Table 3.1 shows which hydrometeors are predicted for each moment and in each microphysics scheme used.

Microphysics Scheme	Mass Mixing Ratios	Number Concentrations
Thompson	Cloud, Rain, Ice, Snow, Graupel	Ice, Rain
Morrison	Cloud, Rain, Ice, Snow, Graupel	Rain, Ice, Snow, Graupel
Milbrant	Cloud, Rain, Ice, Snow, Graupel, Hail	Cloud, Rain, Ice, Snow, Graupel, Hail

Table 3.1: Quantities predicted by the microphysics schemes used in Chapter 6.

Studies show that, even for idealised events, different microphysics schemes can result in quite varied results (for example Bao et al. (2019); Huang et al. (2020); Baki et al. (2021)), and one study that compared eight two-moment microphysics schemes concluded that none of them were consistently the best for all cloud properties, and often the ensemble mean had more realistic characteristics than each individual scheme (Wang et al. 2022). Therefore, three microphysical schemes are used in Chapter 6, rather than just selecting one.

3.5 Cloud-resolving model Radar Simulator (CR-SIM)

NWP models predict mixing ratios and number concentrations for different hydrometeor species; however, radars observe reflectivity and phase shifts which result from the interaction between radar radiation and hydrometeors (and other targets); NWP models do not simulate this interaction. To compare model data with radar observations, a forward operator is needed to emulate radar observables from high-resolution models. CR-SIM is a forward operator developed by Oue et al. (2020) that can take

NWP output from a number of different microphysics schemes, including the three mentioned in Section 3.4.1, and simulate radar and lidar observables at different radar wavelengths. This provides a way to compare directly between observations from the radar and predictions from the model. The simulated radar observables can be used to assimilate radar data into a new model run (Wang et al. 2013) or to help improve microphysical parameterisations (Ilotoviz et al. 2018).

CR-SIM works by using look-up tables which store the scattering amplitudes (that is s_{ij} as in Equation 2.7) of hydrometeors as calculated using the T-matrix method (Mishchenko 2000). The scattering amplitudes for each hydrometeor type at each grid space is found based on air temperature (for cloud and rain), bulk density (ice hydrometeors), radar frequency (3 GHz, 5.5 GHz, 9.5 GHz, 35 GHz, or 94 GHz), elevation angle (0° to 90° in 1° intervals), particle size, and aspect ratio. CR-SIM assumes a mean canting angle of 0° for all hydrometeors. The aspect ratios used in the work presented in Chapter 6 are the same as those used by Oue et al. (2020), that is the aspect ratios proposed by Brandes et al. (2002) for rain drops, 0.2 for cloud ice, 0.6 for snow, those by Ryzhkov et al. (2011) for graupel and hail. The bulk density used in CR-SIM is the same as is parameterised in the microphysics scheme. CR-SIM then creates Particle Size Distributions (PSDs) for each hydrometeor based on data from the model microphysics. Radar observables are then computed by integrating the scattering properties from the look-up tables over the PSDs for each hydrometeor type, using the equations in Appendix A of Oue et al. (2020), and then they are integrated over all hydrometeor types to produce a value for each radar observable at each grid box.

3.6 Facility for Airborne Atmospheric Measurements (FAAM)

The FAAM aircraft is a BAe-146-301 aircraft based in the United Kingdom, converted for the purpose of airborne atmospheric research. A number of flights took place during the winter of 2018 as part of the PICASSO campaign, during which a number of measurements of cloud microphysics were made. One of the instruments on board during these flights are used in this study: the CIP-15 camera is used in Section 5.2 to look for dominant ice habits or patterns that reflect the radar observations.

3.6.1 Cloud Imaging Probe 15 micron (CIP-15)

The CIP-15 probe takes two-dimensional images of hydrometeors at 15 micron resolution, by recording shadows as hydrometeors pass through a laser beam. This allows for identification of particle phase state, based on the assumption that ice particles are non-spherical and therefore produce non-circular images, which holds true except for frozen droplets (Korolev et al. 2017). There is also debate as to how many pixels are needed to distinguish between spherical and non-spherical images, and what size resolution is needed, and an issue with the image of particles depending on how close they are to the plane on which they cause a shadow. As such, care is needed to make sure only "in focus" images are used (Korolev et al. 2017). These images are looked at in Chapter 5 to aid the understanding of the radar observations.

Chapter 4

Evaluation of different K_{DP} methods

As shown in Chapter 2, specific differential phase is not measured directly by the radar, rather it is derived from total differential phase. There are a number of different methods and algorithms created with the purpose of extracting K_{DP} from Ψ_{DP}, with different levels of complexity; the eight used in this study are outlined in Section 3.3.

The natural question to ask then, if wanting to estimate K_{DP}, is which method is most appropriate, or provides suitable estimations, and therefore should be used. However, in the absence of truth, quantitatively defining the accuracy of an estimation is difficult, if not impossible. This is the case in many meteorological observations, for example temperature and rainfall, where whilst we can attempt to measure, the measurements are never perfect and always carry a degree of error. The estimation of K_{DP} is complicated by noisy measurements of Ψ_{DP}, and the potential existence of non-negligible backscatter differential phase (δ). In order to highlight the strengths and weaknesses in several K_{DP} estimation methods, two tests are conducted: firstly comparing a known, simulated 'truth' profile (Section 4.2), and then comparing the methods to each other using real data where no baseline truth can be established (Section 4.3).

4.1 K_{DP} Benchmark Setting

In order to know how good is good enough, first there must be some consideration of the expected K_{DP} estimations, and the application of those estimates. Firstly, Table 4.1 shows the K_{DP} values that give certain rain rate values based on equations 19 and 22 from Ryzhkov et al. (2014) for both S- and X-band radars respectively, and the range

of K_{DP} values that would result in a 5% error in rainfall. This shows that for accurate estimations of light rainfall, very precise estimations of K_{DP} are required, with less precision needed for the same error in rainfall estimation at higher rain rates. However, using the numbers for the standard deviation in K_{DP} from the standard deviation in Φ_{DP} as discussed in Section 2.1.4. In order to achieve a standard deviation in K_{DP} of $0.02° \, km^{-1}$ (for a rainfall estimation within 5% of 10 $mm \, hr^{-1}$ at S-band), the standard deviation of Φ_{DP} needs to be 0.36°, a lot smaller than the 3.1° mentioned in Section 2.1.4.

Rainfall Rate ($mm \, hr^{-1}$)	K_{DP} at S-band ($° \, km^{-1}$)	K_{DP} at X-band ($° \, km^{-1}$)	Rainfall Rate ± 5% ($mm \, hr^{-1}$)	K_{DP} range at S-band ($° \, km^{-1}$)	K_{DP} range at X-band ($° \, km^{-1}$)
1	0.01	0.03	0.95 - 1.05	0.01 - 0.01	0.03 - 0.03
5	0.07	0.22	4.75 - 5.25	0.07 - 0.08	0.21 - 0.23
10	0.16	0.52	9.5 - 10.5	0.15 - 0.17	0.49 - 0.55
50	1.17	3.87	47.5 - 52.5	1.10 - 1.24	3.63 - 4.12

Table 4.1: K_{DP} for given rainfall rates at S-band and X-band, based on Equations 19 and 22 in Ryzhkov et al. (2014).

While accurate rainfall estimation, for example, may require a high accuracy of K_{DP} estimation, this is not required for every use of K_{DP}. Many hydrometeor classification algorithms use a fuzzy logic scheme (Liu and Chandrasekar 2000; Thompson et al. 2014), which typically use beta membership functions which allow for a broader range of K_{DP} values to be weighted in the algorithm. In this case, one may consider half of the width of the slope of the membership function to be a reasonable allowable error in the K_{DP} estimation (that is an error which does not dramatically alter the contribution of K_{DP} to the output of the algorithm). This therefore varies depending on the algorithm, and could be over $0.5° \, km^{-1}$ (for example, dendrites at X-band in Thompson et al. (2014).

4.2 Comparison using a simulated K_{DP} profile

The algorithmic performance of the K_{DP} estimation methods is tested through a simulated profile, which gives an artificial 'true' profile by which the methods can be compared. This profile starts very simply, with uncertainty and additional phase measurements added to determine their impact on each estimation method. This simulated profile has 768 gates along the ray spaced 0.15 km apart (the same as the NCAS X-band radar). The 'true' K_{DP} is integrated to create a 'true' Φ_{DP}, and various noise is added, and 'missing measurements' created, resulting in a 'measured' Ψ_{DP} profile,

which is provided to the estimation methods from which to retrieve K_{DP}.

4.2.1 Constant K_{DP}

The simplest profile one can start with is that of constant K_{DP}. As some of the methods used assume K_{DP} at the start of the ray is equal to $0° \, km^{-1}$, the profile is prefixed with a small number of 'gates' with $K_{DP} = 0° \, km^{-1}$, with an immediate step change to the chosen constant value, which is $0.5° \, km^{-1}$. A similar step change at the end of the profile down to $0° \, km^{-1}$ is implemented at the end of the ray, with the step change expected to produce problems as K_{DP} often changes much more smoothly. These $0° \, km^{-1}$ values preceding and succeeding the K_{DP} profile are implemented in all of the simulated profiles.

As mentioned in Section 3.3, the Ryzhkov and Bringi methods use different window sizes depending on the measured reflectivity. As there is no reflectivity profile here, a number of constant reflectivity profiles are used to match the different thresholds in each method.

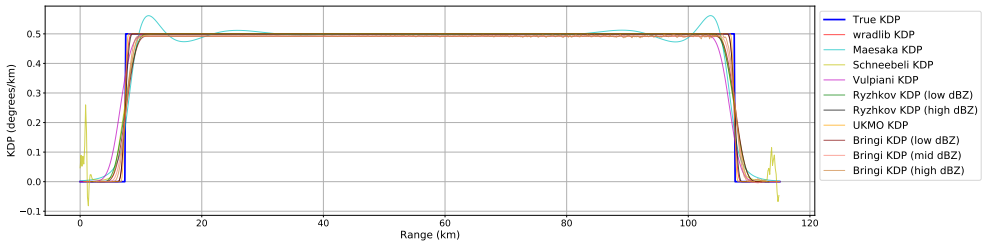

Figure 4.1: Estimating a constant K_{DP} profile.

Figure 4.1 shows the 'true' K_{DP} profile and the estimated profile retrieved by each method. The estimation methods are mostly able to reproduce the 'true' K_{DP} profile; however, the Bringi method, at all reflectivity thresholds, underestimates K_{DP} by about $0.01° \, km^{-1}$, which is likely a result of smoothing of the Ψ_{DP} profile by the finite impulse response filter, accounting for the sections of $0° \, km^{-1}$ K_{DP} at each end of the profile. The sharp transitions between $0° \, km^{-1}$ and $0.5° \, km^{-1}$ are not replicated in any of the methods, as they all employ some sort of smoothing or averaging window, which smooths out large and sudden changes in the Ψ_{DP} profile, and therefore the sudden change in K_{DP} is smoothed out as well. Additionally, noise is seen at the start and end of the profile estimated by the Schneebeli method. This is due to the addition of slightly noisy Ψ_{DP} data to each end of the measured profile needed for the Kalman filter to work (see Section 3.3.2).

4.2.2 Sinusoidal K_{DP}

While reassuring to see accuracy in each of the estimation methods against a constant K_{DP} profile, such a profile is not very realistic. Therefore, first complication added to the simulated profile is to add changing K_{DP} values along the ray. A simple sine wave is used to model the changing values of K_{DP}, with negative values set to $0° \, km^{-1}$. While not entirely realistic, the sinusoidal pattern does give smooth changes in K_{DP}, with spatially smooth profiles often seen as ideal, particularly when estimating rainfall from K_{DP}. This profile has five peaks in K_{DP} with values of $1° \, km^{-1}$.

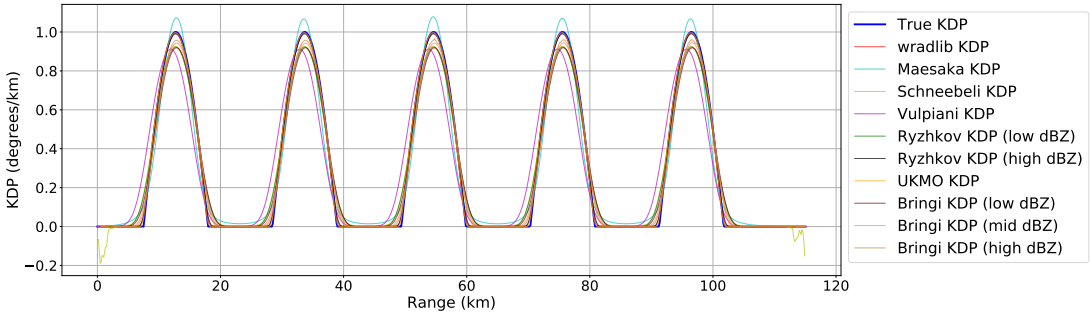

Figure 4.2: Same as Fig.4.1, using a sinusoidal K_{DP} profile with negative values set to 0.

Figure 4.2 starts to show some differences between the retrieved profiles. The wradlib and UKMO methods still accurately estimate K_{DP}; however, the Maesaka method overestimates the peak by about $0.07° \, km^{-1}$, and the Schneebeli method and the Vulpiani method underestimate by about $0.07° \, km^{-1}$ and $0.09° \, km^{-1}$ respectively. The Vulpiani method also peaks early, compared to the 'truth'. The other profiles appear to have timing that matches the peaks in the 'true' profile. Between the peaks, all the retrieved K_{DP} profiles return to $0° \, km^{-1}$ a little after the 'true' profile, partly due to the sharp change seen in the 'truth' whereas the estimated profiles prefer a smooth transition. Similarly, non-zero K_{DP} values are estimated earlier preceding each peak than are seen in the 'true' profile. The exception to this is the Maesaka method, in which the K_{DP} profile does return to $0° \, km^{-1}$ after the final peak; however, between peaks the profile only returns to about $0.01° \, km^{-1}$.

The two methods that are dependent on reflectivity (Ryzhkov and Bringi) show differing results as reflectivity changes. The Ryzhkov method, which has two reflectivity regions separated at 40 dBZ, matches the truth well for high reflectivity measurements, but it underestimates the peaks by almost $0.1° \, km^{-1}$. The Bringi method, which has three reflectivity regions with splits at 35 dBZ and 45 dBZ, underestimates for all three, with

the degree of underestimation increasing as reflectivity decreases. For both methods, as reflectivity decreases, the averaging window in the K_{DP} estimation method increases in size, so at the peaks the highest values of K_{DP} are diluted by smaller values which are more prevalent in the larger averaging windows, resulting in underestimation. The opposite is true at the transition from $K_{DP} = 0° \, km^{-1}$ to positive K_{DP}: the larger averaging window size picks up the positive 'true' K_{DP} further from the 'truth' than the smaller averaging windows, so the K_{DP} estimations at lower reflectivity remain above $0° \, km^{-1}$ far longer than those estimations at higher reflectivity.

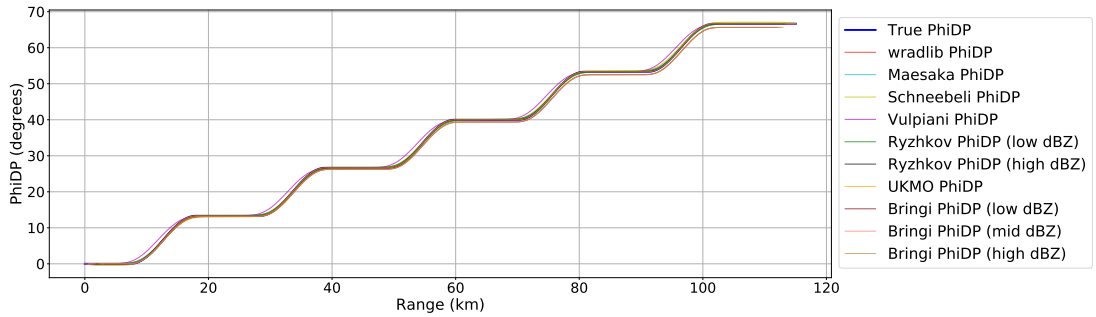

Figure 4.3: 'True' and estimated Φ_{DP} profiles for the 'true' sinusoidal K_{DP} profile.

Despite these observed shortcomings in the K_{DP} profiles, it is worth noting how they affect the Φ_{DP} profiles, shown in figure 4.3. For the Vulpiani method, the timing and magnitude differences observed in K_{DP} appear to average each other out, so that the retrieved Φ_{DP} profile generally agrees with the 'truth', albeit with slightly more gradual inflection points and slightly early on the timing. The Schneebeli method shows a similar pattern in its retrieved Φ_{DP}, with a slightly early pattern and yet slightly more gradual inflection points; however, the deviation from the 'truth' does increase along the profile, suggesting that the differences in the K_{DP} profile due to timing are slightly larger than the differences due to peak magnitude. Somewhat surprisingly, despite overestimating the peaks of K_{DP} and the profile not returning to 0 between those peaks, the Φ_{DP} profile retrieved using the Maesaka method is a very close match to the 'truth'. The Maesaka K_{DP} profile exhibits much steeper changes than the 'true' profile, and therefore is underestimating the truth a lot of the time, despite the stand-out differences being in the overestimation. These differences compensate well to give an accurate Φ_{DP} profile. Unsurprisingly, as the wradlib K_{DP} retrieval was very close to the 'truth', so is its retrieved Φ_{DP} profile.

4.2.3 Missing Ψ_{DP} measurements

Sometimes there may be no value of Ψ_{DP} at a gate, or number of gates, along the ray. This could be due to there being no scatterers in that region, the measurement of the returned phase shift being rejected by the radar as bad or invalid data, or an error in processing. This leaves a Ψ_{DP} profile with gaps in, from which K_{DP} is to be retrieved. To replicate this, a random selection of 20 gates along the ray in section 4.2.2 are removed. Two estimated Φ_{DP} and K_{DP} profiles are now obtained from each estimation method, one using the 'raw' Φ_{DP} profile with the missing data, and the other with Φ_{DP} linearly interpolated between the missing data points. As the missing data gates are randomly selected, by running this multiple times an ensemble approach to the statistics can be utilised.

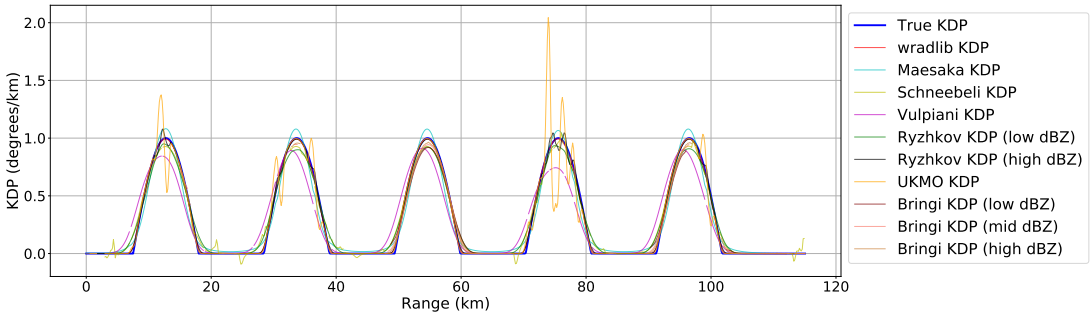

Figure 4.4: Same as Fig.4.2, with 20 missing Ψ_{DP} observations in the 'raw' profile.

While the exact location of the missing observations does have an effect on the retrieved profiles, the general observations hold true regardless of location. Therefore, while only one ensemble is shown, this discussion holds for all ensembles.

The Vulpiani method is most affected of the Py-ART estimation methods by missing observations where K_{DP} is non-zero. It can be clearly seen in Figure 4.4 that the magnitude of the K_{DP} peaks estimated by the Vulpiani method are lower than in Figure 4.2 if there is missing data around those peaks, whereas the peaks without missing data are similarly estimated. This effect is also seen in the estimated Φ_{DP} profile (figure 4.5), which has significantly lower Φ_{DP} values than the 'truth' and than those produced by the other methods. This occurs because during the processing, K_{DP} is set to $0\ ^\circ\, km^{-1}$ where data is missing. If that happens to be in at a location where surrounding K_{DP} is positive, as most clearly seen during the fourth peak, that positive K_{DP} information is lost in the Φ_{DP} estimation, resulting in lower K_{DP} (figure 4.4) and Φ_{DP} (figure 4.5).

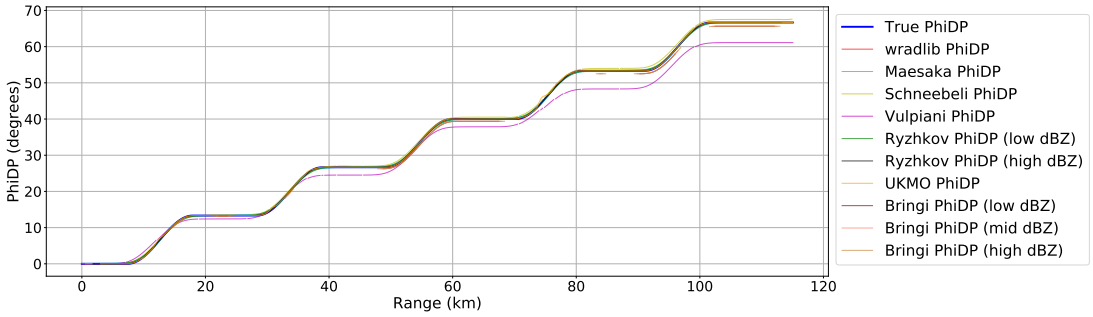

Figure 4.5: Same as Fig.4.4, but showing 'true' and estimated Φ_{DP} profiles.

Missing data also has an observable affect on K_{DP} from the Schneebeli method: around the missing data points the profiles lose their smoothness and appear noisy. This noise, when located near one of the K_{DP} peaks, can result in K_{DP} peaks that match the 'truth' a lot more closely than before (for example, the first and third peaks in Figure 4.4). However, this has minimal impact on the Φ_{DP} profile (figure 4.5), which still closely reproduces the 'true' Φ_{DP} but does drift slightly higher through the profile.

In this implementation of the Bringi estimation method, if there is a missing measurement anywhere within the averaging window, that value of K_{DP} is not estimated and is set to be missing. This results in some very large gaps in the K_{DP} profile, especially in low reflectivity. The implementation of the Ryzhkov method does not have the same issue and generally performs the same as previously, besides a few small changes seen when there are missing data in the 'truth' near the peaks.

This implementation of missing Ψ_{DP} values highlight an underlying assumption in the UKMO method which may not always hold true. The UKMO method removes invalid Ψ_{DP} measurements, firstly to create a non-meteorological mask, secondly to create a rain mask, based on meeting a threshold of the measured, or lack of, ρ_{hv} value. In this work, while there are gaps in the Ψ_{DP} profile, there are no gaps in the ρ_{hv} profile used, and as such there are no invalid Ψ_{DP} measurements. This means that when the median filter is applied on the Ψ_{DP} profile, the missing values affect the output, resulting in a noisy output around the location of the missing Ψ_{DP} measurements. As this process is done twice, the effect is amplified, resulting in a noisy K_{DP} estimation around those locations. Adjusting the code to remove locations of missing Ψ_{DP} independently of the ρ_{hv} measurement removes the noise in the estimation. However, as this is a study of the accuracy of these methods as they are used, this adjustment is not applied through the rest of this study.

Interpolating Ψ_{DP} between the missing points has a noticeable impact on the estimated

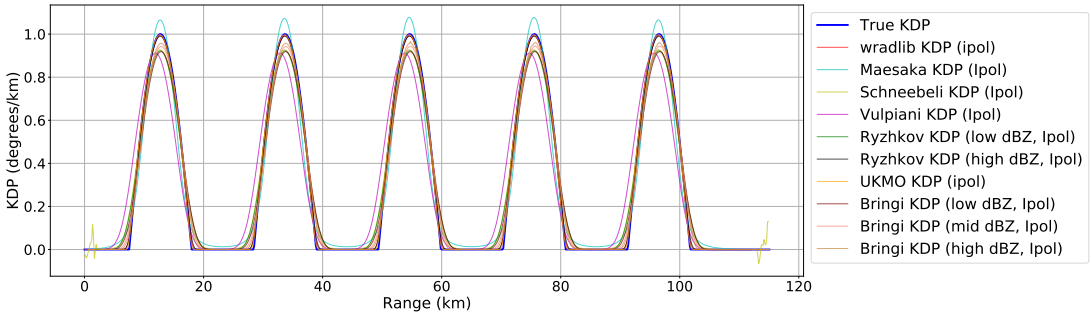

Figure 4.6: Same as Fig.4.4, but with the 20 missing Ψ_{DP} observations have been interpolated.

K_{DP} profiles, as seen in Figure 4.6. It can be seen that the changes mentioned above in the profiles estimated by the Vulpiani and Schneebeli methods are no longer present, and the large gaps in the Bringi estimation methods are filled, such that these profiles now appear the same as in Figure 4.2. Therefore, interpolation of the Ψ_{DP} profile over missing data points should be considered as part of a pre-processing routine before estimation of K_{DP}.

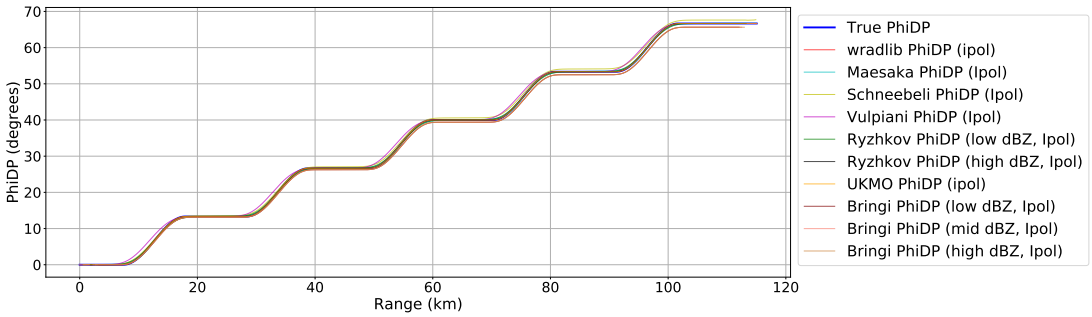

Figure 4.7: Same as Fig.4.6, but showing the 'true' and estimated Φ_{DP} profiles.

4.2.4 Factors that affect Ψ_{DP} measurements: individually

There are three key factors that can be added to this simulated K_{DP} profile to obtain more realistic Total Differential Phase measurements, which are then used to retrieve the original K_{DP}. These factors are the existence of negative K_{DP}, noise and inconsistency in the measurements, and the potential presence of backscatter differential phase.

Negative K_{DP}

In most circumstances, K_{DP} is positive, that is the specific phase shift of the horizontal component of the radar beam is greater than that of the vertical component. This is a result of the fall geometry of hydrometeors under the influence of gravity and atmospheric drag, in which the elongated axis of the hydrometeor is horizontally orientated. However, in some cases, hydrometeors may fall with their elongated axis perpendicular to the ground, resulting in observations of negative K_{DP}. The most common case of this is in the presence of electric fields in clouds, where ice crystals can become vertically orientated.

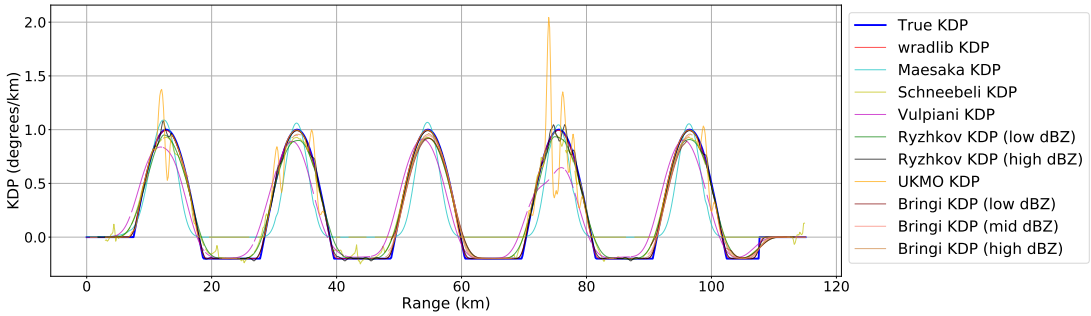

Figure 4.8: Same as Fig.4.4, with the K_{DP} values are truncated at -0.2° km^{-1} rather than 0° km^{-1}.

To view how the different estimation methods cope with negative K_{DP}, the simulated truth is adjusted so that values below -0.2° km^{-1} are set to -0.2° km^{-1}, as opposed to values below 0° km^{-1} being set to 0° km^{-1} as before. This new 'true' K_{DP}, and the retrieved K_{DP} profile from each of estimation methods, is shown in Figure 4.8. Given the previous results in this chapter, particularly Figure 4.4, and knowledge of the choice to exclude negative K_{DP} in the Maesaka and UKMO estimation methods, these estimated profiles are not surprising. The only significant difference in allowing negative K_{DP} is observed in these two estimated profiles, as these methods assumes that all K_{DP} is non-negative. The two methods diverge slightly in their estimation of the K_{DP} peaks: while the UKMO method still accurately estimates the peak value in K_{DP} (ignoring the issue with missing data), the Maesaka method estimates slightly higher peak values, with a greater rate of change of K_{DP} than the 'truth'. This is because the UKMO method allows K_{DP} to be negative during calculation, truncating negative K_{DP} values to 0 ° km^{-1}, whereas the Maesaka method does not have negative K_{DP} at any point in its calculation. As a result, to reduce the cost function used in the Maesaka method in areas where K_{DP} is negative, the constant portion of the estimated Φ_{DP} profile stretches slightly each side into areas of positive K_{DP}, as can be seen in figure 4.9. This means narrower and higher K_{DP} peaks are calculated to produce a Φ_{DP} profile that best solves the cost function.

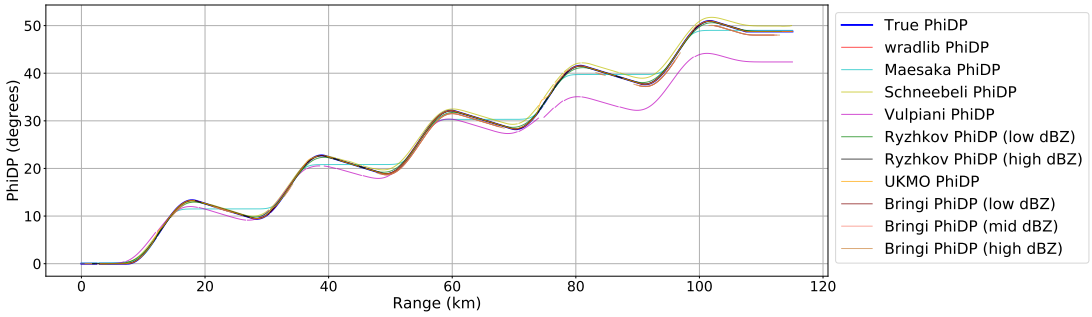

Figure 4.9: Same as Fig.4.8, but showing the 'true' and estimated Φ_{DP} profiles.

Noise

To this point, only clean profiles of Ψ_{DP} have been considered. Measurements of Total Differential Phase are always noisy, and part of the work of the estimation methods is to remove noise from the profile, while retaining the Φ_{DP} signal from which to estimate K_{DP}. A noise profile is therefore created, using Equation 6.80 from Ryzhkov and Zrnić (2019):

$$\mathrm{SD}(\Phi_{DP}) = 30.3 \left(\frac{\rho_{hv}^{-2} - 1}{\sigma_{vn} M} \right)^{0.5}, \tag{4.1}$$

where $\sigma_{vn} = 4\sigma_v T_s / \lambda$ is the normalized spectrum width (σ_v), λ is the wavelength in metres, T_s is the pulse repetition period in seconds, and M is the number of pulses. Here, σ_v is set to 1 $m\,s^{-1}$, and the other parameters are taken from the NCAS Mobile X-Band Radar during its deployment at Chilbolton Observatory, so that $\lambda = 0.032m$, $T_s = 0.001s$, and $M = 60$. These values result in $\mathrm{SD}(\Phi_{DP})$ equal to 1.58° when ρ_{hv} is 0.99, increasing to 8.30° when ρ_{hv} is 0.8. Following Equation 2.16, this results in $\mathrm{SD}(K_{DP})$ equal to 0.15° km^{-1} and 0.77° km^{-1} respectively in the case of the Ryzhkov method for low reflectivity (M_r in Equation 2.16 is equal to 25). This $\mathrm{SD}(K_{DP})$ is slightly smaller than the example discussed in Section 2.1.4 for the NEXRAD radars, due to a higher normalised spectrum width and greater number of pulses used by NX-Pol-1.

To use this equation to create noise, a profile of co-polar correlation coefficient (ρ_{hv}) is needed. ρ_{hv} is generally close to 1; however, it decreases in some places, particularly in the melting layer. The central K_{DP} peak was therefore selected to be in the melting layer, and Figure 4.10 shows the idealised ρ_{hv} that was then created. The minimum value of ρ_{hv} of 0.8 was chosen based on the hydrometeor classification algorithm in Thompson et al. (2014) and the range of expected values for ρ_{hv} in the melting layer in Fabry (2015). Noise was then added to this ρ_{hv} profile, using the standard deviation

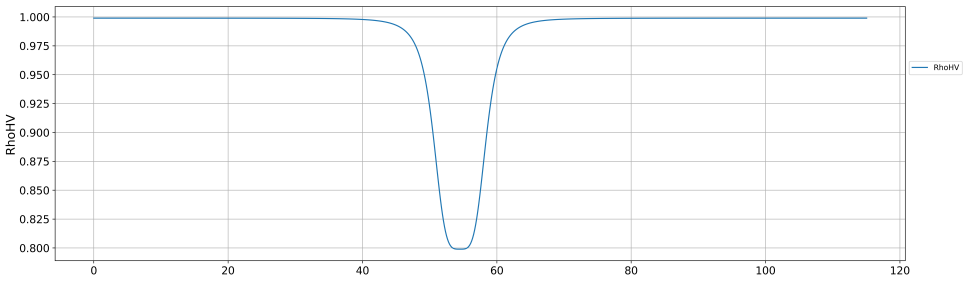

Figure 4.10: ρ_{hv} profile created for adding noise to the simulated true profile.

as also given by Ryzhkov and Zrnić (2019):

$$\mathrm{SD}(\rho_{hv}) = 0.53\frac{1-\rho_{hv}^2}{(\sigma_{vn}M)^{0.5}}. \tag{4.2}$$

For each location along the profile, noise for ρ_{hv} is generated by picking a random number from a Gaussian distribution, with a mean of 0 and the standard deviation as calculated for that location. This noise is then added to the idealised ρ_{hv} profile at that location, creating a new noisy ρ_{hv} profile, which in turn is then used to calculated the standard deviation of Φ_{DP}, and the same process is used to create the noise in the Ψ_{DP} profile. The noise in Ψ_{DP}, and how this adds to the defined Φ_{DP} profile to create the final Ψ_{DP} profile, are shown in Figure 4.11.

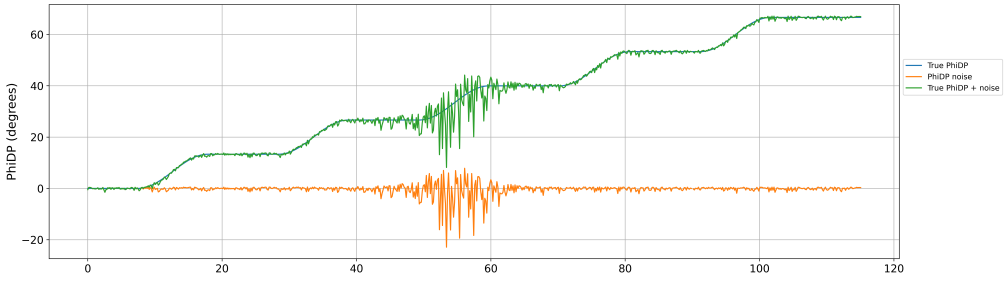

Figure 4.11: Noise (orange) added to Φ_{DP} (blue) to create a profile of Ψ_{DP} (green).

The effect of adding noise to the Ψ_{DP} profile is shown in Figure 4.12. This shows that the different estimation methods cope quite differently to each other due to the introduction of noise to the Ψ_{DP} profile. The wradlib-derived K_{DP} estimation, which until this point matched the 'true' profile better than any of the other methods, now exhibits noise throughout its estimated profile, which is largely exaggerated through the 'melting layer'. The peak K_{DP} value estimated here is over $4° \, km^{-1}$, and in some

ensemble members it reaches $5° \, km^{-1}$, whilst the maximum value in the 'true' profile is $1° \, km^{-1}$, and throughout most of this peak K_{DP} values are largely overestimated compared to the 'truth'. This results in significant deviation from the 'truth' in the estimated Φ_{DP} profile, with the estimated Φ_{DP} increasing by approximately 30° through the 'melting layer', when the 'true' Φ_{DP} only increases by about 15° (Figure 4.13).

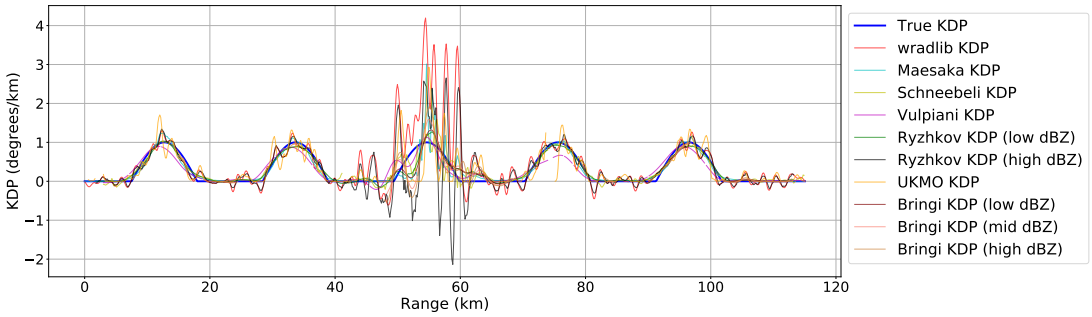

Figure 4.12: Estimated and simulated K_{DP} profiles when noise is included in the Ψ_{DP} profile.

The UKMO method shows similar noise throughout its profile outside the 'melting layer', greater than that shown by the wradlib method, although the limitation on negative values means that some of this noise is obscured by being set to zero. Within the 'melting layer', the estimated values are not as extreme as those from the wradlib method, but they are still not representative of the 'true' K_{DP} profile.

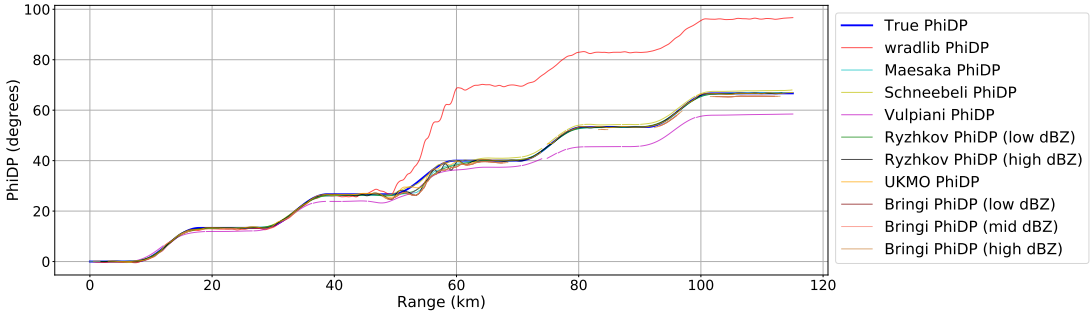

Figure 4.13: Same as figure 4.12, but showing the 'true' and estimated Φ_{DP} profiles.

All of the other estimation methods are also affected by the introduction of noise, although not so severely. The pattern in the Maesaka-estimated K_{DP} is broadly the same in the 4 'normal' K_{DP} peaks, with greater rate of change of K_{DP} and slight overestimation at the peaks; however, through the 'melting layer' the K_{DP} estimation becomes noisy, with values ranging from about $0.2° \, km^{-1}$ to around $1.6° \, km^{-1}$.

The Vulpiani method is affected less by the introduction of noise than most of the

other methods. The K_{DP} estimation it derives still exhibits a smooth pattern, with a small change in the 'melting layer'; however, the previously observed pattern of underestimation and early timing are still the significant factors.

The Ryzhkov and Bringi methods produce differing results based on the value of reflectivity. In both methods, the profiles that assume lower reflectivity, and therefore utilise larger averaging windows, filter out noise well, and as such the effects of noise are small in the estimated profile. Noisy measurements have more of an effect on these methods as reflectivity increases, especially for the Ryzhkov estimation method, which away from the 'melting layer' follows the wradlib method quite closely. Within the 'melting layer', it does not show the same extreme estimation, but the Ryzhkov method still exhibits more noise and larger values than most of the other methods. However, for the high reflectivity versions of the Bringi estimation, while there is a little more noise in the estimated profile, it is still quite close to the low reflectivity version - in high reflectivity areas, the Bringi estimation method removes noise better than the Ryzhkov estimation method.

Backscatter Differential Phase

The final factor that affects Ψ_{DP}, and hence the retrieval of K_{DP}, is the potential presence of Backscatter Differential Phase (δ). δ is the difference between the phase of the horizontal and vertical components of the radar beam that occurs as a result of scattering, rather than the phase change that occurs as the beam travels through a different medium. The value of backscatter is dependent on radar wavelength, temperature, and hydrometeor size. At X band, the magnitude of δ is small for drop diameters of less than 2.5mm, but increases significantly after. Contributions to Ψ_{DP} caused by δ need to be removed before K_{DP} can be estimated.

Using work by Trömel et al. (2013), based largely on their Figures 3 & 8, a profile of δ is created for X band, and is shown in Figure 4.14. δ in rain is largely a function of temperature and raindrop size. Below the 'melting layer', δ is set to 0.8°, resembling raindrops with diameter around 3mm, and above the 'melting layer' δ is equal to 0°, as δ is negligibly small for most ice hydrometeors, including snow, crystals, and graupel. Within the melting layer, δ is difficult to reliably estimate; however, Trömel et al. (2013) used a microphysical and scattering model to estimate δ up to about 4°. The limitation of their model is that it does not include aggregation, which they comment would significantly increase δ. The simulated profile used here has a peak value of δ of 5°, although larger values could be observed, especially for X band.

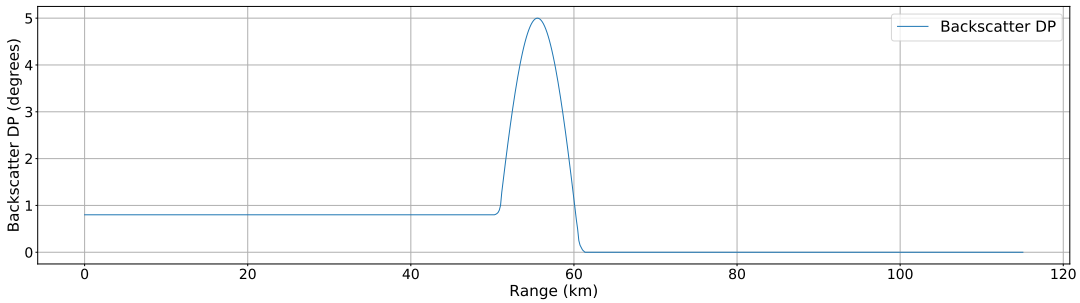

Figure 4.14: Created backscatter differential phase profile to be added to Φ_{DP} profile to make Ψ_{DP}.

Figure 4.15 shows K_{DP} profiles from the different estimation methods as a result of including δ in the Ψ_{DP} profile. None of the methods are successful in completely removing the effects of δ in the melting layer, which is evident in the estimated Φ_{DP} profiles by the 'bump' seen between 50 and 60 km (figure 4.16), and in the oscillating nature of the K_{DP} profiles, with overestimation of K_{DP} before the 'true' peak as δ increased, followed by negative values of K_{DP} after the 'true' peak as δ decreased. The Maesaka- and UKMO-estimated profiles are the exception to this, as they do not allow for negative K_{DP}; however, they still do not remove δ in the 'melting layer' and significantly overestimate K_{DP}. This is not surprising, given that the Maesaka estimation method is designed for rain, where the effects of δ are small, and in this case with constant δ before the 'melting layer', its effects on K_{DP} estimation are negligible, not just for the Maesaka method but for all.

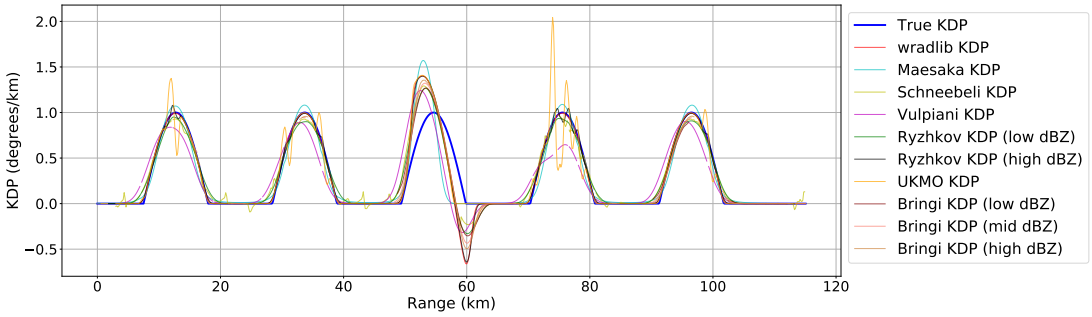

Figure 4.15: Estimated and 'true' K_{DP} profiles when δ is included in the Ψ_{DP} profile.

In both the methods that are dependent on reflectivity, the lower reflectivity versions have smaller estimations of K_{DP} around the 'δ-bump', for the same reason as why they have smaller peaks mentioned in Section 4.2.2: the larger averaging window used reduces the impact of more extreme values, smoothing out the resultant profiles.

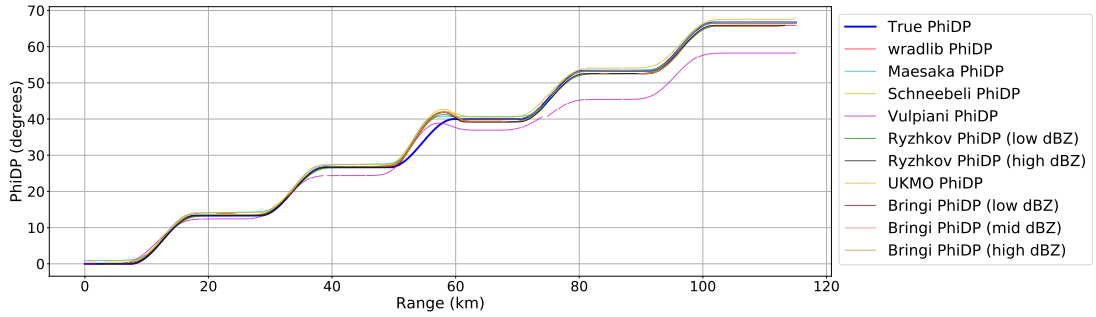

Figure 4.16: Same as figure 4.15 but showing Φ_{DP}.

4.2.5 Factors that affect Ψ_{DP} measurements: pairs

After analysing the effect on the estimated K_{DP} profiles individually, these three factors (negative K_{DP}, noise, and δ) can be paired together to see if they affect each other, or if there is a more dominant factor. Figures 4.17, 4.18, and 4.19 show the estimated profiles when there is noise in the Ψ_{DP} when allowing negative values of K_{DP}, when there is noise and δ in the Ψ_{DP} profile, and when δ is present in Ψ_{DP} and negative K_{DP} is allowed, respectively.

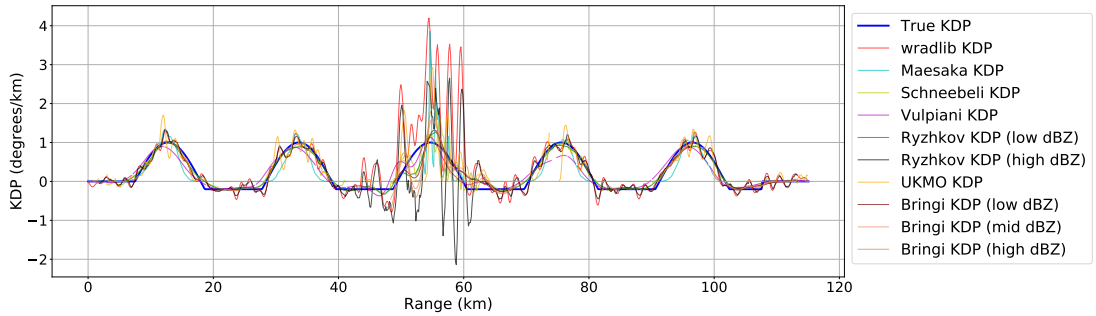

Figure 4.17: Estimated and 'true' K_{DP} profiles with negative K_{DP} values and noise included in the Ψ_{DP} profile.

These figures show that these factors, and the changes they make to the estimated K_{DP} profiles, combine together without creating anything unexpected or new. In Figure 4.17, where noise and negative K_{DP} are present, the results are effectively the noisiness in Figure 4.12 overlaying the profiles seen in Figure 4.8 where negative K_{DP} is the only additional factor.

In Figure 4.18, where noise and δ are included, the resultant profiles are very similar to Figure 4.12; however, the values of K_{DP} are slightly higher at the start of the 'melting layer' as a result of the presence of δ. This is especially observed in the Maesaka-

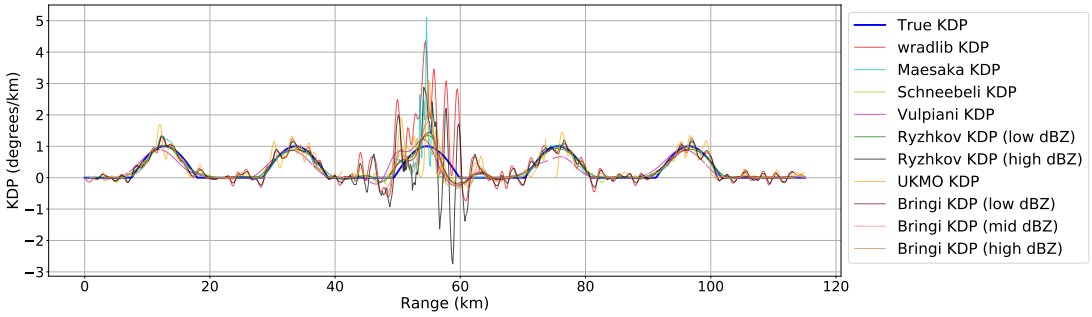

Figure 4.18: Estimated and 'true' K_{DP} profiles with δ and noise included in the Ψ_{DP} profile.

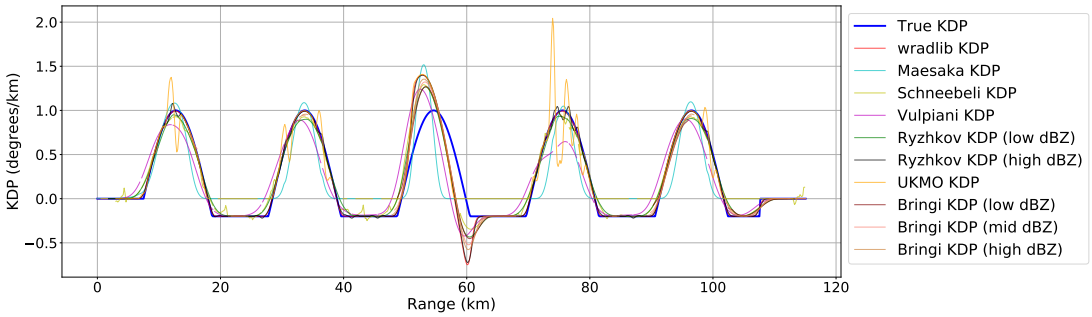

Figure 4.19: Estimated and 'true' K_{DP} profiles with negative K_{DP} values and δ included in the Ψ_{DP} profile.

derived K_{DP} profile, which is slightly noisy in the 'melting layer' in Figure 4.12, and has the largest early peak K_{DP} value in the presence of δ (Figure 4.15), and so in Figure 4.18 where these effects are combined, the largest value of K_{DP} in the 'melting layer' region increases from about 1.9° km^{-1} and 1.6° km^{-1} in the noise-only and δ-only profiles to about 4.4° km^{-1} when these two factors are combined. The combination of δ and noise also has an effect on the Vulpiani and Ryzhkov (low reflectivity) estimated profiles around the 'melting layer'. The effect of noise alone within the 'melting layer' is to produce two peaks, akin to a bimodal distribution, this being more pronounced in the Ryzhkov (low reflectivity) profile. The introduction of δ means that the first of these peaks is reinforced, and the second diminished, by the early peak caused by not correctly accounting for δ, resulting in a shape around the 'melting layer' that looks more like a Poisson distribution, with an early peak and a longer tail.

The profiles in Figure 4.19, combining the presence of δ and negative K_{DP}, are also as expected, almost exactly combining the profiles in Figure 4.15 with the allowance for negative K_{DP} shown in Figure 4.8.

4.2.6 Factors that affect Ψ_{DP} measurements: all three

Having looked at negative K_{DP}, noise and δ individually and paired together, all three are now combined to create a more realistic Ψ_{DP} profile, further testing the capabilities of the estimation methods. The results of this are shown in Figure 4.20. As when pairing factors together, combining all three does not introduce any new limitations or failures in the estimated K_{DP} profiles, rather just combining together what has already been mentioned. The noise continues to have the most noticeable effect, especially within the 'melting layer'; however, the effects due to δ and due to negative K_{DP} can also be seen.

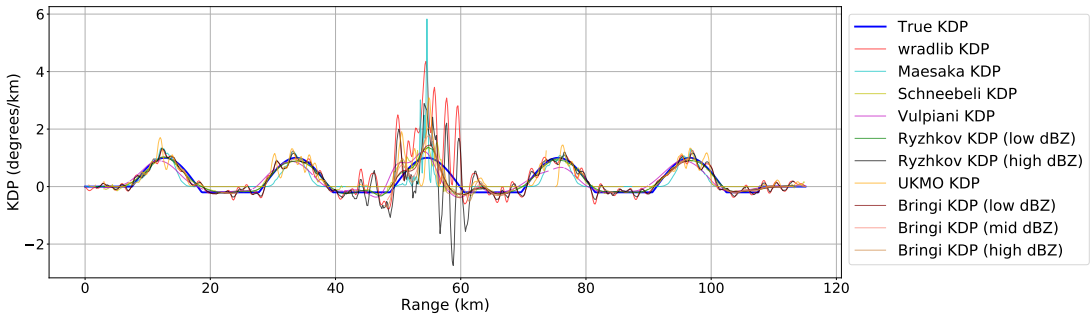

Figure 4.20: Estimated K_{DP} profiles from a Ψ_{DP} profile that includes noise, δ and negative K_{DP}.

4.2.7 Statistical evaluation

Having looked at how each method estimates K_{DP} with different factors applied to the Ψ_{DP} profile for one profile, the same is done 52 more times, each with different noise and missing gates. Figures 4.21 & 4.23 shows the mean correlation coefficient across all of these ensembles for each estimation method, using 'raw' and 'interpolated' Ψ_{DP} respectively, compared to the 'true' K_{DP} at each of the previously outlined stages, as well as the minimum and maximum correlation coefficient across the ensembles.

The first row in Figure 4.21 shows the correlation coefficient between each K_{DP} estimation method and the 'truth' for our original, clean K_{DP} 'true' profile, with the mean absolute error for the same comparison shown in the first row of Figure 4.22. As there are no missing data points here, there is no interpolation process, and so the interpolated results should (and do) match the original estimation (compare Figures 4.23 & 4.24 with Figures 4.21 & 4.22). This confirms what was previously suggested in Section 4.2.2, that all of the methods estimate this clean K_{DP} well, the wradlib

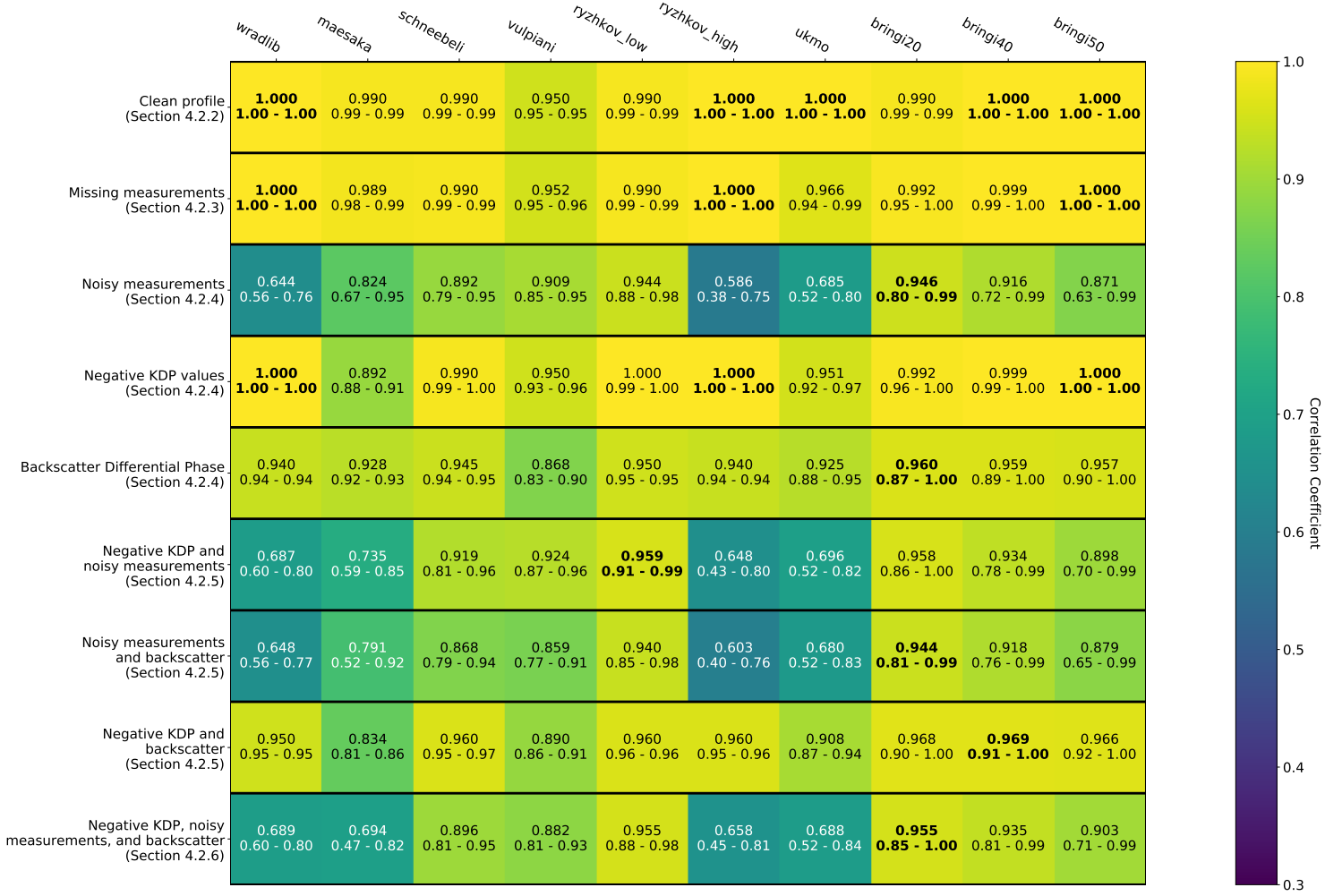

Figure 4.21: Correlation Coefficient for each method at each stage compared to the 'true' K_{DP}. The central number in each box is the mean correlation coefficient from all ensemble members, beneath is the minimum and maximum coefficients. The highest values in each row are in bold type.

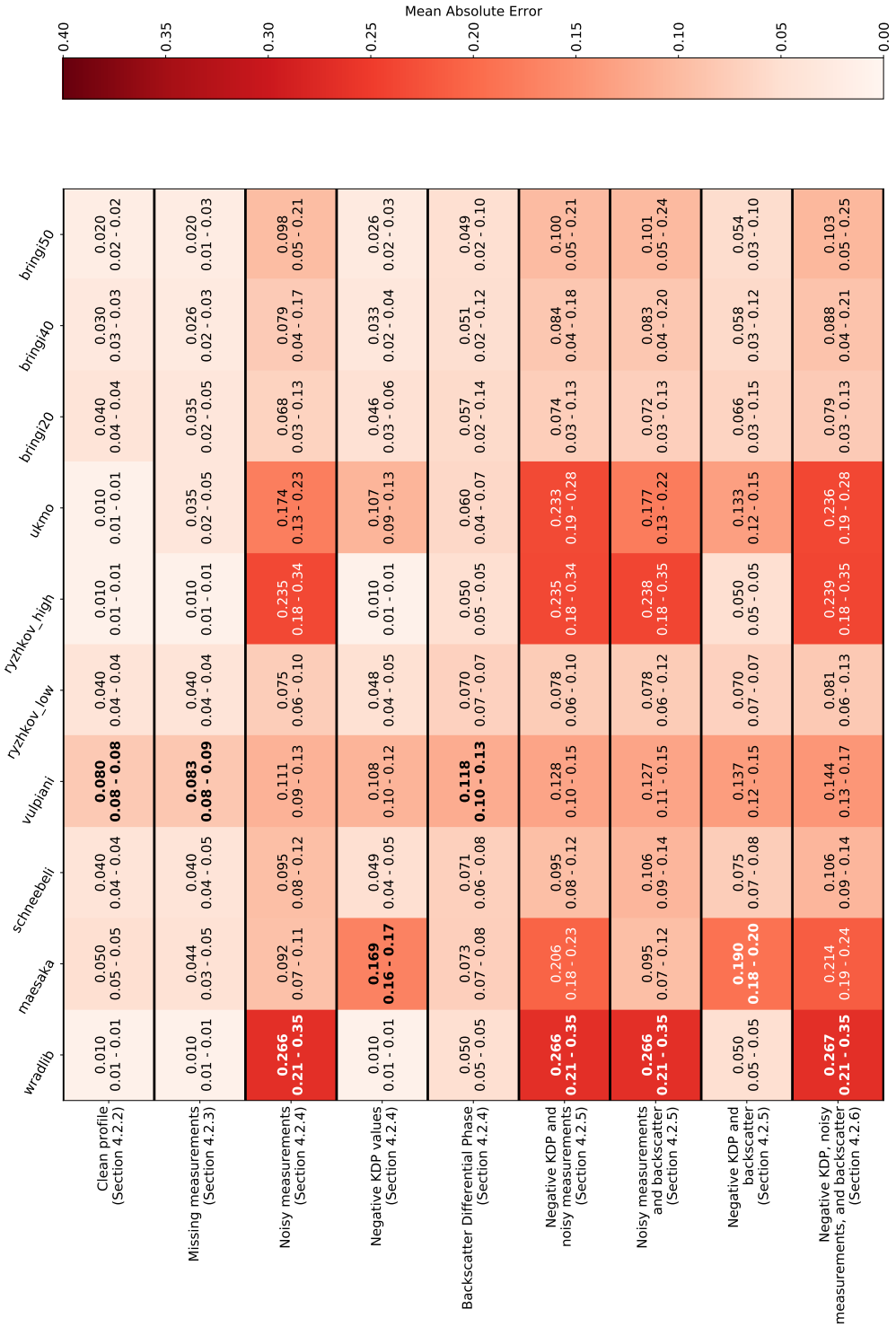

Figure 4.22: Same as Fig.4.21, but showing Mean Absolute Error. The lowest values in each row are in bold type.

method estimating most accurately, and the Vulpiani method with its mistimed peaks least accurately. When some of the data points are missing (Section 4.2.3, and the second row in figures 4.21 & 4.22), the correlation coefficient and the mean absolute error are very similar for each method to those calculated for the 'clean' profile. While there are observable differences in the profiles estimated by the Vulpiani and Schneebeli methods when there is missing data compared to what they estimated for the 'clean' profile, these differences have little affect on the statistics.

The third, fourth and fifth rows in Figures 4.21 & 4.22 show the results when one factor was added to the Ψ_{DP} profile, being noise, negative K_{DP}, and δ respectively, as in Section 4.2.4. Out of the three, negative K_{DP} has the least impact on most estimation methods, with both correlation coefficient and mean absolute error being very similar to the previous stage. The notable exception to this is the Maesaka method, which as previously mentioned does not allow for negative K_{DP} values, and so the observed decrease in correlation coefficient and increase in mean absolute error is expected.

This is a bigger factor for the Maesaka method than the UKMO method, which also does not estimate negative K_{DP}, due to how each method removes negative K_{DP}. The Maesaka method assumes from the start of the algorithm that Φ_{DP} can only increase, and so to most accurately reproduce Φ_{DP} it has narrower but larger changes when K_{DP} is not constant (for example, see the middle peak in Figure 4.8), whereas the UKMO method allows for Φ_{DP} to decrease, and estimates K_{DP} from a Φ_{DP} profile that includes decreasing Φ_{DP}; however, it removes negative K_{DP} as the last part of the estimation by setting all negative values to $0° \, km^{-1}$. This means that the estimated K_{DP} more closely follows the 'true' K_{DP} when K_{DP} is greater than $0° \, km^{-1}$ than the Maesaka method does, and so the correlation coefficient is not as affected for the UKMO method.

The inclusion of δ in the Ψ_{DP} profile (row 5 in figures 4.21 & 4.22) has a small effect on all methods. As seen in Figure 4.15, none of the methods completely remove the 'δ-bump' observed in the 'melting layer', and as a result the correlation coefficient decreases and the mean absolute error increases for all methods. This has the biggest effect on the profiles estimated using the Vulpiani method. As this estimated profile already has early peaks in K_{DP} compared to the 'truth', the addition of δ, which causes all the estimation methods to peak early in the 'melting layer', shifts the K_{DP} peak in the Vulpiani profile even further ahead of the 'true' K_{DP} peak, thus increasing the error.

Adding noise to the Ψ_{DP} profile generally has the largest impact on the estimated

profiles, some methods are more significantly affected than others. The wradlib method and Ryzhkov (high reflectivity) are most affected, with the short averaging windows used in the Ryzhkov (high reflectivity) and wradlib methods not able to smooth out the noise. This leads to significant decreases in correlation coefficient (from 1 to ∼0.65 and ∼0.59 for wradlib and Ryzhkov respectively), and large increases in the mean absolute error (from ∼0.01 to ∼0.27 and ∼0.24), much greater than any change seen as a result of the other two factors. The other methods are also affected by the addition of noise, although not as significantly - the Vulpiani estimated profile is slightly less affected by noise than by δ (correlation coefficient of ∼0.91 compared to ∼0.87, and similar mean absolute error). The Ryzhkov (low reflectivity) profile is the least affected, not just by noise but also by each of the other individual factors, with correlation coefficient dropping to ∼0.94 at the lowest and mean absolute error increasing to ∼0.08 at the most (both due to the addition of noise). This performance with a noisy Ψ_{DP} profile is in stark contrast to the same method in high reflectivity, potentially suggesting that the smaller averaging window does not have any advantage. However, it is also likely that in high reflectivity regions, K_{DP} might be higher and potentially fluctuate more than in this simple example, where the shorter averaging window would be of benefit.

The inclusion of noise is where the impact of interpolating between the missing Ψ_{DP} data points can become noticeable, albeit in an initially unexpected manner (compare Figures 4.23 & 4.24 with Figures 4.21 & 4.22). Particularly with the Schneebeli and the Vulpiani methods, interpolating the missing data points led to a worse estimation of K_{DP} than not interpolating, with both correlation coefficient decreasing and mean absolute error increasing. A hypothesis for this result is that only a simple linear interpolation was used, using just one data point either side of the missing points, and thus the noise was being included in the interpolation, resulting in a noisy value. If a few data points either side of the missing data point were used, the noise may have been smoothed out, resulting in a more accurate Ψ_{DP} value, and therefore a more accurate K_{DP} estimation at that location.

Pairing two of these factors, as discussed in Section 4.2.5, does not have much additional effect beyond what was observed by each factor individually. Rows 6, 7, & 8 in Figures 4.21 & 4.22 show the correlation coefficient and mean absolute error for each estimation method compared to the truth in the presence of noise and negative K_{DP} (row 6), noise and δ (row 7), and negative K_{DP} and δ (row 8). As the addition of noise generally had the greatest effect, the pair without noise (row 8) has the highest correlation coefficients. The exception to this is the Vulpiani method, which as mentioned previously is more affected by δ than noise. Using the raw, non-interpolated Ψ_{DP} profile, the Vulpiani

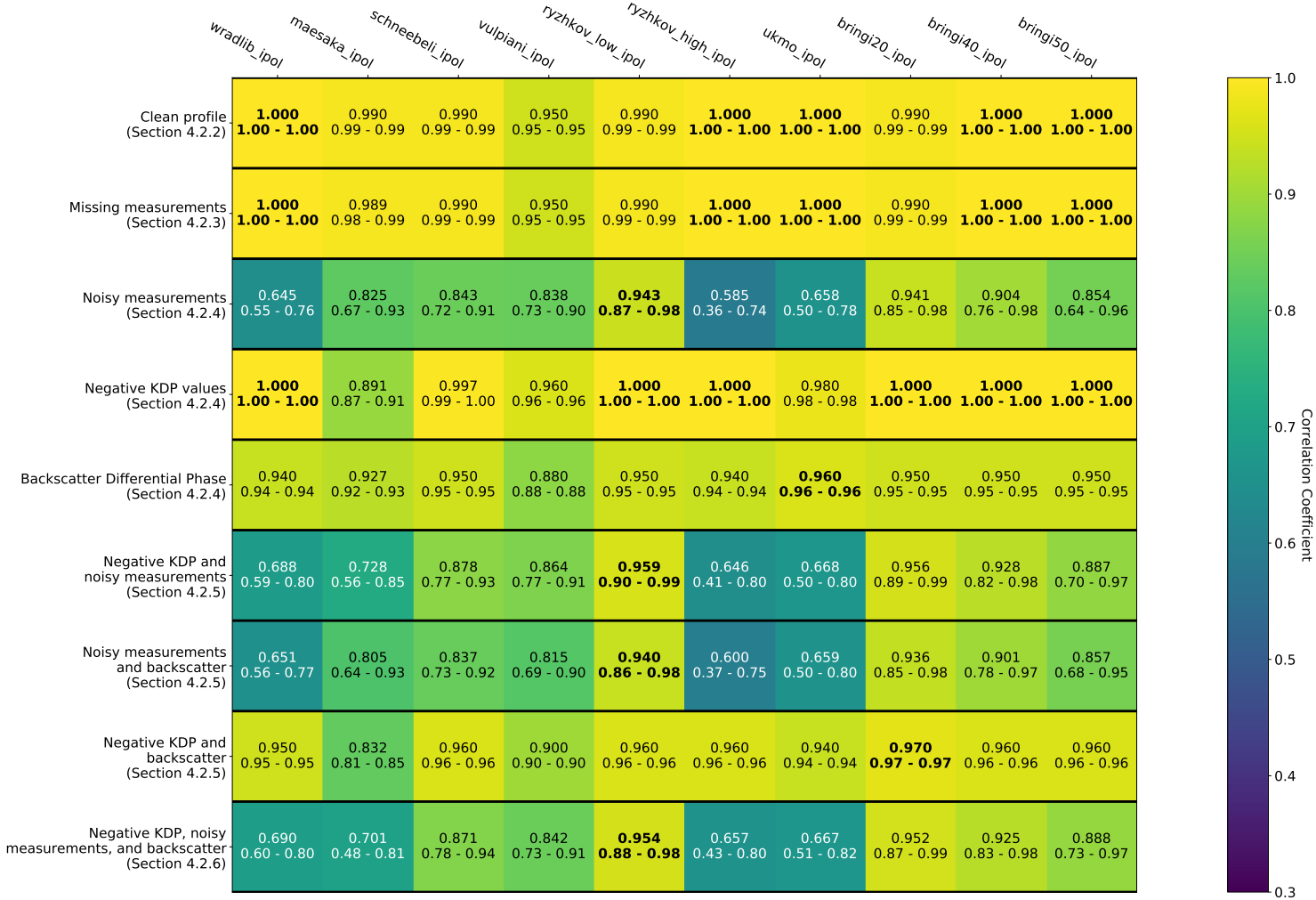

Figure 4.23: Same as Fig.4.21, but with the Ψ_{DP} profile interpolated before K_{DP} estimation. The highest values in each row are in bold type.

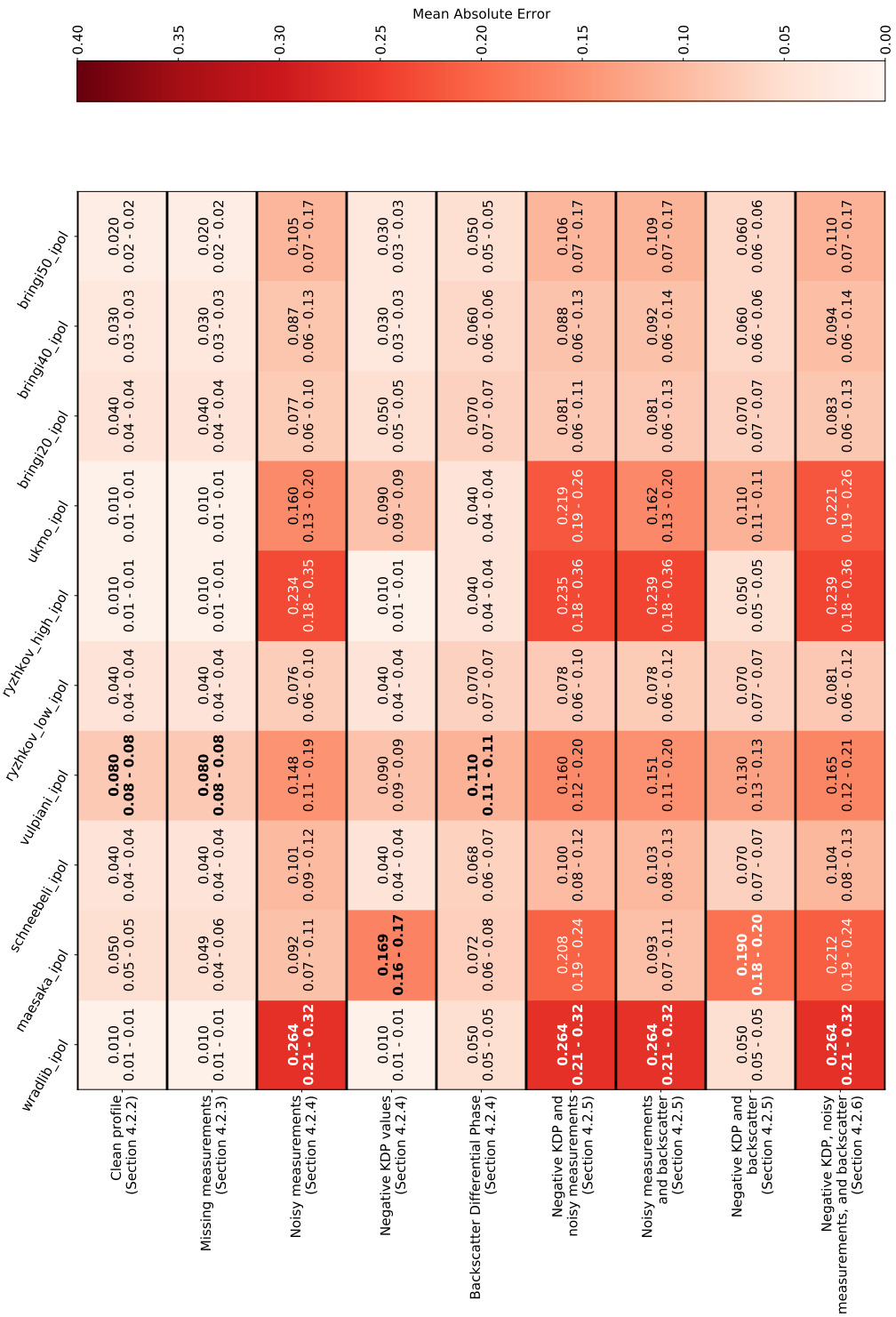

Figure 4.24: Same as Fig.4.22, but with the Ψ_{DP} profile interpolated before K_{DP} estimation. The lowest values in each row are in bold type.

estimation has a higher correlation coefficient in the no-δ pair (row 6); however, when using the interpolated Ψ_{DP} data the issue mentioned in the previous paragraph means that the no-noise pair (row 8) has the highest correlation coefficient.

The final row in Figures 4.21 & 4.22 show the results from Section 4.2.7, where negative K_{DP}, δ, and noise are all included in the Ψ_{DP} profile. The Ryzhkov method covers both extremes, with the low reflectivity version producing the highest correlation coefficient ($\sim$0.96) and lowest mean absolute error ($\sim$0.08), while the shorter averaging window associated with high reflectivity results in the lowest correlation coefficient ($\sim$0.66) and second highest mean absolute error ($\sim$0.24, compared to $\sim$0.27 for the wradlib method). This suggests that while this method works well in low reflectivity areas, for example in ice or low to moderate rain, when reflectivity is high and factors such as noise and δ are more likely, for example heavy rain or in the melting layer, then this method is less capable. The Vulpiani and Schneebeli methods both perform well, with high correlation coefficient ($\sim$0.88 and $\sim$0.90) and low mean absolute error ($\sim$0.14 and $\sim$0.11), suggesting they perform well over the entire range of the Ψ_{DP} profile and, while not perfect as seen previously, they both deal with noise and δ well. These methods also show a small range across the ensembles, suggesting that the noise is dealt with well and consistently. The Vulpiani method may perform better with some sort of supervision to line up the peaks correctly; however, when using real data, one would not know how much the K_{DP} profile needs shifting, therefore a more extensive study would need to be conducted.

4.2.8 Different 'true' profiles

So far, only one 'true' K_{DP} profile has been considered, with values ranging from -0.2° km^{-1} to 1° km^{-1}, with periods of constant -0.2° km^{-1} (truncated at 0° km^{-1} when not including negative values). In this section, three other 'true' profiles are simulated using the same process as outlined so far throughout this chapter, one where the values in the K_{DP} profile are doubled, one where they are halved, and one where the values are increased by 1° km^{-1}, such that an entire sine wave is captured between 0° km^{-1} and 2° km^{-1}. These 'truths' are shown in figure 4.25. The correlation coefficient and mean absolute error for each method at the final Ψ_{DP} stage above, that is including noise, backscatter and negative values, is shown in Figs.4.26 & 4.27 for all four 'true' profiles.

The statistics shown in Figures 4.26 & 4.27 show that the strength of correlation and size

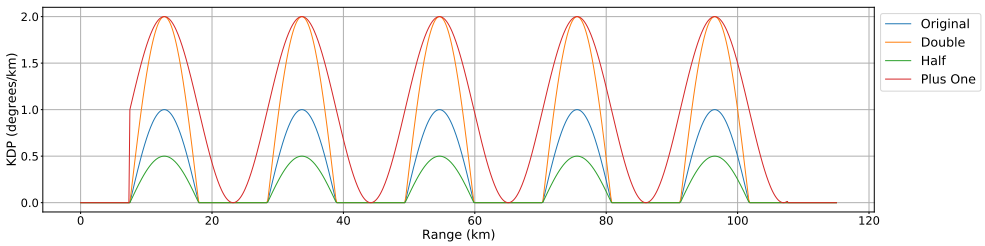

Figure 4.25: Four different 'true' K_{DP} profiles used. "Double", "Half", and "Plus One" describe how those profiles relate to the "Original" profile before truncation of negative values.

of error do change slightly with different 'true' K_{DP} profiles; however, the changes to correlation and error can be easily understood. Increasing the size of the 'truth' profile increases the correlation coefficient, but also increases the mean absolute error. This is because the miscalculation at the turning points in the profile results in larger errors, although doubling the 'true' profile does not double the error, and so the correlation coefficient increases. This change is further exaggerated in the 'Plus One' profile, which encapsulates an entire sine wave and does not have the constant K_{DP} sections between the K_{DP} peaks. Here, the mean absolute error increases as there is incorrect estimation with both peaks and troughs in the 'true' K_{DP} profile, but good estimation along the gradual slope in the profile between the two, rather than the sharp change between constant and changing K_{DP} seen in the previous 'truths', results in increased correlation coefficients.

4.3 Comparison using real Ψ_{DP} measurements

After comparing these different methods to a known 'truth', it is important to look at some observations. However, as previously mentioned, there is no 'truth', so instead the estimation methods are compared to each other, to look for similarities between the estimations, or for any extreme irregularities. Radar data was taken from the NCAS Mobile X-Band Radar from 26 days between 15$^{\text{th}}$ January 2018 and 27$^{\text{th}}$ March 2018 on which precipitation was measured at Chilbolton Observatory, where the radar was located during this time as part of the PICASSO campaign. Firstly, two individual rays are studied as an example, and then statistics are derived from all 26 days.

Figures 4.28 & 4.29 show the estimated K_{DP} profiles for two rays, one at a 1° elevation primarily below the melting layer (Figure 4.28) and one at a 6° elevation which travels through the melting layer early in the ray. Similar plots for Φ_{DP}, and the standard

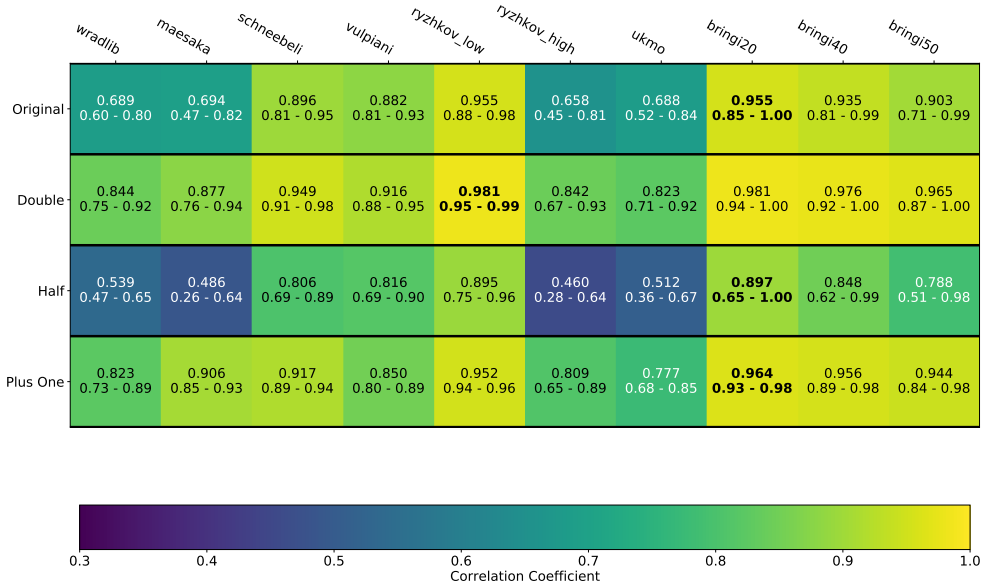

Figure 4.26: Correlation Coefficient for each method at the final Ψ_{DP} stage compared to four 'true' K_{DP} profiles: "Original" is the same 'truth' as throughout this chapter, "Double" is double "Original", "Half" is half "Original", and "Plus One" is "Original" increased by $1° \, km^{-1}$, as shown in figure 4.25. The central number in each box is the mean correlation coefficient from all ensemble members, beneath is the minimum and maximum coefficients.

deviation of Φ_{DP} from equation 2.15, are shown in figures 4.30 & 4.31. While only these two rays are shown here, the patterns seen in them are representative of those observed in other rays.

Visually, the greatest issue is with the wradlib profile. In Figure 4.28, there is a very large spike in K_{DP} at the start of the profile, and then nothing for the rest of ray. This is in stark contrast to Figure 4.29, where the wradlib estimation produces the most extreme values of K_{DP} with large fluctuations along the ray when compared to the other methods, which are mostly much smoother, matching the simulations throughout section 4.2. This explains why the wradlib K_{DP} estimation method has no correlation with the other methods (figure 4.32), and is likely an issue in the wradlib code.

The next method which appears to have comparatively larger fluctuations is the UKMO method. This is in agreement with the observations on the simulated truth, particularly Figures 4.4 & 4.12, where firstly missing Ψ_{DP} values caused problems for the estimation, and then the addition of noise to the profile was amplified through the K_{DP} estimation.

The other estimation methods mostly follow a similar profile along both of the rays, with the Schneebeli method producing a slightly noisier profile, again following the

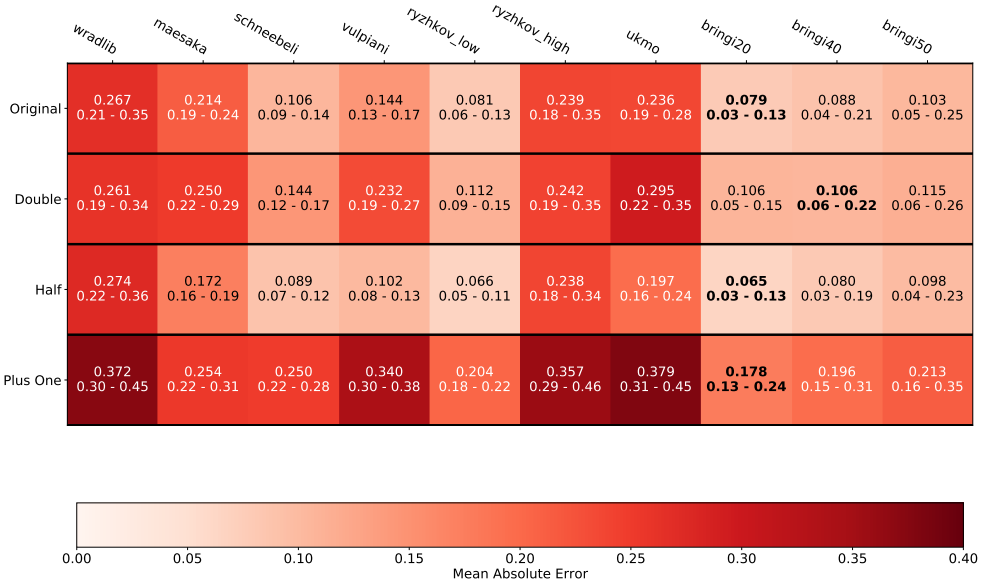

Figure 4.27: Same as Fig.4.26, but showing Mean Absolute Error.

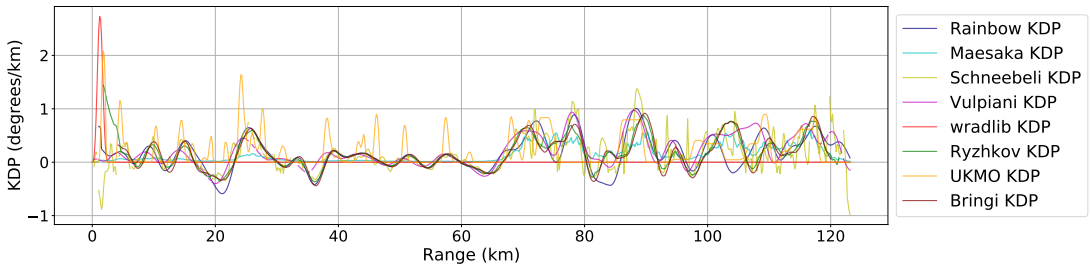

Figure 4.28: Estimated K_{DP} profiles from a 1° elevation scan at 13:24:32 UTC on 17 May 2017.

trend seen in the simulated profiles when noise was added to the 'truth' (Figure 4.12). The Maesaka estimation smooths out the small K_{DP} values, especially early in the profile, although as the other methods start predicting larger K_{DP} values, for example within the melting layer and into the ice region, then the Maesaka method estimates similar values of K_{DP}.

Having looked in detail at these two rays, K_{DP} is estimated by each method for PPI scans from 26 days between 15$^{\text{th}}$ January 2018 and 27$^{\text{th}}$ March 2018 during which rain was observed at Chilbolton Observatory to give more of a bigger picture of how similar the estimated profiles by each method are. The mean correlation coefficient between each K_{DP} estimation method for each PPI scan is shown in figure 4.32. The wradlib method stands out as calculating completely different K_{DP} profiles to each of the other methods. Closer inspection of some individual profiles, for example Figure 4.28, show

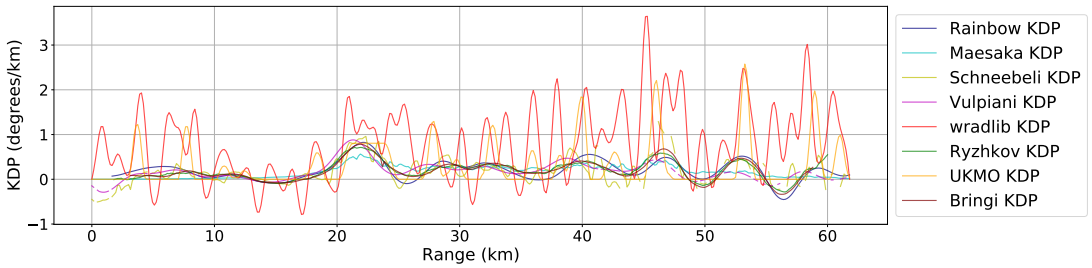

Figure 4.29: Same as Fig.4.28, but with an elevation of 6°.

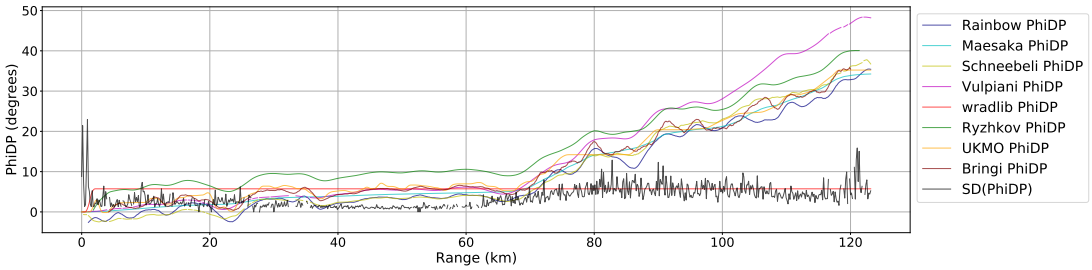

Figure 4.30: Same as figure 4.28, but showing Φ_{DP} and the standard deviation of Φ_{DP} as calculated by equation 2.15.

that occasionally there is an error in the computation of K_{DP} by the wradlib code which results in most of the K_{DP} profile estimated as $0° \, km^{-1}$.

Amongst the other methods, the highest correlations are found between the Rainbow K_{DP} method, Ryzhkov K_{DP} method, and Bringi K_{DP} method. These methods also share low deviations in correlation from volume to volume (Figure 4.33). The similarity between Rainbow K_{DP} and Bringi K_{DP} is unsurprising, as they use similar methods in their estimation; however, the inclusion of the Ryzhkov K_{DP} estimation method, and its especially high correlation with the Bringi K_{DP} method, is more surprising, as the Ryzhkov K_{DP} method is the simplest of methods used in this study, just using a moving averaging window, with a threshold on window size at 40 dBZ. In these PPI volumes, there is very little data with reflectivity over 40 dBZ, therefore most of the Ryzhkov K_{DP} is estimated using the larger window size in the method, which has the effect of more aggressively smoothing any sudden changes in Ψ_{DP}. While the comparisons through Section 4.2 suggest that the Ryzhkov method appeared to give profiles better matching the 'true' profiles in the lower reflectivity regions, particularly with noisy Ψ_{DP} measurements, it may be that in real observations the smaller averaging window at high reflectivity produces better K_{DP} estimations in those regions; however, further study would need to be done to confirm this, and whether the 40 dBZ threshold is still suitable for UK weather conditions.

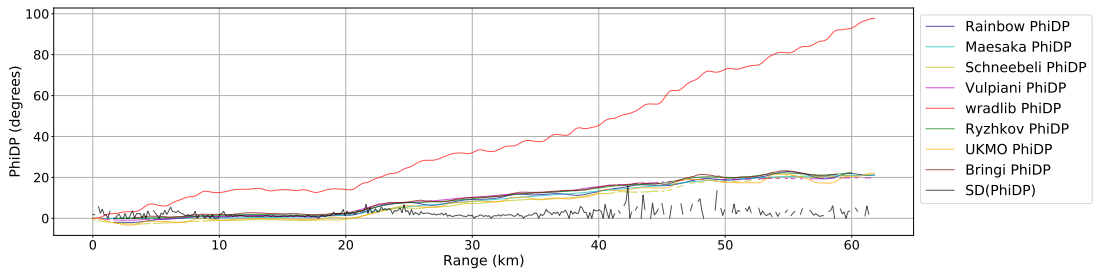

Figure 4.31: Same as figure 4.29, but showing Φ_{DP} and the standard deviation of Φ_{DP} as calculated by equation 2.15.

4.4 Summary

There are many methods to choose from to estimate K_{DP} from the measured Ψ_{DP} profile, with different levels of complexity. Eight of these methods are tested and compared in this chapter, seven on an artificial Ψ_{DP} profile, and all eight using real data. Two of these methods use different averaging window sizes depending on the reflectivity value; they were both tested with a constant reflectivity profile either side of each threshold for the artificial data.

Out of the three factors additional to K_{DP} in the Ψ_{DP} profile, noise has the biggest effect on the accuracy of the K_{DP} estimation. While the estimated profiles still follow the general profile of the 'truth', there is an oscillation in the estimations around the 'truth' in most of the profiles due to the noise, with the methods that use the largest averaging windows, and therefore greatest smoothing, least affected, for example the Ryzhkov and Bringi methods in low reflectivity, and the Vulpiani method. However, the Ryzhkov method for high reflectivity, the UKMO method, and the wradlib method, all show a lot of noise in the estimated profiles, especially in the defined melting layer in the middle of the profile, and these methods have the biggest drop in correlation coefficient when compared to the artificial 'true' profile, and the biggest increase in mean absolute error. The Bringi method appears to deal best with noise, with high correlation coefficients and low mean absolute error for all reflectivity thresholds (third row in figures 4.21 & 4.22). While it might therefore be easy to assume that just using the largest averaging or smoothing window at all times is the best approach, this will miss any fluctuations in K_{DP} on a scale smaller than the averaging window used, and work by Gorgucci et al. (1999b) has shown that changes in reflectivity within the averaging window can lead to inaccurate K_{DP} estimations.

All of the methods fail to remove the backscatter differential phase, resulting in over-

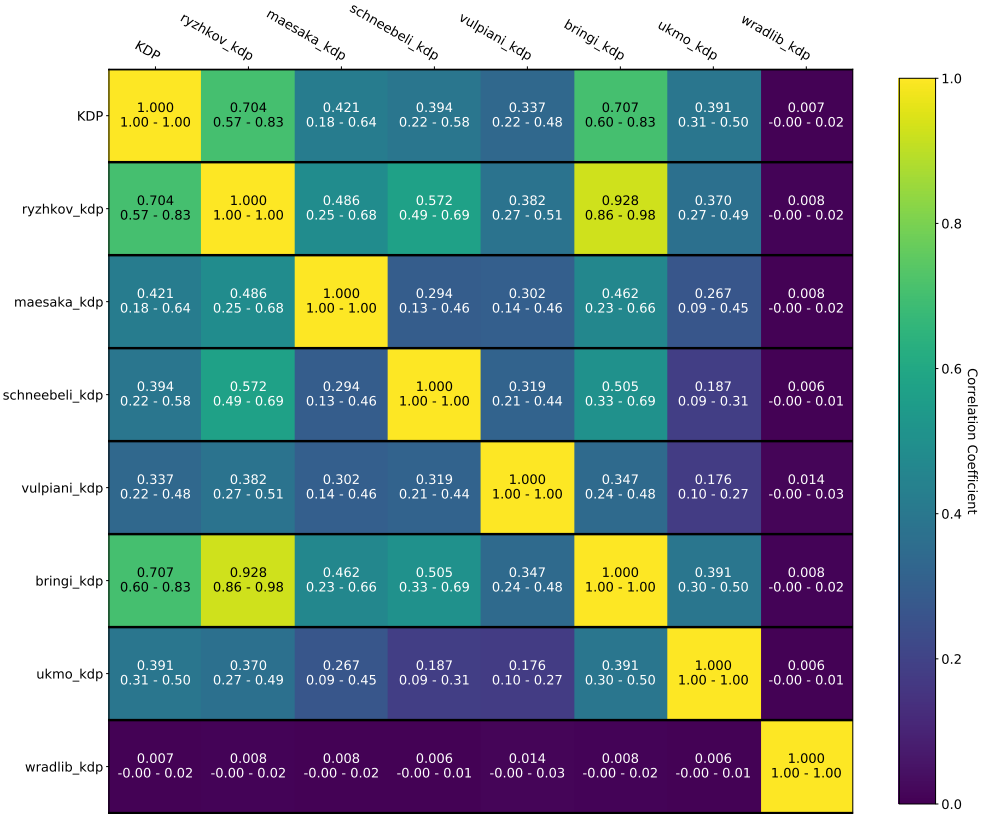

Figure 4.32: The mean correlation coefficient between two K_{DP} estimation methods, averaged over many PPI scans, with minimum and maximum correlation values included for each pairing.

estimation in K_{DP} before the peak of the 'δ-bump' in the melting layer, and underestimation afterwards. This includes the methods that explicitly resolve, or attempt to remove, δ. However, the finite impulse response filter used on the Bringi method does the most to reduce the effect of δ, resulting in a peak in K_{DP} that is closest in location to the peak of the 'true' K_{DP}, and the value of K_{DP} in the low reflectivity case is almost the same as that in the low reflectivity Ryzhkov, which are two of the closest to the 'truth'. In high reflectivity, as might be observed in the melting layer, the Bringi method performs better than the Ryzhkov method in the presence of δ, resulting in higher correlation coefficients and lower mean absolute error for the Bringi method when compared to the artificial truth than for the Ryzhkov method (fifth row in figures 4.21 & 4.22).

In profiles of Ψ_{DP} that do not have noise, a simple linear interpolation between missing data before estimating K_{DP} improves the estimated profile, particularly in the UKMO estimation method due to it not removing missing data before estimation, and those

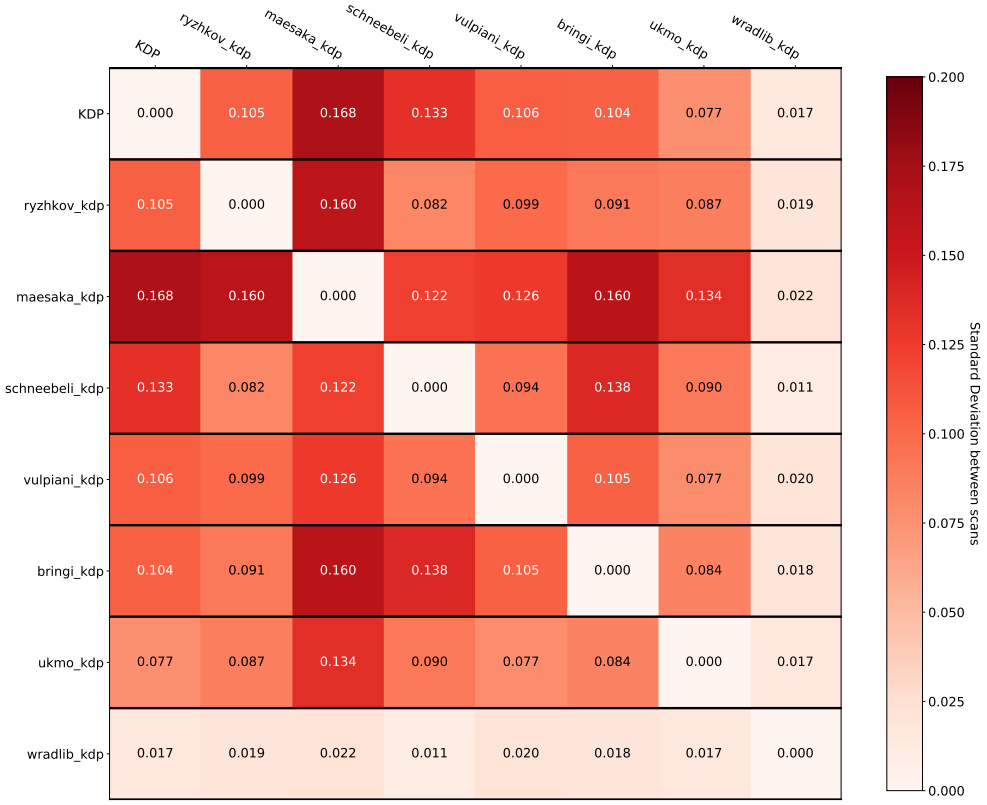

Figure 4.33: Same as Fig.4.32, but showing standard deviation of the correlation coefficients between PPI scans.

that do not estimate K_{DP} in the vicinity of missing data, for example the Bringi method. However, this interpolation has the opposite effect in noisy data. Linearly interpolating between noisy data points may lead to a more inaccurate Ψ_{DP} profile, which results in a more inaccurate K_{DP} estimation. This is most pronounced in the Schneebeli and Vulpiani methods, with decreases in correlation coefficient and increases in mean absolute error. This leaves two options for estimating K_{DP} in real world data, either use an estimation method that does not need a continuous Ψ_{DP} profile to estimate from, or do the interpolation based on a smoothed Φ_{DP} profile, rather than on the noisy observations.

As a result of how the finite impulse response filter deals with the large increase in backscatter differential phase through the melting layer, and with noise throughout the profile, the Bringi method returns the best statistics overall. However, the Bringi method does not deal well with individual missing data points along the ray, which can result in large gaps in the estimated K_{DP} profile. After linearly interpolating the Ψ_{DP} profile before applying the estimation methods, the Ryzhkov method returns similar, if

not very slightly better, statistics than the Bringi method in the low reflectivity region for the Ryzhkov method (below 40 dBZ); however, the small averaging window used by Ryzhkov for larger reflectivity results in much smaller correlation coefficients and higher mean absolute errors than the mid and high reflectivity versions of the Bringi method (figures 4.23 & 4.24).

When looking at real data, the spread between the different methods is quite large, with the correlation coefficient between most methods being quite low (below 0.4). However, three of the methods produce K_{DP} profiles that are close to each other: the Rainbow method (which could not be included in the artificial data study), the Bringi method, and the Ryzhkov method. The Rainbow method and the Bringi method use a similar methodology, and as such it is not surprising they produce similar results. The Ryzhkov method is the simplest of the methods used, just smoothing the Ψ_{DP} profile using an averaging window, and a slope from a least squares linear fit to estimate K_{DP}. This method is also surprising given the noisy estimations observed in the artificial data when there is significant noise in the Ψ_{DP} profile in the high reflectivity regime. However, the data used here has very few observations that fall in the high reflectivity regime ($>$ 40 dBZ), suggesting either the threshold may need to be adjusted for different weather regimes and different radars, or that the removal of convective weather from the study also removed the majority of the data that would meet this threshold.

Though the Bringi method appears to provide the best results, based on the results of the first section of this chapter, given the observed similarities between the Rainbow and Bringi methods shown in the second section of this chapter, and the fact that NXPol-1 natively calculates K_{DP} with the Rainbow method, the Rainbow method will be used throughout the rest of this thesis. These results suggest that no other method would provide a meaningful improvement in K_{DP} estimation compared to what is currently available. However, with the diversity in estimations, one method can not be unequivocally chosen as 'better' than the others. There may be one method, or a combination of methods, which is better in certain cases, for certain weather patterns or a particular radar. This also means that retrieval relations for microphysical quantities, such as rain rate or liquid or ice water contents, derived using one K_{DP} estimation method or on one radar system or network, might not have the desired accuracy for another estimation method or radar. Therefore, where the necessary observations are present or can be obtained, these relations will be most accurate if tuned or derived for each radar system and method individually.

Chapter 5

Variation in K_{DP} with radar elevation angle

One of the benefits of using specific differential phase over reflectivity measurements is that K_{DP} is not affected by attenuation. However, a number of the uses of K_{DP} (for example hydrometeor classification and quantitative precipitation estimation) also rely on reflectivity measurements, and so the effects due to attenuation need to be considered. This is particularly true for X band radars, where the shorter wavelength used compared to other weather radars means attenuation is more of an issue. One method of doing this is to limit the maximum distance from the radar in which measurements are used. For example, Bechini et al. (2013) used data within 50 km of the radar, Matrosov et al. (2005) used PPI scans with a maximum range of 57.6 km, the radars in the Collaborative Adaptive Sensing of the Atmosphere (CASA) network have a maximum range of 30 km (Brotzge et al. 2006), and Wolfensberger et al. (2016) limited observations to just within 5 km.

When limiting usable data to short distances, higher elevation angles are needed to study the melting layer or ice regions of clouds. A melting layer 2 km above the radar requires an elevation angle of 11° at a distance of 10 km from the radar, or 22° at 5 km. To observe the dendritic growth layer at around -15 °C, roughly 3 km above the melting layer, the required elevation angle needed is 27° or 45° at distance 10 km or 5 km respectively. The impact of elevation angle on differential reflectivity is well known (Ryzhkov et al. 2005a), with commonly used Z_{DR} calibration technique based on the assumption that the average Z_{DR} being zero when the radar is pointing vertically (Gorgucci et al. 1992; Bechini et al. 2008).

A relation between K_{DP} and elevation angle has previously been theoretically derived

(Schneebeli et al. 2013; Lu et al. 2015), although it has not been shown by observational studies. Also, due to the small values in K_{DP} and the uncertainty in its estimation, these relations are unstable for the highest elevation angles. Equation 9 in Schneebeli et al. (2013), which is

$$K_{DP}(\theta = 0) = \frac{2K_{DP}(\theta \neq 0)}{1 + cos(2\theta)}, \tag{5.1}$$

shows that while changes to K_{DP} are small when going from low elevation angles ($\theta < 20°$) to $\theta = 0$, while this multiplicative factor can be more significant for higher elevation angles (see Figure 5.1). This multiplier affects not only the 'true' K_{DP}, but also the errors and uncertainty in the estimated K_{DP} value. Table 5.1 shows how an error of 0.05 $^\circ\, km^{-1}$ at different elevation angles would propagate through to 0° elevation angle. Therefore, if using K_{DP} at high altitudes for hydrometeor classification or short term precipitation forecasting (Bechini et al. 2013), a small error in estimation can propagate through to incorrect classification or precipitation estimation.

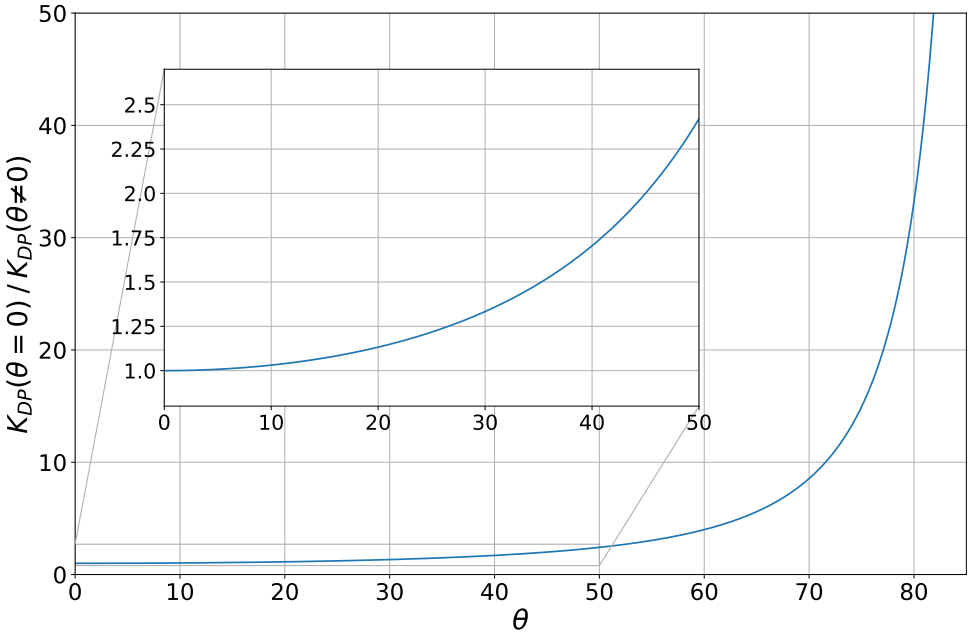

Figure 5.1: Multiplication factor when adjusting K_{DP} to 0° elevation based on equation 9 in Schneebeli et al. (2013).

The two main aims of this chapter are (1) to use observations to confirm the relationship between K_{DP} and elevation angle, and (2) to study if other available data can be used to constrain adjusted K_{DP} from high elevation angles. This chapter uses observational data from the NXPol-1 radar to study the relationship between K_{DP} and elevation angle, first through a few small case studies and then a larger study using 3 months

θ (°)	Multiplier	Adjusted Error ($^\circ\, km^{-1}$)
20	1.13	0.057
50	2.42	0.12
70	8.55	0.43
80	33.16	1.66

Table 5.1: Change in 0.05 $^\circ\, km^{-1}$ error of K_{DP} adjusted to an elevation of 0° from various elevation angles.

of observations. Evidence for a physical understanding of the observations is also presented, along with an example from hydrometeor classification of the importance of correctly estimating K_{DP}.

5.1 Case Studies

Three 1 hour long case studies are selected for initial study. These three hours are 1100-1200 17 May 2017 (Figure 5.2), 1700-1800 5 June 2017 (Figure 5.3), and 0100-0200 12 July 2017 (Figure 5.4). These three periods were chosen because they were times of stratiform rainfall associated with frontal activity due to low pressure systems from the Atlantic Ocean, with at least two hours of sustained rainfall observed at Chilbolton Observatory in each case. By limiting data to times when stratiform rainfall was observed, the clouds present are more likely to be well developed, with vertical structure that would enable comparison at different temperatures. The limitation of stratiform rainfall, rather than convective, also increases the likelihood of horizontal homogeneity, meaning that it is more likely that what the radar observed directly overhead was the same as at a distance further away, and therefore any change in observed values is more likely due to the change in radar elevation angle, as opposed to a change in hydrometeor type. This can be seen in figures 5.2, 5.3 & 5.4, where in all three cases there is consistency in the vertical structure throughout the RHI.

Figure 5.5 shows K_{DP} against elevation angles from all the RHI observations for each of these case studies for data points with a temperature of -15 °C ± 0.5 °C, with each data point coloured by the reflectivity measured at that location. In two of these case studies (Figures 5.5a,c), for temperatures below 0 °C where ice is dominant, K_{DP} has a large value (over 0.5 $^\circ\, km^{-1}$) when observed at low elevation angles (between 0 ° and 20 °), but K_{DP} decreases to 0 $^\circ\, km^{-1}$ as elevation angle increases, as predicted by the equations in Schneebeli et al. (2013) and Lu et al. (2015). However, in the third of these cases (Figure 5.5b, 5$^{\text{th}}$ June 2017), such an angular change in K_{DP} is not

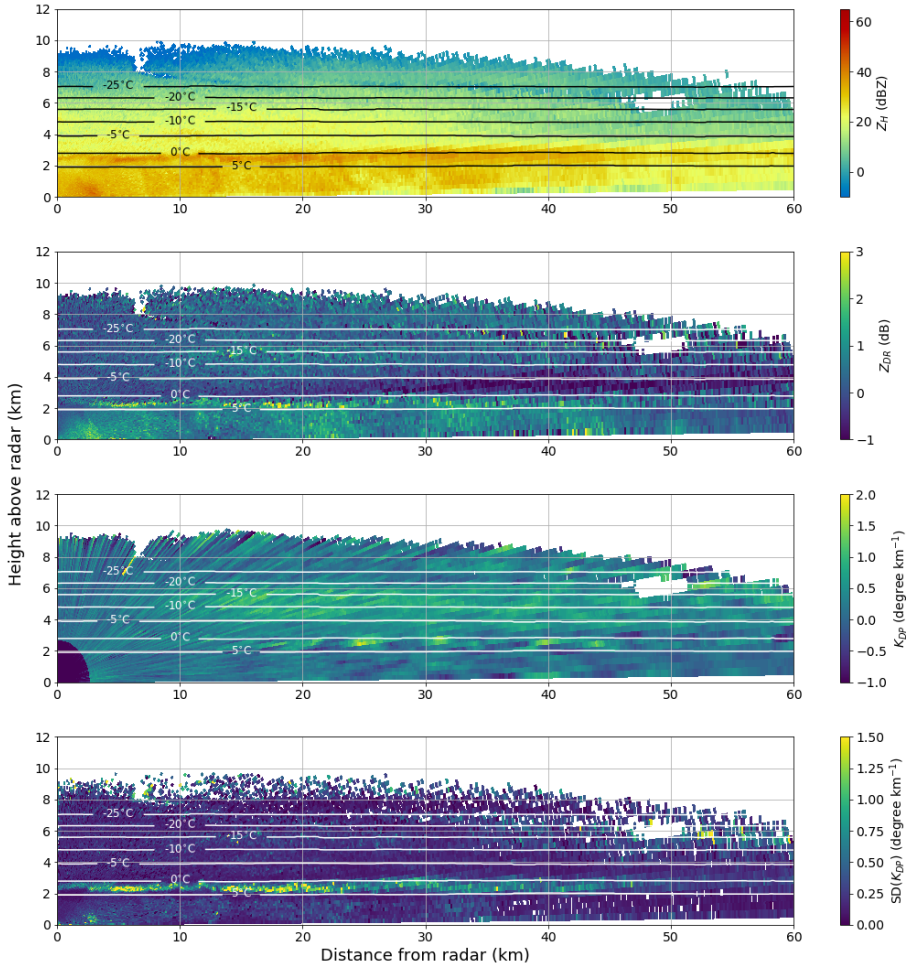

Figure 5.2: From the top, reflectivity factor from horizontal polarization, differential reflectivity, and specific differential phase measured by 248° RHI scan at 11:36:54 UTC 17 May 2017, and at the bottom the standard deviation of specific differential phase as calculated by Equation 2.16. On each RHI are contours of temperature from the UK Met Office model regridded to the radar co-ordinates.

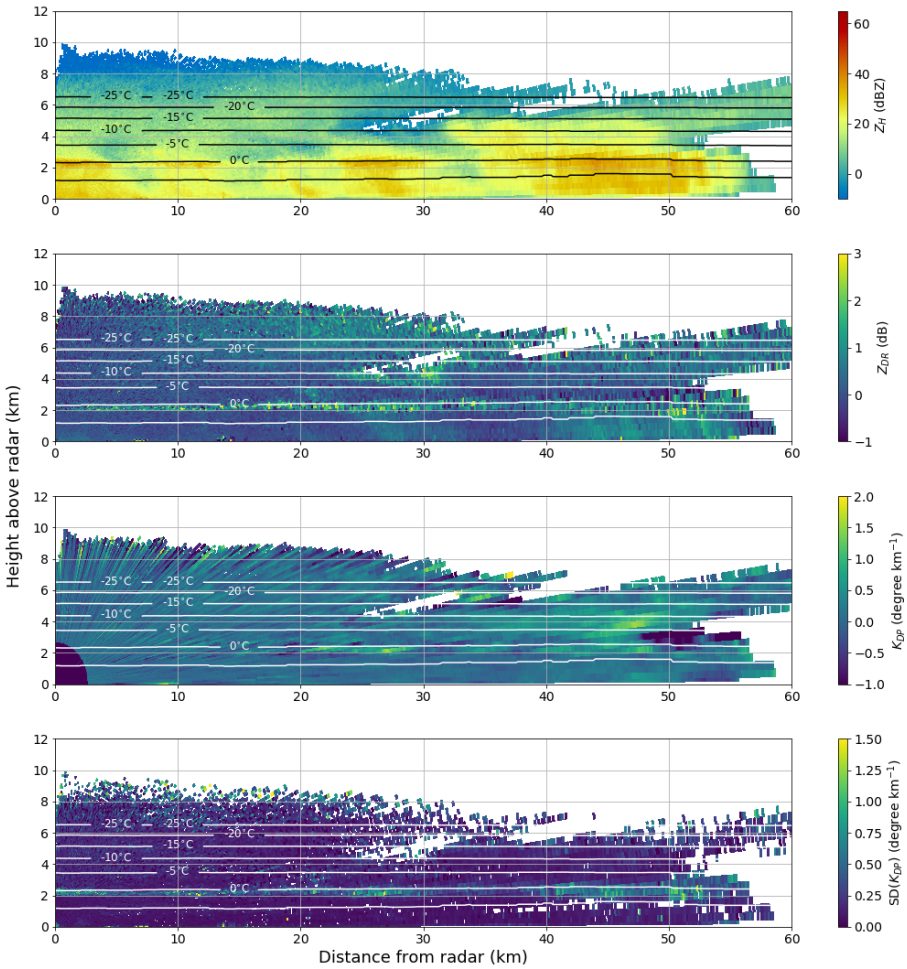

Figure 5.3: Same as Fig. 5.2, for 17:08:12 UTC 5$^{\text{th}}$ June 2017.

observed. The measured reflectivity in this case is lower than in the other two (∼10 dBZ compared to ∼20 dBZ), which along with the different K_{DP} measured at low elevation angles suggests that there is a difference in the hydrometeors being observed between this case study and the other two.

Data from the same hours are also plotted for a temperature of +5 °C (Figure 5.6). While there is little data available for the highest elevation angles, there is no sign of a strong change in K_{DP} with elevation angle in any of the case studies, with low K_{DP} observed at low elevation angles in all, regardless of reflectivity. This may suggest that knowing temperature, as well as reflectivity, may help improve the adjustment to K_{DP} needed between high and low elevation angles.

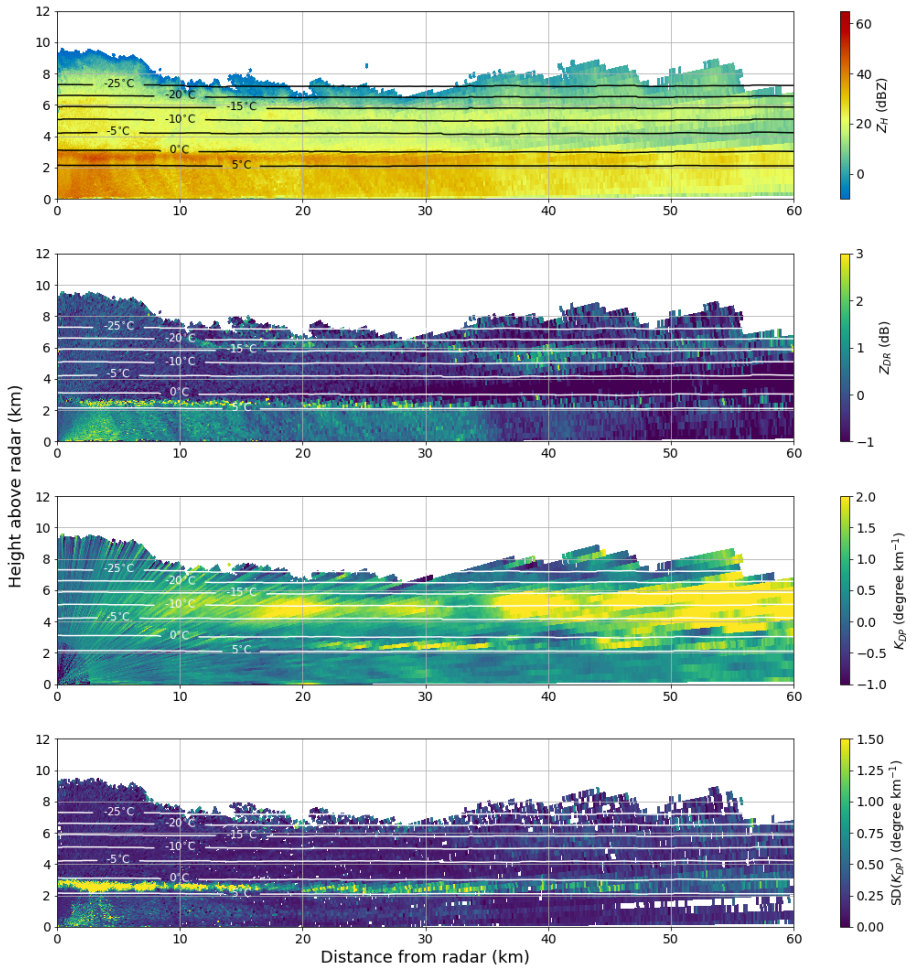

Figure 5.4: Same as Fig. 5.2, for 01:13:18 UTC 12th July 2017.

5.2 Discussion of physical understanding

Images taken from the CIP-15 probe on a FAAM flight on 17th May 2017 (radar observations and modelled temperature in figure 5.2) were examined visually to determine if any patterns or dominant ice habits existed. A selection of these images are shown in figure 5.7, representing the large number of images available. Observations from the entire flight were binned by temperature in a similar fashion to the radar observations. In matching with the changes of reflectivity seen by temperature, hydrometeors tended to increase in size as altitude decreases and temperature warmed, from mostly small plates and columns crystals at -25 °C to larger aggregates at around -5 °C - 0 °C, and then raindrops at +5 °C (figure 5.7).

The observed size and shape of the hydrometeors matches what is expected based on

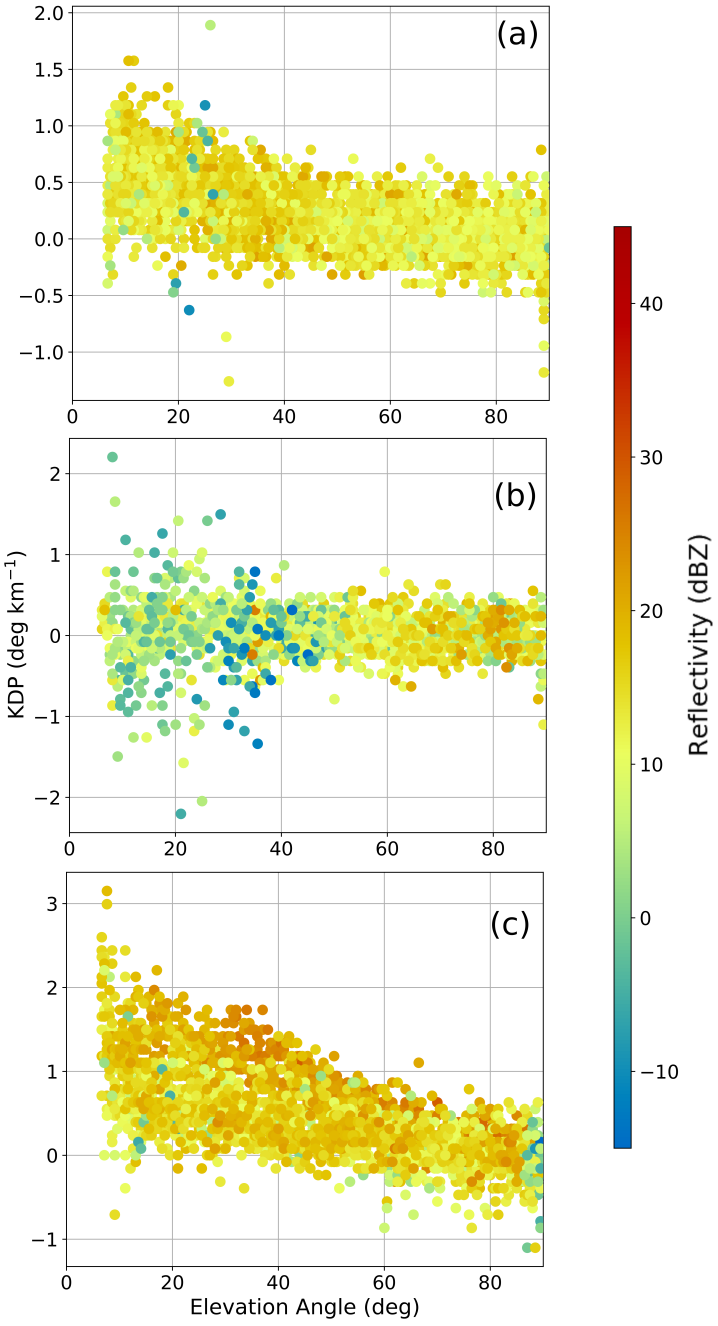

Figure 5.5: K_{DP} against elevation angle at -15 °C for all RHI scans between (a) 1100 UTC and 1200 UTC 17th May 2017, (b) 1700 UTC and 1800 UTC 5th June 2017, and (c) 0100 UTC and 0200 UTC 12th July 2017.

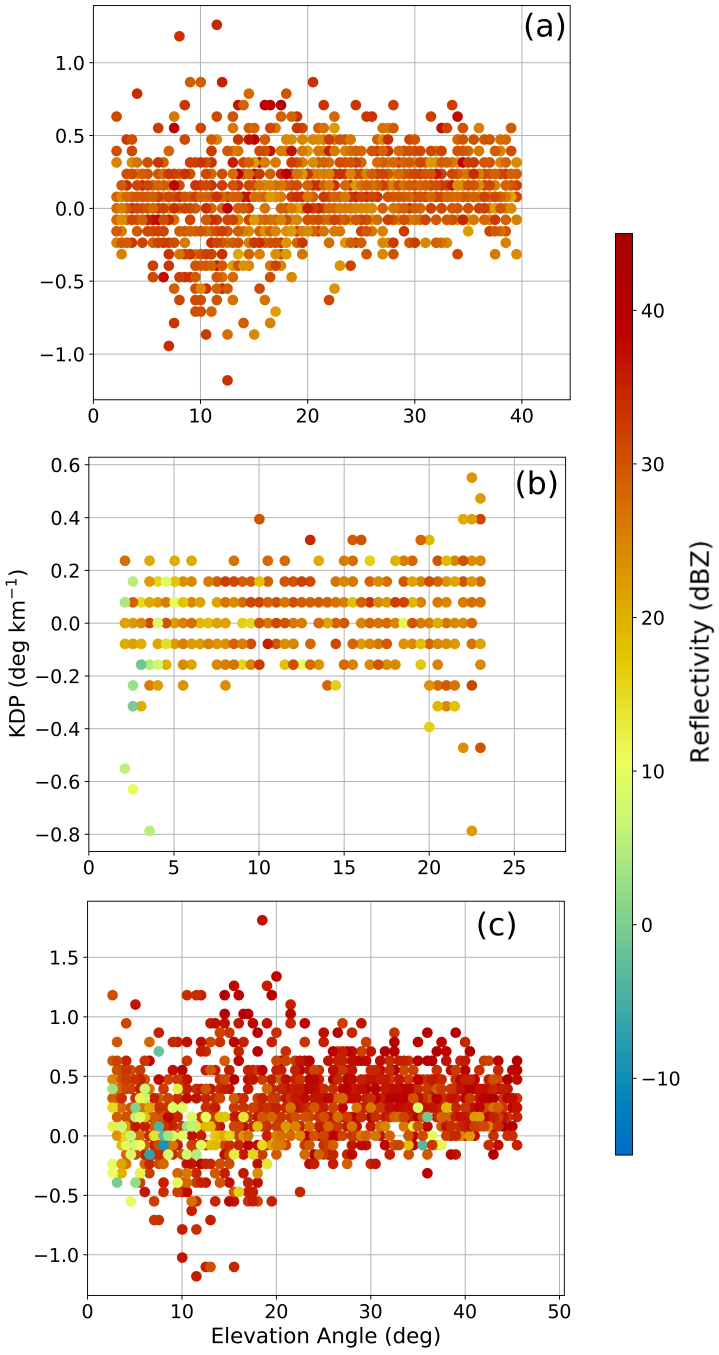

Figure 5.6: Same as Fig. 5.5, for +5 °C.

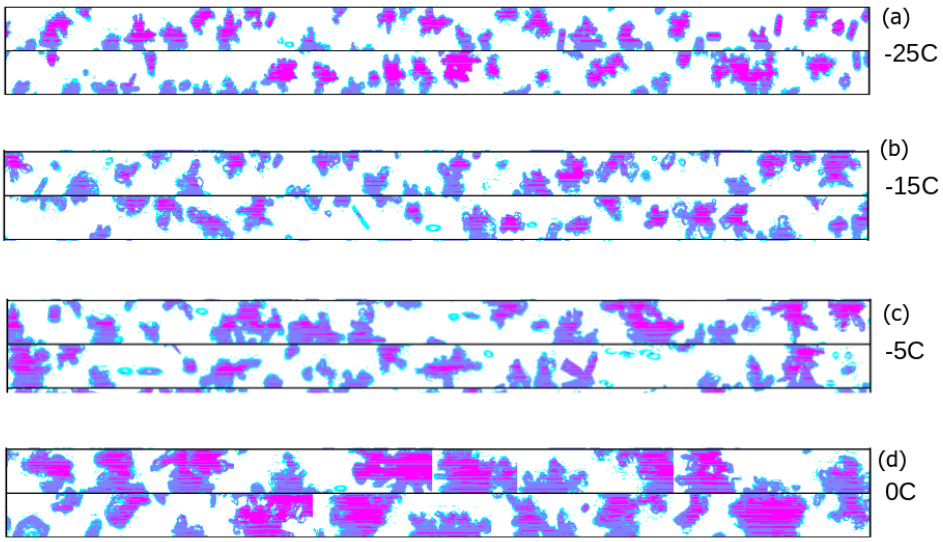

Figure 5.7: Images from the CIP-15 probe aboard the FAAM aircraft flight on 17$^{\text{th}}$ May 2017, at temperatures of (a) -25 °C, (b) -15 °C, (c) -5 °C, and (d) 0 °C.

the radar observations and known ice crystal behaviour. At the lowest temperatures (-25 °C), the dominant hydrometeor type is small, pristine ice crystals, which are small in size and so have small reflectivity. As shown in figure 5.8, a volume of pristine plate and column crystals, which tend to fall with horizontal orientation (Willmarth et al. 1964; Westbrook et al. 2010) and are observed at colder temperatures within clouds, result in positive K_{DP} when viewed from the side, i.e. a low radar elevation angle. However, the smallest of these (associated with the small values of reflectivity) have the smallest K_{DP}, as their size means they have little effect on the propagation of the radar wave, and having less time to grow means they are closer to spherical (at least in absolute dimensions $(a - b)$, not necessarily relative dimensions or aspect ratio (a/b)). Therefore, smaller ice crystals will have K_{DP} close to 0 $^\circ\, km^{-1}$ at the low elevation angles. Larger ice crystals, which have had more time to grow and are associated with higher reflectivity, will have grown into the shape determined by their habit type, increasing the differential impact on the propagation of the radar beam, and hence resulting in higher K_{DP} when viewed at lower elevation angles (Andrić et al. 2013). However, when viewed from beneath, the apparent axis ratio for plates will be $\sim$1, and the random orientation of columns within the volume observed by a radar will also result in an average axis ratio of $\sim$1, regardless of ice crystal size, so as the radar points vertically, K_{DP} will tend toward 0 $^\circ\, km^{-1}$ in these regions, as observed.

Between -10 °C and -20 °C dendritic growth can occur in areas of high ice supersatura-

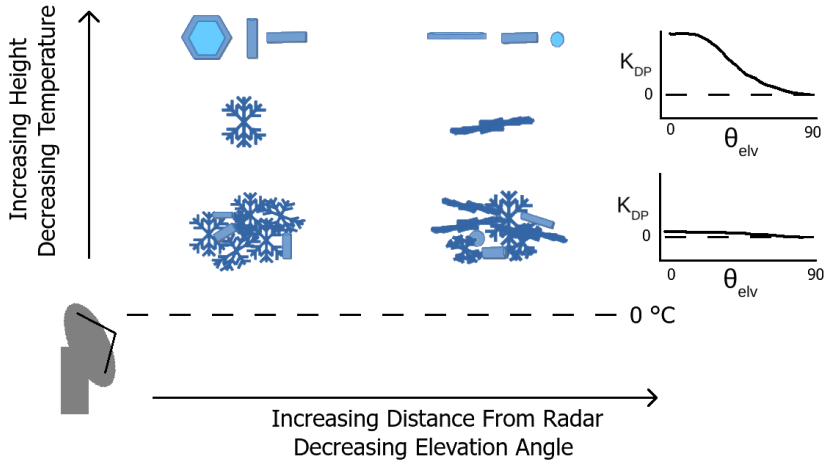

Figure 5.8: Sketch showing view of different hydrometeors to the radar from different elevation angles, highlighting the change in K_{DP} with elevation angle.

tion. In radar observations, this manifests in increased reflectivity and increased K_{DP}, with the increased K_{DP} observable at lower elevation angles. This agrees with studies such as Kennedy and Rutledge (2011), Bechini et al. (2013), Moisseev et al. (2015), and Griffin et al. (2018). In clouds with less available moisture, dendrites are not able to grow, therefore ice crystals will tend to remain as small, hexagonal plates (Bailey and Hallett 2009), which have a lower reflectivity and lower, although non-zero, K_{DP} when viewed at low elevation angles.

At temperatures warmer than -10 °C, the primary microphysical process is the aggregation of crystals. This has the effect of increasing reflectivity while reducing K_{DP}, as observed and shown in figures 5.12 and 5.13. A volume of aggregated crystals can appear as spherical particles to a radar, both when viewed from the side and from beneath, reducing K_{DP} toward 0 $^\circ\, km^{-1}$. The exception is at the largest reflectivity, at low elevation angles, a small, positive K_{DP} is still observed (figure 5.13). There are a couple of hypotheses that would explain this. Firstly, the presence of graupel: while attempts were made to remove convective cases, it is plausible that there are some cases of stratiform systems with embedded convection. This could result in graupel just above the melting layer, which when wet would exhibit high reflectivity and non-zero K_{DP} (Liu and Chandrasekar 2000; Moisseev et al. 2015), although conical graupel could also result in negative K_{DP} (Oue et al. 2015). Secondly, it is possible that wet melting snowflakes are sometimes captured at 0 °C. Melting snowflakes are known to exhibit high K_{DP} and high radar reflectivity (e.g. Zrnić et al. (1993) and Ryzhkov and Zrnić (1998a)).

These observations from the CIP probe explain changes why K_{DP} of hydrometeors when viewed from side incidence changes, and how that may relate to temperature and reflectivity. The next section considers whether the additional information supplied by reflectivity and temperature could better help in adjusting K_{DP} from high elevation angles.

5.3 Analysis of observations during Winter 2018

To explore the results of these case studies further, 26 days on which rainfall occurred at Chilbolton Observatory between 15 January 2018 and 27 March 2018 were chosen for further analysis. This period was selected as radiosonde and aircraft measurements are also available for this time frame from the PICASSO campaign. For each of these 26 days, a DiVeN disdrometer (Pickering et al. 2019) located at Chilbolton Atmospheric Observatory was used to determine if rain was falling during each RHI scan, eliminating times with no observed precipitation. Only using data when precipitation was occurring ensures more of the data is from mature clouds, rather than clouds early in their development life cycle. Use of the Radar Convective Parameter (RCP, Bechini et al. (2013)) further limited data to periods of stratiform precipitation from well developed clouds, increases the likelihood of horizontal homogeneity such that the hydrometeors the radar observes at a distance should be the same as those observed directly overhead at the same height. RCP is defined by Bechini et al. (2013) as

$$\mathrm{RCP}(dB) = \frac{\int_{h(0\,^\circ\mathrm{C})}^{h(-15\,^\circ\mathrm{C})} \frac{\mathrm{mean}(Z_{lin})}{\mathrm{median}(Z_{lin})}\, dh}{h(-15\,^\circ\mathrm{C}) - h(0\,^\circ\mathrm{C})}, \tag{5.2}$$

where Z_{lin} is reflectivity in linear units (mm^6m^{-3}), and $h(-15\,^\circ\mathrm{C})$ is the height in metres of $-15\,^\circ\mathrm{C}$ above ground. Work by Bechini et al. (2013) shows a dramatic difference between convective and stratiform precipitation when studying the correlation between reflectivity and K_{DP}, with a marked change around RCP = 4 dB. The correlation is around 0.8 for RCP $<$ 4 dB compared to below 0.3; as such stratiform precipitation is defined as when RCP $<$ 4 dB.

From the remaining RHI scans, values of K_{DP}, horizontal reflectivity, radar elevation angle, and temperature were extracted, and then binned by both temperature (-25 °C to +5 °C in 5 °C intervals) and reflectivity (10 dB bins, starting from 0 - 10 dBZ, up to 40-50 dBZ, plus one open-ended bin for dBZ $<$ 0).

Figure 5.9 shows, for -20 °C, plots of K_{DP} against elevation angle for each reflectivity

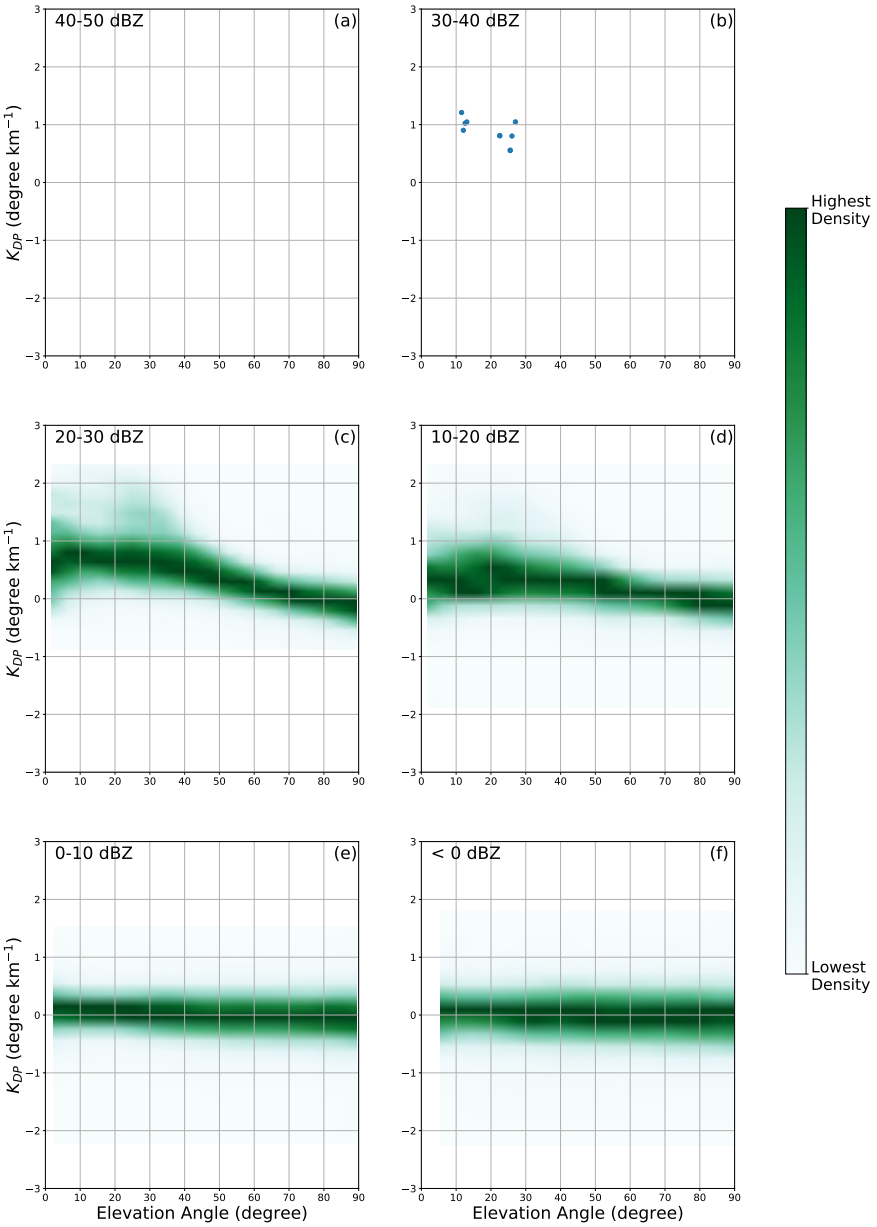

Figure 5.9: Heatmaps of K_{DP} against elevation angle at -20 °C for radar RHI scans from 26 days, normalised by elevation angle, with data split by reflectivity factor from horizontal polarization between (a) 40 and 50 dBZ, (b) 30 and 40 dBZ, (c) 20 and 30 dBZ, (d) 10 and 20 dBZ, (e) 0 and 10 dBZ, and (f) below 0 dBZ. Where more than 50 data points are present, the plots are density shaded, with the shading going from the lowest density for a given elevation angle (white) to the greatest density (dark green).

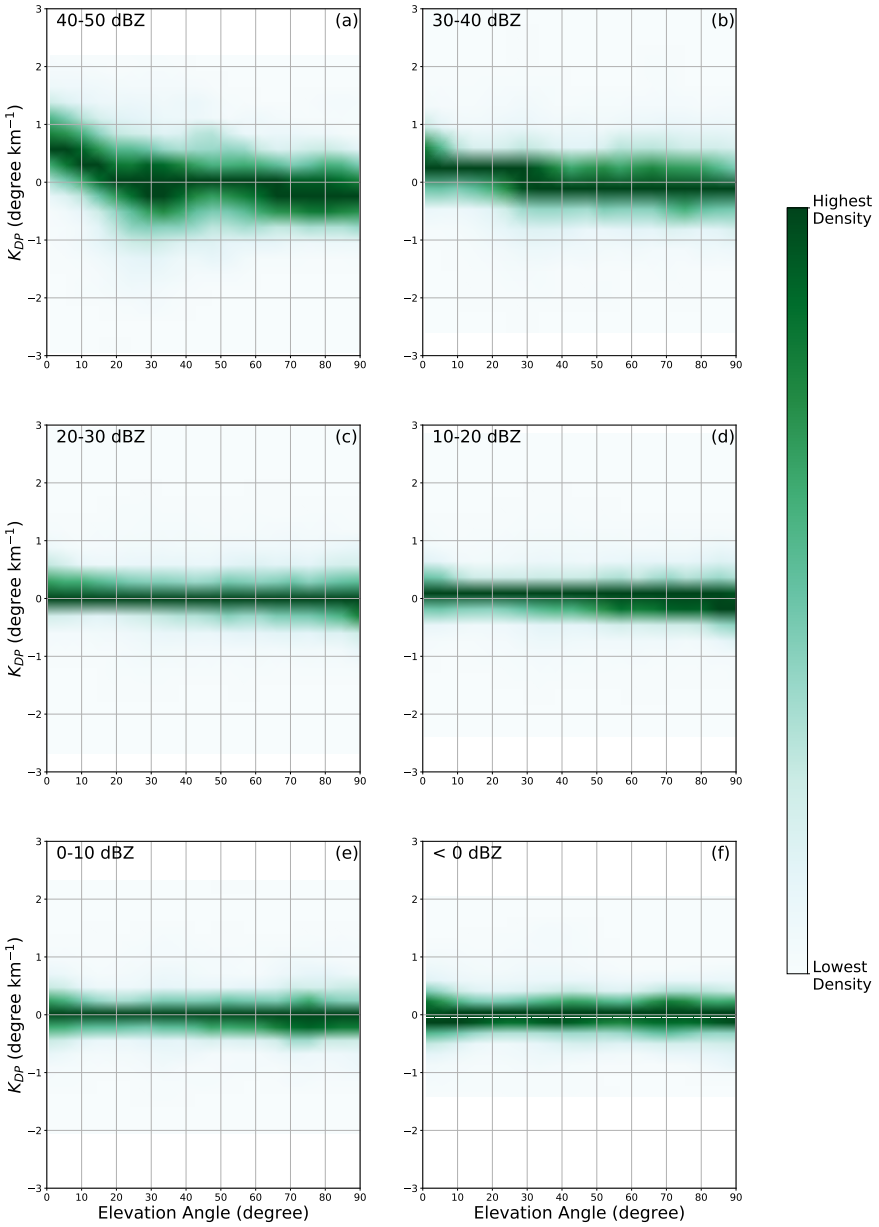

Figure 5.10: Same as Fig. 5.9, for 0 °C.

bin, shaded by density where there are more than 50 data points. A significant change in K_{DP} with respect to elevation angle is observed for more intense values of reflectivity (i.e. dBZ $>$ 20; figure 5.9c), however for lower reflectivity most K_{DP} values lie close to 0 $^\circ km^{-1}$ (figures 5.9e,f). When looking at warmer temperatures, for example 0 °C (figure 5.10), with the exception of a small change (up to around 0.5 $^\circ km^{-1}$) at low elevation angles in high reflectivity areas (30+ dBZ; figures 5.10a,b), K_{DP} changes very little with respect to radar elevation angle. However, although apparently small, the change observed at 0 °C may still be of importance, as such large reflectivity values are common just above the melting layer. These results from a larger set of measurements agree with what was observed in the few case studies.

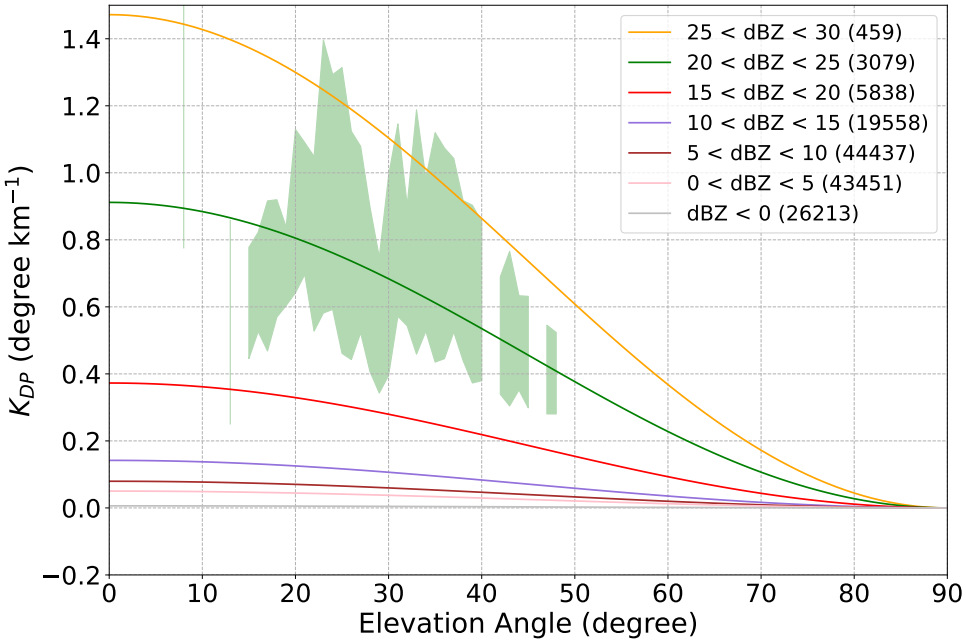

Figure 5.11: Lines showing K_{DP} against elevation angle at -20°C, fitting data from 26 days of radar RHI observations. Each line represents one 5-dBZ bin. The shading around the 20 - 25 dBZ line indicates the interquartile range for the K_{DP} measurements at that elevation angle for angles where there are more than 40 K_{DP} estimations.

To compare these six density plots at each temperature more clearly, lines of the form $K_{DP}(\theta) = a(1 + cos(2\theta))$ (from Schneebeli et al. (2013)) were fitted to each plot, where a is a constant determined to best fit the data, which from Equation 9 in Schneebeli et al. (2013) equals $K_{DP}(\theta = 0)/2$, and θ is the radar elevation angle. a is calculated such that the sum of the squared residuals between the data and the fit curve is minimised. For this comparison, data were split further by reflectivity, from 10 dBZ bins down to 5 dBZ. This gives 12 lines for each temperature (one per reflectivity bin), so

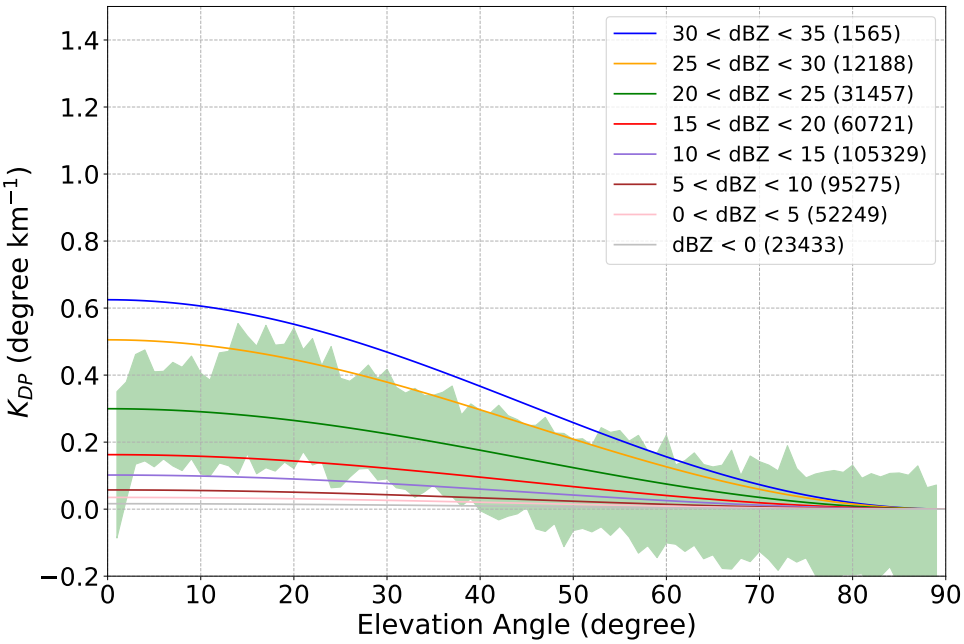

Figure 5.12: Same as Fig. 5.11, for -10 °C.

that the role of reflectivity may be more easily compared. Figure 5.11 shows these 12 bins for -20 °C, highlighting the angular dependence of K_{DP} for reflectivity greater than 20 dBZ, a smaller change in K_{DP} for the reflectivity bins covering the 10 - 20 dBZ range, and below 10 dBZ almost no change in K_{DP} with elevation angle. Figure 5.12 shows the same for -10 °C, and figure 5.13 for 0 °C. Comparison of the three temperature regimes shows that as temperature increases, the reflectivity at which the angular shift matters increases. However, at 0 °C (Figure 5.13), although the change in K_{DP} ($\sim 0.3\,^{\circ}\,km^{-1}$) is only for high reflectivity (greater than 30 dBZ), it is common for such high reflectivity to be observed just above the melting layer. Therefore, the angular change in K_{DP} at 0 °C should not be ignored.

Figure 5.14 shows the angular shift at different temperatures for the 20 - 25 dBZ reflectivity bin. This shows the importance of temperature on the strength of the variation of K_{DP} with elevation angle, with a larger change in K_{DP} as temperatures decrease. Therefore, when attempting to adjust K_{DP} at a given elevation angle to an elevation angle of 0°, temperature and reflectivity need to be taken into consideration in addition to the elevation angle. For example, if K_{DP} was measured to be $0.05\,^{\circ}\,km^{-1}$ at an elevation angle of 80°, then by following the equations in Schneebeli et al. (2013) and Lu et al. (2015), K_{DP} corrected to an elevation angle of 0° would be $1.66\,^{\circ}\,km^{-1}$, however if that measurement was taken where the temperature was around -10 °C, then

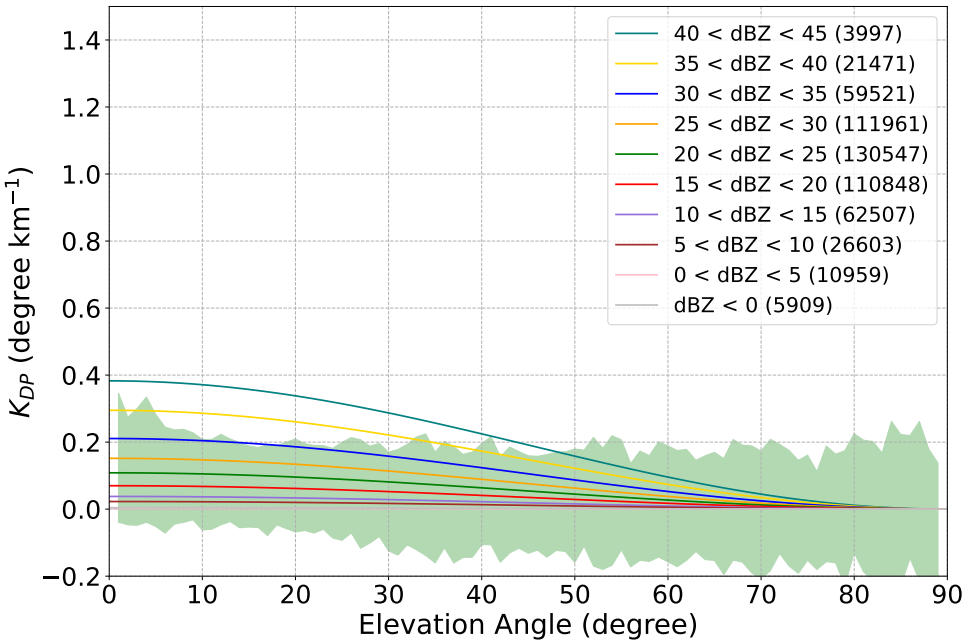

Figure 5.13: Same as Fig. 5.11, for 0 °C.

figure 5.12 would suggest that 1.66 $^\circ\, km^{-1}$ might be too high. The reflectivity measured at that point could also help determine what a more suitable value for K_{DP} might be. A reason for the importance of accounting for reflectivity is that two factors affect the shape of an ice crystal - temperature and vapor supersaturation (Bailey and Hallett 2009). For a given temperature, an increase in vapor supersaturation results in larger observed crystals (see Figure 11 in Bailey and Hallett (2009)), which in turn result in higher radar reflectivity. However, due to the large uncertainty in K_{DP} estimation (as discussed through Chapter 4), one would need to be careful to ensure efforts in adjusting K_{DP} are not dominated by temperature and reflectivity.

5.3.1 Considering noise

Following the discussion in Chapter 4, it is worth considering the noise in these K_{DP} measurements, especially as most of the estimated K_{DP} values are small. Figures 5.2, 5.3 and 5.4 include plots of the standard deviation of K_{DP} as calculated by equation 5.1, and these values from range gates above the melting layer (as determined by use of the hydrometeor classification algorithm presented in Thompson et al. (2014)) are represented in the histogram in figure 5.15. The majority of these standard deviations are below 0.2 $^\circ\, km^{-1}$, which when compared with figures 5.9 and 5.10 is within the

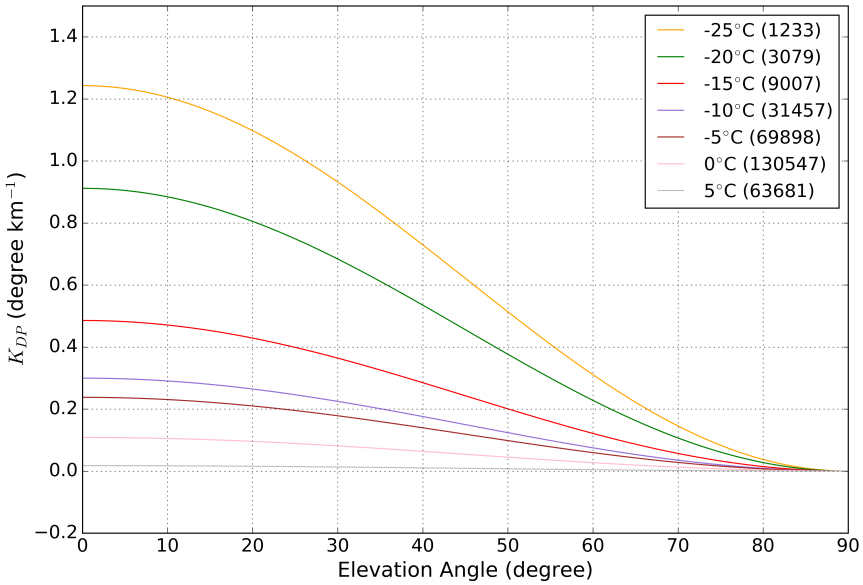

Figure 5.14: Lines showing K_{DP} against elevation angle where reflectivity is between 20 and 25 dBZ, fitting data from 26 days of radar RHI observations. Each line represents data at a specific temperature. The legend states in brackets how many data points are represented by each line.

region of highest density of K_{DP} measurements at all angles and reflectivities.

However, when considering how this might affect use of equation 5.1 to adjust K_{DP} from high elevation angle to 0° elevation, a difference of 0.2 $^\circ\, km^{-1}$ to the K_{DP} estimation is significant, as can be seen through use of figures 5.11-5.13. For figure 5.11, 0.2 $^\circ\, km^{-1}$ covers the range of the best fit lines above 70° elevation, with an error of 0.2 $^\circ\, km^{-1}$ being multiplied by 8.55 through the use of equation 5.1 (see table 5.1). At warmer temperatures (for example -10°C as shown in figure 5.12), 0.2 $^\circ\, km^{-1}$ covers the spread of the best fit lines at an elevation angle of 55° - at warmer temperatures an error of 0.2 $^\circ\, km^{-1}$ covers the range of the best fit lines at lower elevations, although as elevation angle decreases so does the multiplication factor of adjusting K_{DP} to 0° elevation. This further suggests that use of K_{DP} and elevation angle alone will not be sufficient when adjusting K_{DP} values for elevation angle; however, decreasing the standard deviation of K_{DP} can increase the elevation angle where adjusting K_{DP} through the use of equation 5.1 can be useful.

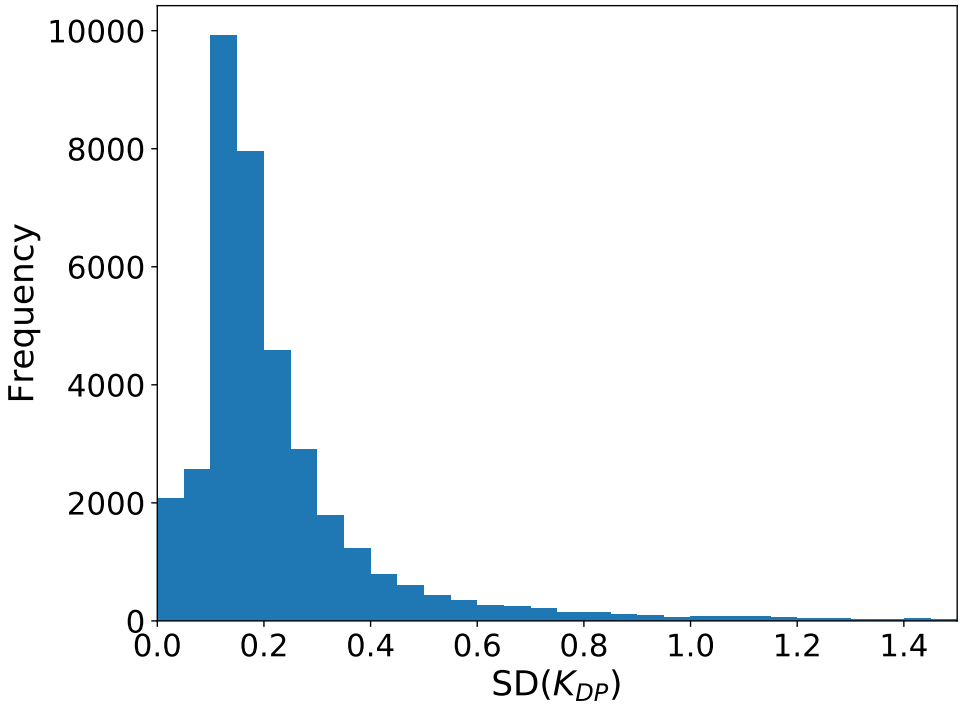

Figure 5.15: Histogram of standard deviation of K_{DP} as calculated by Equation 2.16 for data points in the three case studies shown (Figures 5.2,5.3,5.4) classified as plates, dendrites, ice crystals or aggregates by the Thompson et al. (2014) hydrometeor classification algorithm.

5.4 Implications

To further explore the role of aggregation in the elevation dependence of K_{DP}, the hydrometeor classification algorithm (HCA) from Thompson et al. (2014) was applied to the three case studies shown in figures 5.2, 5.3, & 5.4, the results of which are shown in figures 5.16, 5.17, & 5.18. This HCA is designed specifically for stratiform precipitation, and distinguishes between different ice habit types above the melting layer. The algorithm uses reflectivity, differential reflectivity and co-polar correlation coefficient to firstly determine the location of the melting layer, with the areas above and below the melting layer then treated separately. The areas above the melting layer are classified as aggregates, ice crystals, dendrites, or plates, using specific differential phase in addition to the polarimetric observations used in the melting layer detection. Below the melting layer, temperature is used along with horizontal reflectivity to classify between rain and freezing rain.

In this implementation of the HCA, reflectivity data is used without attenuation correc-

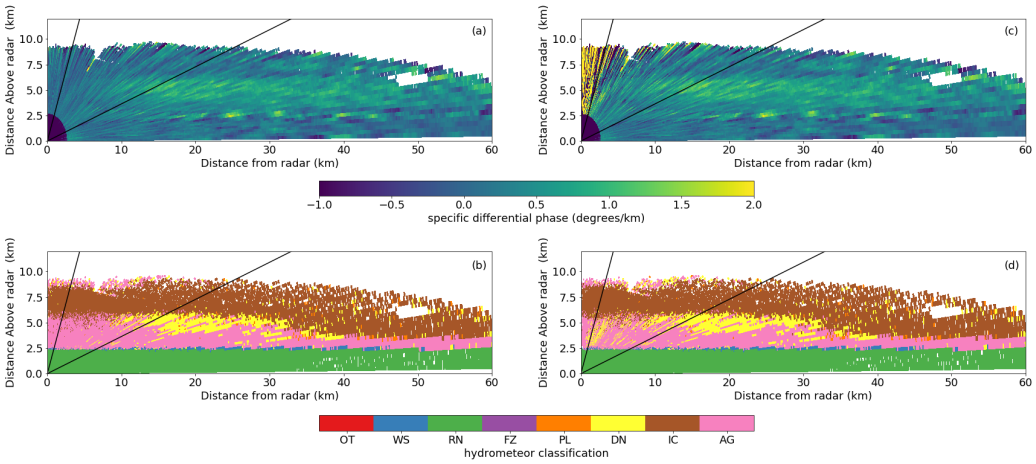

Figure 5.16: K_{DP} and hydrometeor classification algorithm based on Thompson et al. (2014) from a radar RHI scan at 11:36:54 UTC 17 May 2017 (figure 5.2). (a) K_{DP} as measured by the radar. (b) Hydrometeor classification algorithm using measured K_{DP}. (c) K_{DP} corrected to 0° following Eq. 9 in Schneebeli et al. (2013) when elevation angle is greater than 20°. (d) Hydrometeor classification algorithm using adjusted K_{DP}. The black lines on each plot show 20° and 70° elevation angle. The abbreviations in the legend for the hydrometeor classification expand as follows: OT - other, WS - wet snow, RN - rain, FZ - freezing rain, PL - plates, DN - dendrites, IC - ice crystals, AG - aggregates.

tion. Although use of corrected Z_{dr} would be ideal, correcting Z_{dr} is non-trivial, with most methods correcting Z_{dr} based on attenuation in rainfall. Furthermore, Φ_{DP} is often used to constrain attenuation correction algorithms (Jameson 1992; Testud et al. 2000; Lim and Chandrasekar 2016). As the focus of this chapter is on the ice region of clouds, with only a short path through liquid regions, such techniques would not be suitable. While this may cause some small error, in the ice region K_{DP} has the greatest weighting of the three variables used in the HCA, and as such the accuracy of K_{DP} is more important.

The output from the HCA for the 17 May 2017 case (figure 5.16) suggests that aggregates (AG) are present at higher altitudes (colder temperatures) at higher elevation angles compared to lower elevation angles (almost 6 km above ground, about -15 °C, compared to 4 km, about -5 °C). Dendrites at -10 °C to -15 °C are present at lower elevation angles (up to around 20°), but at higher elevation angles are classified instead as aggregates. A similar pattern is seen in the 12 July 2017 case (figure 5.18) with the classification of dendrites between 3 and 7 km above ground, although the presence of stronger estimated K_{DP} at elevation angles just above 20° results in the transition to

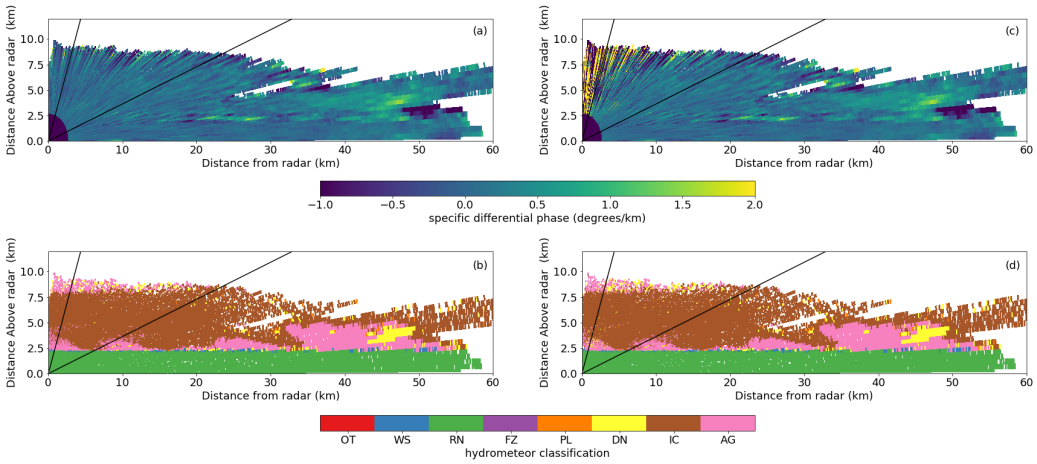

Figure 5.17: Same as figure 5.16, but for data from 17:08:12 UTC 5 June 2017, as in figure 5.3.

from dendrites to aggregates at higher altitudes starting at a higher elevation angle. If this change in classification is due to a change in K_{DP} caused by the change in radar viewing angle, then by changing K_{DP} at high elevation angles to match that at a lower elevation angle, it should be expected that the classification of aggregates at high elevation angles should change. An alternative method could be to change the weighting for K_{DP} to be a function of elevation angle and temperature, however this could lead to the classification being mostly dependent on reflectivity and temperature, which could result in unrealistic crystal classifications (Thompson et al. 2014). This hypothesis is tested by changing K_{DP} for all elevation angles greater than 20° to what K_{DP} should be at 0° elevation angle, according to equation 9 in Schneebeli et al. (2013). Although Z_{dr} also changes with elevation angle, that correction has not been applied here, so that the importance of adjusting K_{DP} can be identified, and in this hydrometeor classification algorithm K_{DP} has a greater weight in deciding the probability of ice hydrometeors than Z_{dr} does. The result of this is shown in figure 5.16(c), and the hydrometeor classification using the changed K_{DP} in figure 5.16(d).

Through changing K_{DP} measured at high elevation angles, the output of the hydrometeor classification algorithm changes to dendrites where previously there were aggregates. This suggests that at high elevation angles, these observed changes in K_{DP}, along with the general uncertainty in K_{DP} estimation, can result in misidentification of hydrometeors as aggregates. However, for elevation angles greater than 70°, the correction to K_{DP} appears to be inadequate, providing an apparently large over-correction, as noted by Schneebeli et al. (2013) and Lu et al. (2015).

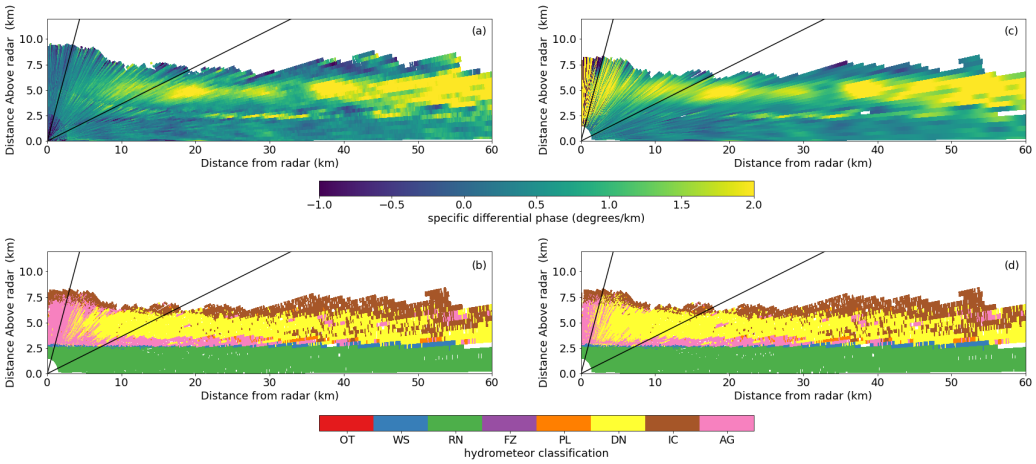

Figure 5.18: Same as figure 5.16, but for data from 01:35:54 UTC 12 July 2017, as in figure 5.4.

Figure 5.17 shows an example with lower estimated K_{DP}, with the classification of ice in the cloud dominated by ice crystals, rather than dendrites. After adjusting K_{DP} due to elevation angle, very little change is seen in the output from the hydrometeor classification algorithm, suggesting the low K_{DP} values do not have much influence on the HCA output. As in the other two examples, this simple adjustment provides very large estimations of K_{DP} above 70°. As the change in K_{DP} with elevation angle has been shown in this chapter to be influenced by reflectivity and temperature, using reflectivity and temperature data could help improve corrections to K_{DP}.

5.5 Summary

The observations in this chapter confirm that measured specific differential phase is strongly affected by the viewing geometry of the radar, confirming the theoretical $cos(2\theta)$ dependence as described in Schneebeli et al. (2013) and Lu et al. (2015), with values of K_{DP} tending toward 0 $^\circ\, km^{-1}$ as the elevation angle increases to 90°.

However, as both of those studies state, and as these observations show, use of this equation is inadequate when adjusting K_{DP} to side incidence from an elevation angle greater than 70°. This is due to K_{DP} being close to zero, and so a small change in the measured K_{DP} at high elevation angle (e.g. due to noisy estimates as discussed in Section 4.2.4, or excessive smoothing in calculation) result in large changes to the estimated K_{DP} at 0° elevation. This is shown to result in misidentification from hy-

drometeor classification algorithms.

The observations analysed in this chapter suggest that adjustments of K_{DP} from high elevation angles to 0° elevation angle could be improved by including reflectivity from horizontal polarisation and temperature observations within the correction. As temperature decreases above the melting layer, or as reflectivity increases, K_{DP} at low elevation angles tends to increase. Using this knowledge can provide a guideline for more accurate K_{DP} adjustments.

The proposed underlying physical mechanism for this phenomenon is the vapour growth and aggregation of pristine plates and columns. At cold temperatures, the presence of small plate and column crystals result in positive K_{DP} values when viewed from the side, however when viewed from beneath K_{DP} would tend to zero. Slightly larger crystals, with greater reflectivity, will appear wider (plates) and longer (columns), and so would have a greater K_{DP}. As temperature increases, these crystals start to aggregate, forming hydrometeors irregular in shape but appearing more spherical to the radar, thus leading to lower K_{DP}, until the hydrometeors melt and become quasi-spherical raindrops, resulting in $K_{DP} \sim 0\ ^\circ\, km^{-1}$. While in-situ observations from one day support this idea, additional observations and modelling are needed to explore this hypothesis.

Chapter 6

Comparison between radar forward operator output and radar observations of K_{DP}

While there are many uses for polarimetric weather radar observations, for example hydrometeor classification (for example Liu and Chandrasekar (2000); Thompson et al. (2014)), quantitative precipitation estimation (Tabary et al. 2011; Vulpiani et al. 2012), and liquid and ice water content estimation (Ryzhkov et al. 1998; Hogan et al. 2005), one area which is a relatively new area of research is the utilisation of radar data in numerical weather prediction (NWP) models (Ryzhkov et al. 2020). Radars can provide data at a high temporal resolution over a large coverage area, and can identify different hydrometeor types and processes through polarimetric data which could be used to constrain the microphysics in NWP models (Ryzhkov et al. 2020). These uncertainties are a major contributor to uncertainty in forecasts (Morrison et al. 2020) due to uncertainty in the microphysical processes and the need for a level of simplicity (Morrison et al. 2015; Fan et al. 2017).

However, radars and models do not have the same data. One aspect of this is that radar measurements are often at a much higher spatial resolution than model grid spacing (for example 300 m range gates between UK Met Office radar measurements, and 1.5 km grid spacing in the Met Office high resolution model run (Hawkness-Smith and Simonin 2021)). Not only do radar and model data occupy different spatial domains, they also have different variables representing different physical properties. State variables from NWP models are mass mixing ratio and number concentration for each hydrometeor, which are proportional to the 3^{rd} and 0^{th} moment of the size distribution (Ryzhkov et al.

2020). Radar variables are measurements of how hydrometeors scatter electromagnetic radiation (Ryzhkov et al. 2020), and are determined by higher moments of the Drop Size Distribution, i.e. radar reflectivity is approximately the 6^{th} moment (Zhang et al. 2019). This means that data stored in polarimetric radar measurements are influenced more by larger hydrometeors, which are fewer in number than the smaller hydrometeors which have important effects on microphysical processes (Zhang et al. 2019). Some studies have attempted combining dual-polarisation parameters in an attempt to overcome this issue when using radar data to estimate the Drop Size Distribution (Huang et al. 2019; Bringi et al. 2020).

A key aspect in bridging the gap between radar meteorology and numerical weather prediction is the development of radar forward operators. Forward operators take the state variables from the cloud microphysics scheme in NWP models, and estimate radar variables through the use of scattering calculations, based on the size distributions predicted by the microphysics scheme and assumptions on the aspect ratio and canting angles of the hydrometeors. This is the start of the data assimilation process, which has the potential to be one of the main uses for polarimetric radar observations, particularly in convective scale NWP (Wang et al. 2013; Zhang et al. 2019). Forward operators are also used to aid with model evaluation, with a number of studies (for example Bodas-Salcedo et al. (2008); Nam and Quaas (2012)) using forward operators to convert model data to satellite observations. While satellites are more often used for such evaluations, such work can also be carried out using ground-based radar data (for example Bouniol et al. (2010)).

The work presented in this chapter aims to study how well, if at all, regions of elevated KDP can be simulated from a radar forward operator, with elevated K_{DP} being an indicator of increased rainfall rate (Bechini et al. 2013) or associated with radar signatures of microphysical processes (for example secondary ice production (Sinclair et al. 2016) and dendritic growth (Kennedy and Rutledge 2011)). One case study - a frontal weather system across the UK on the 24^{th} January 2018 - is studied, during which a number of elevated K_{DP} regions can be observed in the radar data (figure 6.1). The forward operator is initiated with data from high-resolution WRF model output, and is presented using multiple microphysics schemes, to ensure that observations of the output from the forward operator are related to the forward operator, and are not dependent on the microphysical scheme chosen.

This chapter is presented as follows. Firstly, the output from the WRF model runs is checked against surface observations at Chilbolton Observatory to check its accuracy.

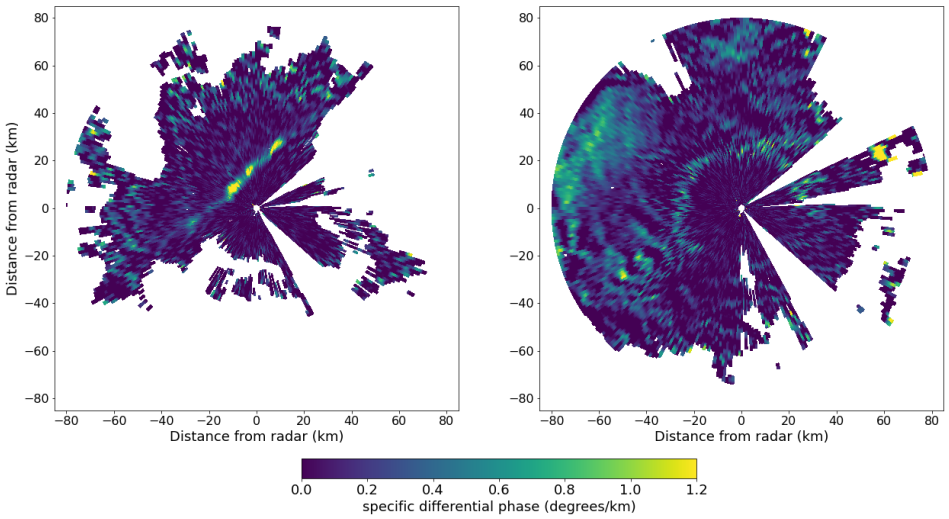

Figure 6.1: K_{DP} on 24 January 2018 at 10:54:18 UTC (left) and 13:41:59 UTC (right), at 2° elevation angle.

Next, the estimates from CR-SIM are compared to each other to look for differences between the microphysics schemes. Finally, the CR-SIM output is compared to radar observations with a focus on K_{DP}, using PPI scans from NXPol-1 as these scans show a wide coverage area, are routinely collected by operational radar networks, and avoid the problems of high elevation angles as discussed in Chapter 5.

6.1 Comparison between WRF model output and Chilbolton surface observations

The case study chosen is a cold front passing through the United Kingdom on the 24$^{\text{th}}$ January 2018. On this day, a low pressure system moved north-east across the western Northern Ireland coast and across north-western Scotland into the North Sea, with a long trailing cold front bringing rain to most of the UK throughout the morning, with rain continuing to fall through the afternoon in southern and south-eastern England (figure 6.2).

Output of 2m temperature, precipitation, and sea level pressure from each WRF run is compared against surface measurements from Chilbolton Observatory (Figures 6.3, 6.4 & 6.5). These show that while the model captures the general trend throughout the

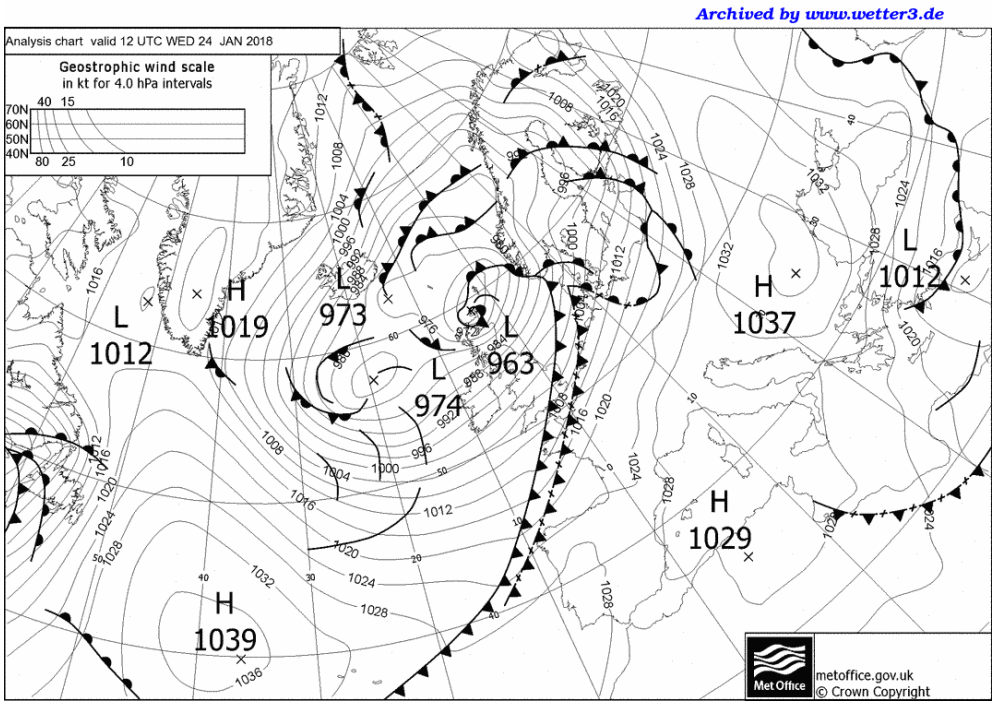

Figure 6.2: Synoptic chart for 24$^{\text{th}}$ January 2018 12:00 UTC.

day, the timing of the main cold front passing Chilbolton Observatory is wrong by ∼30 minutes, independent of the microphysics scheme used. This indicates the timing of the front in the model may be a function of the initial and lateral boundary conditions, rather than the microphysics scheme.

The WRF models in this case study also fail to capture the intensity of the rainfall (Figure 6.5). They capture the presence of rain both before and after the front passes through; however, the total precipitation values are less than 50% of that measured by the surface rain gauge. The choice of microphysics scheme leads to differences in the total precipitation, which mostly comes in the hour or two after the front passes through. It would be expected that this reduction in rainfall would result in slightly lower values of horizontal reflectivity and specific differential phase from the forward operator compared to that measured by the radar; for example, taking the peak station rainfall rate as 22 mm/hr, and the peak model rainfall rate as 12 mm/hr (from figure 6.5), that would convert to an expected radar reflectivity near the surface of 45 dBZ and 41 dBZ respectively using the Marshall-Palmer relationship of $Z = 220R^{1.6}$ (Marshall and Palmer 1948), and expected K_{DP} values of 1.39 $^\circ km^{-1}$ and 0.65 $^\circ km^{-1}$ using $R = 16.9|K_{DP}|^{0.801}$ from Ryzhkov et al. (2014) (Table 6.1). These numbers are not meant as predictions of what should be seen based on the rainfall rate, but rather are

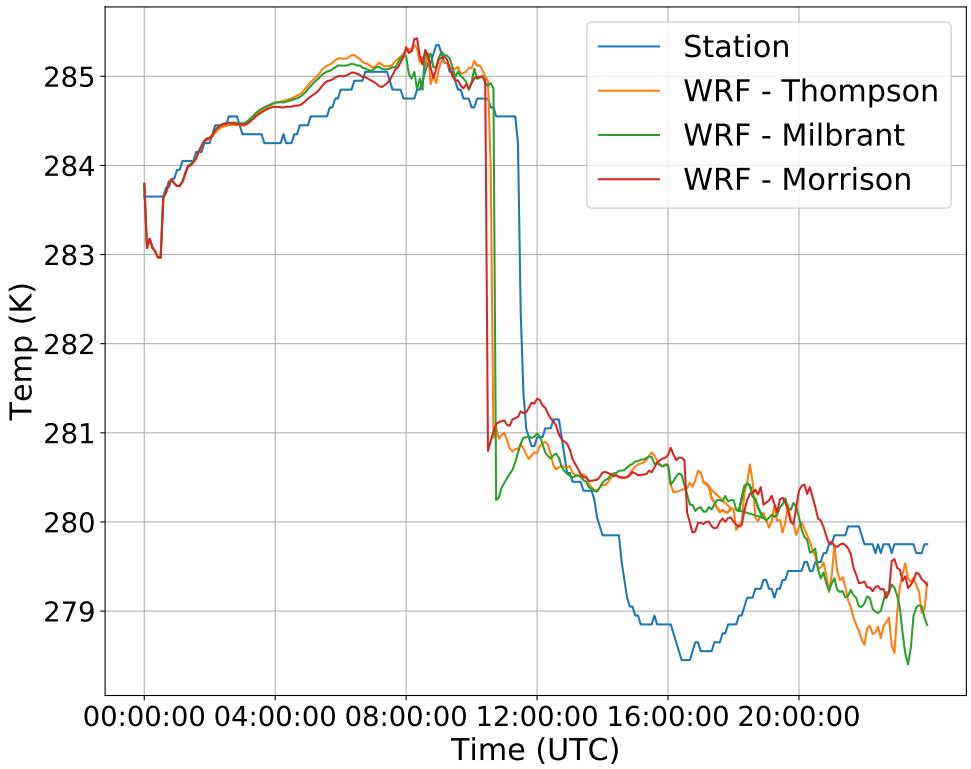

Figure 6.3: Temperature at Chilbolton Observatory, as predicted by each WRF run and observed (blue line).

meant to suggest how much of a difference might be expected between the radar and forward operator outputs.

Rainfall Rate	Expected Reflectivity	Expected K_{DP}
22 mm/hr (station)	45 dBZ	1.39 $^\circ\, km^{-1}$
12 mm/hr (model)	41 dBZ	0.65 $^\circ\, km^{-1}$

Table 6.1: Expected reflectivity and specific differential phase based on peak rainfall rates observed at Chilbolton Observatory and predicted by WRF.

While this single-point analysis is not sufficient as a full study of model analysis, that is not the intention of this work. Rather, this single-site comparison is intended to provide a sanity check that the model computes a reasonable prediction of the observed weather conditions, which these single-point comparisons confirm, with all three microphysical schemes producing similar results that resemble the features of the observations.

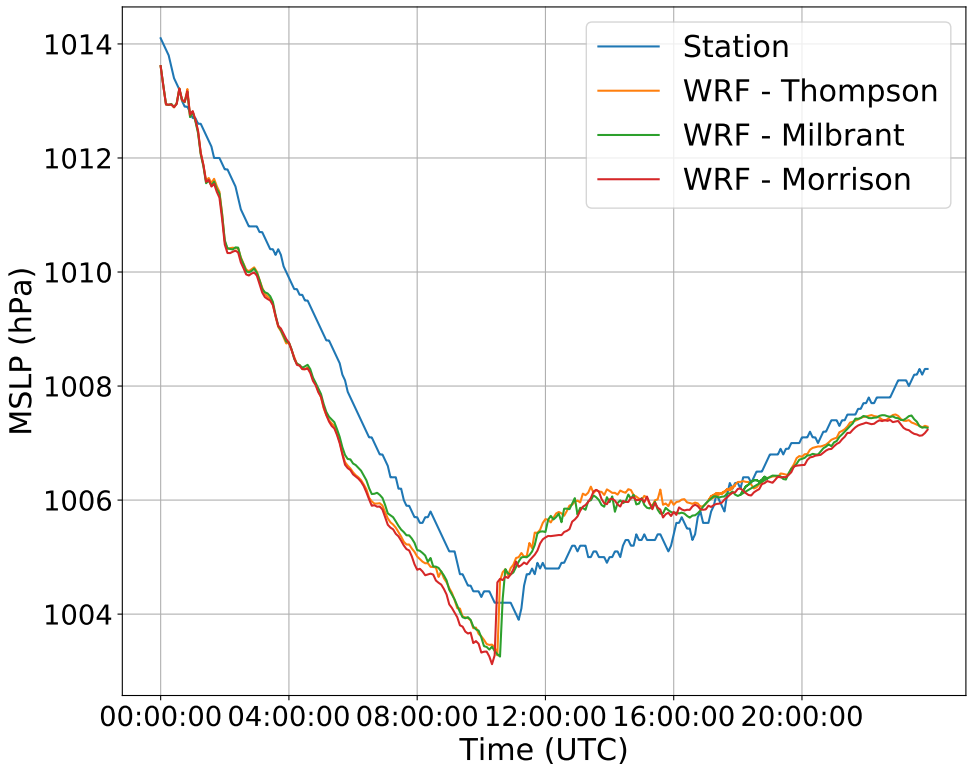

Figure 6.4: As Fig.6.3, for mean sea level pressure.

6.2 Comparison of CR-SIM output between different microphysical schemes

Figure 6.6 shows WRF output, CR-SIM output, and radar data for 24$^{\text{th}}$ January 2018 at 10:55 UTC at a 2° elevation angle, with output from the three microphysics schemes used. All three schemes produce high reflectivity along the front (>40 dBZ), with the Morrison and Thompson schemes having higher reflectivity and a thicker front than the Milbrant scheme. To understand this, the number and size concentrations for each hydrometeor predicted by each scheme would need to be studied and compared to in-situ data, which is beyond the scope of this study. The Morrison and Thompson schemes also give higher K_{DP} than the Milbrant scheme, with values exceeding 1 $^\circ\, km^{-1}$ throughout much of the front for Morrison and Thompson, compared to only small regions of high values in the Milbrant scheme, with most values in the front between 0.4 and 0.8 $^\circ\, km^{-1}$.

Ahead of the front, the model simulations resolve lines of precipitation ahead of the front, which can be seen in the precipitation plots and the reflectivity plots (regions

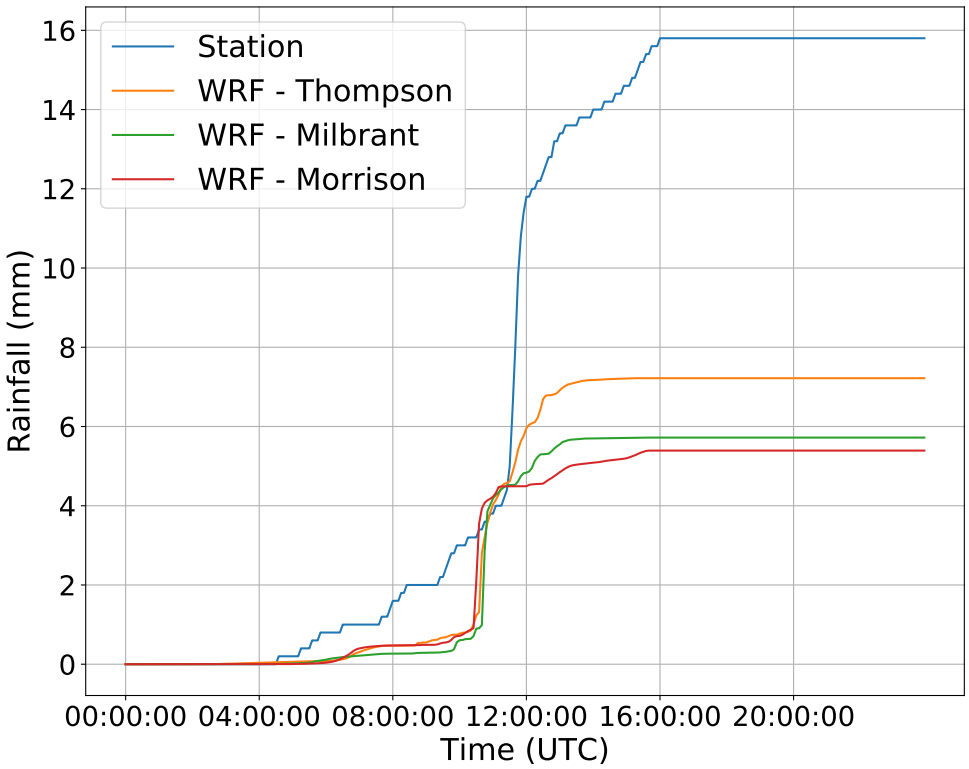

Figure 6.5: As Fig.6.3, for rainfall.

around 20-30 dBZ), and to a lesser extent the K_{DP} plot for the Thompson and Morrison schemes. However, despite the higher reflectivity and K_{DP} produced by the model than the radar, the amount of rainfall observed by the weather station is not replicated in any of the WRF simulations, missing around 3 mm of rain before the arrival of the front.

The model simulations diverge slightly behind the front (Figure 6.7). The Milbrant and Morrison schemes show cloud breakup behind the front, with patchy areas of higher reflectivity (20+ dBZ) and larger areas of low reflectivity (<0 dBZ), while the Thompson scheme has more area of the larger reflectivity. However, all of the schemes have very small K_{DP} after the front has passed, with some small patches of low K_{DP} ($< 0.1\ ^\circ km^{-1}$) in areas of where higher reflectivity is simulated.

While the two times shown in figures 6.6 & 6.7 do not capture the entire evolution of the weather system as it passes over the radar, they do show the model produces a reasonable simulation of the weather on that day, while highlighting similarities and differences between the schemes on either side of the main front.

Figure 6.6: Radar measurements plus output from WRF and CR-SIM at 10:55 UTC 24$^{\text{th}}$ January 2018 at a 2° elevation angle. Top row shows rainfall intensity predicted by each microphysical scheme (Thompson, Milbrant and Morrison, in that order). Second row shows the estimated reflectivity from CR-SIM, along with the radar measurements in the far right column. The bottom row shows the estimated K_{DP}, again from CR-SIM and from the radar.

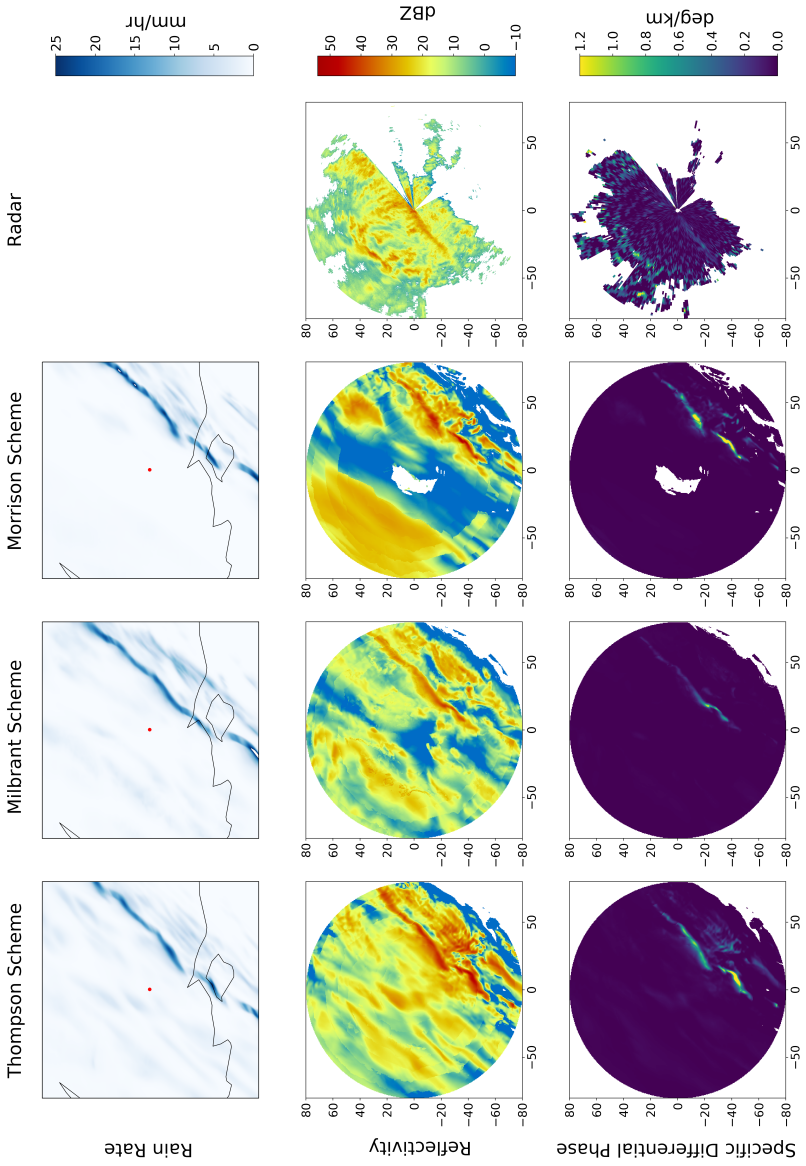

Figure 6.7: Same as fig.6.6, at 11:30 UTC.

6.3 Comparison between CR-SIM and radar observations

While comparing the CR-SIM output between the different microphysical schemes show there are some differences, they all appear as plausible and realistic when compared to the radar observations. As the front passes Chilbolton Observatory, CR-SIM from the Milbrant scheme replicates the radar observations most closely, with closer values of reflectivity and K_{DP}, and similar thickness of the front as judged by the width of high reflectivity, whereas the Morrison and Thompson schemes show a slightly larger values and a thicker front; this pattern is replicated through other elevation angles. This is surprising given the lower rainfall in the models compared to the observations: lower values of polarimetric radar variables would be expected with lower rainfall.

However, in the ice region of the clouds, there are further discrepancies in the CR-SIM output, particularly in the estimated K_{DP}. Figure 6.8 shows an example of missing a number of large K_{DP} features, and while data from only one time is shown, these results hold throughout all output from this event. Firstly, a ring of higher K_{DP} at a range between 20km and 40km can be seen in the radar observation, which is not observed in any of the CR-SIM simulations. This ring is located in the melting layer. As changes in radar measurements around the melting layer are a key signature in radar measurements, it should be simulated in a radar forward operator.

Another region of increased K_{DP} is observed 60km to 80km west of the radar, in a region where the temperature is around -8 °C, deduced from model simulations from the Met Office (section 3.2). This is completely missed in the K_{DP} from CR-SIM in the Morrison scheme, which is the only one to still have reflectivity values close to the radar observations at this time. This region has the signs of being an area of secondary ice production, with large K_{DP} and an increase in Z_{DR} in the region as shown in figure 6.9 (Sinclair et al. 2016; Field et al. 2017). Secondary ice production is seen as an important mechanism to explain the difference between the expected ice particle concentrations from primary ice nucleation, and the concentrations observed through airborne observations. Correctly predicting ice concentrations, which play an important role in cloud development and evolution (Hallett and Mossop 1974), is an important challenge to a successful microphysics scheme (Field et al. 2017).

Possibly the main reason why this potential area of secondary ice production is missed by the model and the forward operator is due to the generalisation of ice. Most microphysics schemes categorise ice as hail, graupel or ice, which is a very broad category. As shown by Bailey and Hallett (2009), there are a range of shapes, sizes, and categories

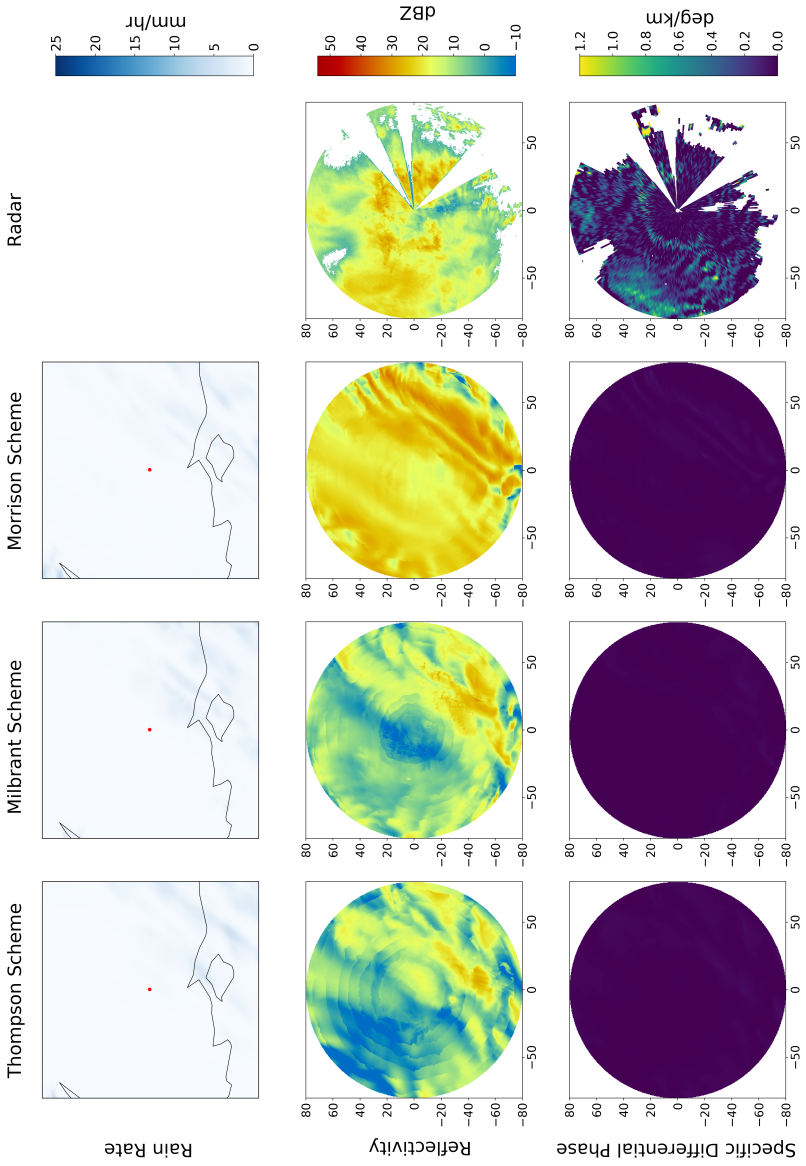

Figure 6.8: Same as fig.6.6, at 13:40 UTC.

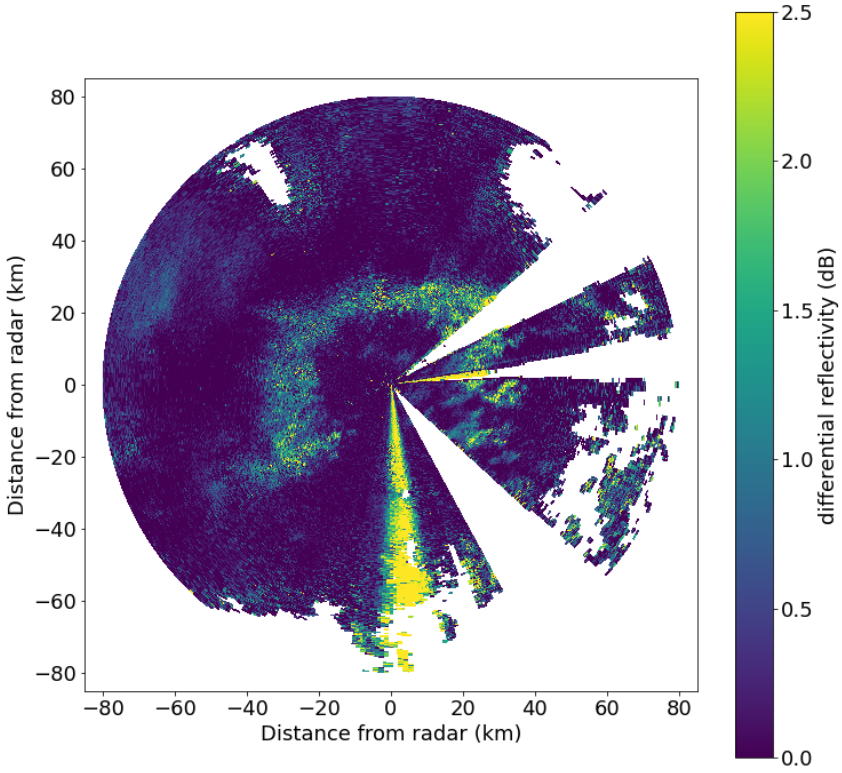

Figure 6.9: PPI of Z_{DR} at 13:41 UTC using a 2° elevation angle.

of ice crystal, which grow depending on the temperature and supersaturation of the environment. Including all of these into one category may speed up the computation of the microphysics scheme; however, key details in the cloud may be missed when compared to radar observations.

6.4 Future Work

To increase the accuracy of K_{DP} estimations from radar forward operators above the melting layer, more ice habit types need to be represented, which could result in better replication of polarimetric radar signatures. There are potentially two options for this: either take the temperature and humidity information from the model and make assumptions on the dominant habit type based on the work by Bailey and Hallett

(2009), or incorporate more ice habit types in microphysical schemes, which increases the complexity and computation time of the scheme but provides more information for the forward operator to work with.

There is one microphysics scheme in the WRF model that has more detail in the ice category, which is the Hebrew University Cloud Model (Khain et al. 2004). This is a bin microphysics cloud model which has separate categories for plate-, columnar-, and branch-like ice crystals, as well as aggregates. While CR-SIM does not have this scheme incorporated into the code, the program is written to be expandable to include further microphysics schemes.

Adding these different ice crystal types into the forward operator highlights an issue with the current assumptions in CR-SIM. The scattering properties for all ice hydrometeors (ice crystals, snow, graupel and hail) are only computed for a temperature of -30 °C. As shown by Bailey and Hallett (2009), ice crystals at -30 °C grow in a different way to those at -5 °C, and therefore the scattering properties of those crystals will be different. Likewise, an increase in ice supersaturation results in different size or shape ice crystals (larger supersaturation typically results in bigger crystals), and therefore different scattering properties. While the T-matrix code used to calculate the scattering properties does not require temperature or supersaturation, it does require axis ratio and equivalent volume diameter, which are size and shape dependent, therefore incorporating additional environmental information could result in more accurate scattering properties.

Another assumption of the CR-SIM operator that hinders accurate emulation of radar measurements is that all hydrometeors are either pure liquid or a mixture of ice and air, that is there are no melting hydrometeors. This will result in a large misrepresentation of radar measurements, particularly in mid-latitudinal weather conditions, as melting snow forms a very distinct layer in the radar data, as seen in figure 6.8 and discussed in section 6.3 (Austin and Bemis 1950; Smyth and Illingworth 1998; Sánchez-Diezma et al. 2000). A radar forward operator developed by Jung et al. (2008), and refined by Dawson et al. (2014), included a melting model, in which when snow and rain coexist some of the rain mixing ratio is combined with some of the snow mixing ratio to create a rain-snow mixture (section 3b in Jung et al. (2008)). This would help output from the operator to replicate one of the key signatures seen in radar observations - the radar bright band characteristic of the melting layer.

6.5 Summary

There are many uses for polarimetric radar observations, but utilising the data with numerical weather prediction is still a relatively new area of research (Ryzhkov et al. 2020). By estimating radar observations from model output, radar forward operators provide the means to compare model data to radar observations. However, shortcomings in radar forward operators, particularly with regards to how ice is treated mean that some radar signatures are not reproduced, for example the radar bright band, or elevated K_{DP} in areas of secondary ice production.

There are two major benefits of having a radar forward operator that can accurately reproduce polarimetric observations such as K_{DP}. Firstly, it is largely understood that one of the main sources of uncertainty in forecasts comes from inadequate microphysical parameterisations (Morrison et al. 2015; Fan et al. 2017). Polarimetric weather radars provide a lot of information that could be useful for constraining microphysical schemes, but to do so, uncertainty and inaccuracy in the measurements (as discussed in Chapters 4 & 5, for example), and then in the operators, needs to be considered and reduced where possible (Ryzhkov et al. 2020). Secondly, the data obtained by radars can be assimilated into numerical weather prediction models. It has been shown that assimilating reflectivity helps reduce spin up time in models (Sun and Crook 1997; Gao and Stensrud 2012) and can help improve precipitation forecasts (Jung et al. 2012; Snook et al. 2016); however, reflectivity alone is not enough to analyse all the variables in a multi-moment microphysics scheme, hence the need for a forward operator that can accurately reproduce polarimetric radar data from numerical model output.

Chapter 7

Synthesis

The aim of this thesis was to study some of the uncertainties associated with estimations of Specific Differential Phase (K_{DP}), using data from the NCAS mobile X-band radar (NXPol-1). K_{DP} is less sensitive to large hydrometeors than reflectivity measurements, being proportional to the number of drops of diameter D multiplied by D^a, where a is between 4.3 and 4.9 for K_{DP}, compared to 6 for reflectivity (Fabry 2015; Ryzhkov and Zrnić 2019). With the constant a being approximately 3.67 for rainfall rate, K_{DP} appears to be more favourable for quantitative precipitation estimation. Furthermore, K_{DP} is more closely related to ice water content (IWC) than reflectivity is, with a linear relationship to IWC making K_{DP} more suitable for microphysical retrievals (Vivekanandan et al. 1994; Bukovčić et al. 2018). Improved retrievals could help facilitate the use of polarimetric radar data in initialising numerical weather prediction (NWP) models (Jung et al. 2008).

However, K_{DP} is not measured directly by the radar, rather it is derived from the measurement of the total differential phase (Ψ_{DP}), which includes measurements of backscatter differential phase (δ), and noise within the phase measurements. This makes retrieving K_{DP} from radar observations challenging and prone to uncertainty and error. This thesis focused on three topics:

- How different methods of retrieving K_{DP} from Ψ_{DP} deal with noise, the presence of δ, and negative K_{DP} values, through performance against a synthetic, but known, 'true' profile, and through performance on real data.
- How the viewing geometry of targets from the radar influence estimations of K_{DP}.
- How well output from NWP models and radar forward operators can replicate K_{DP}.

These topics were studied through use of observations from the NCAS mobile X-band radar while it was stationed at Chilbolton Observatory from November 2016 through to June 2018 through the PICASSO (Parameterizing Ice Clouds using Airborne obServationS and triple-frequency dOppler radar) campaign, along with output from the Met Office UK Atmospheric High Resolution Model (Met Office 2016), the Weather Research and Forecasting (WRF) model (Skamarock et al. 2021), and observations from the Facility for Airborne Atmospheric Measurements (FAAM) aircraft.

7.1 Review of results

The results from each section are summarised below, along with any suggestions for further research.

7.1.1 Chapter 4: Comparison of different K_{DP} estimation methods.

The aim of this section was to determine the impact of K_{DP} estimation methodology on its retrieval. Seven different estimation methods, with a range of complexity in how they estimate K_{DP}, were tested against an artificial, but known, 'true' profile, and then eight methods were compared to each other when using real data (the K_{DP} estimation method provided by the Rainbow software with the radar could not be used in the artificial K_{DP} section, but was used in the real data section). Two of the methods used in the first section (Ryzhkov and Bringi) use changing averaging window sizes depending on reflectivity thresholds - each of these methods were tested with a constant reflectivity profile on either side of each threshold.

All of the methods were able to accurately reproduce the clean synthetic K_{DP} profile away from the sharp gradient, but there were various discrepancies close to the step change in K_{DP} that affected the estimated retrievals for some range either side of the gradient. While such a large, sudden change in K_{DP} would not be expected in real data, users should be aware of the small inaccuracies that are created by such a change, particularly in the Maesaka method which oscillates around the true positive value for a while after the gradient. Most of the methods were also accurate in their reproduction of the true K_{DP} profile when there were random missing data points along the ray; however, the UKMO method was strongly affected around the locations of missing data, producing large spikes of K_{DP} at those locations. The Ryzhkov method for high reflectivity was similarly affected, although to a lesser degree, and the Vulpiani

method underestimated K_{DP} due to the addition of missing data. The Bringi method uses an averaging window as part of its estimation at each point along the ray, and if any measurement within that window is missing then it does not estimate K_{DP} at that ray. This results in large gaps in the estimated profile, although when an estimation is present it is close to the 'true' profile. Interpolating the Ψ_{DP} profile before estimating K_{DP} removes these mentioned issues in all affected methods, and so may be an important step in achieving accurate K_{DP} estimations, provided that locations of no measurement are accounted for correctly after K_{DP} estimation.

There are three factors in addition to K_{DP} that affect Ψ_{DP} measurements that could impact K_{DP} retrieval - noise, backscatter differential phase, and negative K_{DP} - each of which are added individually to the synthetic Ψ_{DP} profile in this analysis. The results from allowing negative K_{DP} were unsurprising, in that the methods that do not allow K_{DP} estimations to be negative (UKMO and Maesaka) produced regions of 0 $^{\circ}\,km^{-1}$ where the rest of the methods were estimating negative K_{DP}. Negative K_{DP} was included by moving the truncation of the 'true' K_{DP} profile from 0 $^{\circ}\,km^{-1}$ to -0.2 $^{\circ}\,km^{-1}$, producing large regions of negative K_{DP}. This is not particularly realistic, as negative K_{DP} is mainly seen in small areas where ice crystals become vertically aligned due to strong electric fields in the clouds. However, there is nothing in the results, or in the methodology of each estimation, to suggest that they would not be able to estimate small, localised negative K_{DP}.

Backscatter differential phase (δ) is a phase shift that occurs upon the electromagnetic beam scattering from targets, as opposed to the shift due to propagation through them. δ is almost non-existent in ice crystals and small raindrops, and is small in large raindrops; however, it can be large and non-negligible for mixed-phase hydrometeors, such as melting snow seen throughout the melting layer. A corresponding δ profile was then added to the synthetic Ψ_{DP} profile, including a large 'δ-bump' in the middle of the profile replicating the melting layer. None of the methods correctly removed δ and reproduced the 'true' K_{DP} profile, instead they all over-estimated K_{DP} ahead of the peak of the δ-bump and under-estimated K_{DP} behind that peak. This is in spite of some methods (Schneebeli, Bringi, and Maesaka) explicitly accounting for δ in their retrieval.

However, the addition of noise to the Ψ_{DP} profile has the biggest impact on the accuracy of the estimated K_{DP} profiles. The estimated profiles still follow that of the 'true' K_{DP}, with a bit of oscillation around the 'truth' due to the noise; however, in the melting layer, where the standard deviation of Ψ_{DP}, and therefore the noise in Ψ_{DP}, is greatest,

there is a lot more variability in the estimation of K_{DP}. This is particularly the case in the wradlib method, the Ryzhkov method in high reflectivity, and the UKMO method, resulting in the biggest drop in correlation coefficient and biggest increase in mean absolute error when compared to the 'true' profile. Therefore, removing as much noise as possible from the Ψ_{DP} profile is key to accurate K_{DP} estimations; however, as none of the methods can completely remove noise from the collected data, it is important to consider noise in the phase measurements when setting radar parameters if accurate K_{DP} estimations are required. As discussed in section 2.1.4, the standard deviation in the K_{DP} estimation can be reduced by increasing the number of pulses used in each measurement or increasing the pulse repetition period, but these changes also decrease the measurement range and increase the time between measurements.

When looking at observations, there is no truth that can be used to compare each method with, and so the methods are compared to each other instead. This shows low correlation coefficient (<0.6, and often <0.4) between most of the methods, suggesting that those methods together are not converging around a common solution; however, three of the methods show high correlation (>0.7) between each other: Bringi, Ryzhkov and Rainbow (which could not be used in the first section). The similarity between Bringi and Rainbow is unsurprising, as they are based on the same methodology; however, the inclusion of the Ryzhkov method is surprising, as it is a very simple method that just smooths Ψ_{DP} using an averaging window, and then estimates K_{DP} as a slope of a least squares linear fit. The inclusion of the Ryzhkov method here is also unexpected because of the noisy estimations previously seen when there is high reflectivity and noise in the Ψ_{DP} profile. In the observations used, there is very little data that reaches the threshold of 40 dBZ needed for the high reflectivity estimation, instead the larger window size of the low reflectivity estimation is used which more aggressively smooths out the sudden changes in Ψ_{DP}. This may mean that the threshold is not suitable for this data, particularly as this looks at X-band observations collected in the UK rather than the S-band radars in the USA that this method was developed on, or simply that the removal of convective cases means that only lower reflectivity values are observed in this dataset, and the results would be different for convective observations.

The Bringi method returns amongst the highest correlation coefficient and lowest mean absolute error when compared with the synthetic 'true' profile across most of the scenarios, although the Bringi method does not deal well with individual missing data points, which results in large parts of the estimated profile having no value K_{DP} being estimated. Linearly interpolating the Ψ_{DP} profile before estimating K_{DP} removes this issue, but also results in statistics similar, or very slightly worse than, the Ryzhkov

method when looking at low reflectivity regions (below 40 dBZ); however, the Bringi method performs better than the Ryzhkov method for higher reflectivity, based on its higher correlation coefficient and lower mean absolute error when compared with the 'true' profile (figures 4.23 & 4.24). In regions where backscatter differential phase is present or there is noise within the measurement, the Bringi method may be the best choice; however, if there are individual missing data points along the ray then another method, or interpolation, may be more applicable to retrieve a full profile, and when there is little noise within the measurement then most methods return reasonable results.

Therefore, while one method may work best in some cases, or for certain types of weather or different wavelengths of radar (which is not directly explored in this study), that method might not be the best choice in other cases. This also means that any retrieval relation, for example for rain rate, or ice or liquid water content, might not be directly applicable from one estimation method to another. One should not necessarily expect to be able to take any relation in the literature and expect it to achieve the greatest accuracy, instead it should ideally be adjusted with the K_{DP} being estimated, where the corresponding observations are available. For example, using a K_{DP} - rain rate relation derived and tested using one particular K_{DP} estimation method may not provide rainfall rate estimations with the accuracy determined in its testing, for optimal results it should be tested and adjusted using rainfall rate measurements near the radar.

7.1.2 Chapter 5: Change of estimated K_{DP} with radar elevation angle.

In this section, how K_{DP} is affected by changing the radar elevation angle, and therefore the viewing geometry of hydrometeors, is studied. While the theoretical change of Z_{dr} with elevation angle had been shown observationally (Ryzhkov et al. 2005a), the same had not been done with observations of K_{DP} to prove a theoretically derived equation between K_{DP} and radar elevation angle (Schneebeli et al. 2013; Lu et al. 2015). In Chapter 5 observations are presented which support the theory, and then further studied to potentially constrain uncertainty in adjusting K_{DP} from high elevation angles (>70°) to 0° elevation.

Radar data from stratiform weather across 26 days were used to show how elevation angle affects K_{DP}. This data was binned by reflectivity and temperature (taken from the Met Office UK Atmospheric High Resolution Model), so that data from different days could be compared to each other. This showed a larger K_{DP} at 0° elevation angle

as reflectivity increases and as temperature decreases, which is explained by the vapour growth and aggregation of pristine plates and columns. These pristine ice crystals are observed at colder temperatures, and result in positive K_{DP} values when viewed from the side; however, when viewed from below their K_{DP} would tend to 0 $^\circ\, km^{-1}$ due to the random rotation in the horizontal plane of these crystals. Larger pristine crystals would appear longer and wider to the radar when viewed from the side, and so have larger K_{DP}. As temperature increases, these crystals aggregate, forming hydrometers that, while irregular in shape, appear more spherical to the radar, and therefore K_{DP} at side incidence will reduce.

Observations from the CIP-15 probe measured from the FAAM aircraft during one flight support this idea, but additional observations and modelling studies are needed to fully support this hypothesis.

Both Schneebeli et al. (2013) and Lu et al. (2015) mention the inadequacy of the theoretical equation at high elevation angles (>70°). The addition of reflectivity and temperature information can help with adjusting K_{DP} from high elevation angles to 0° elevation angle. Due to the small values of K_{DP} estimated at high elevation angles, any noise and uncertainty in the K_{DP} value (as explored through Chapter 4) would propagate through the adjustment and could result in unrealistically large estimations of adjusted K_{DP}. Knowledge of reflectivity and temperature could help constrain the adjustment of K_{DP} from high elevation angles; however, this would need further observations and modelling to achieve an adjustment that does not result in K_{DP} that is purely a function of reflectivity and temperature.

While there is little application for this, as for knowledge of the Z_{dr} change with elevation angle, in operational radar measurements due to the lower elevation angles used (20° or less), accounting for this change is shown to have an impact on the output from a hydrometeor classification algorithm applied to an RHI scan, as are often used in research (for example Kouketsu et al. (2015); Lang et al. (2016); Le et al. (2016); Chen et al. (2017); Roberto et al. (2017)). A case was studied where a hydrometeor classification algorithm returned aggregates at elevation angles greater than 20° and temperatures colder than -5 °C, while it returned dendrites in the same temperature region at lower elevation angles. By only using the equation in Schneebeli et al. (2013) and Lu et al. (2015), adjusting K_{DP} between elevation angles of 20° and 70° to K_{DP} at 0° elevation angle resulted in parts of this section being reclassified as dendrites, highlighting potential misclassification due to the viewing geometry and the general uncertainty associated with K_{DP}. However, above 70° elevation, use of this equation

resulted in large over-adjustment, and this region may benefit most from use of reflectivity and temperature data. Accurately adjusting K_{DP} at these high elevation angles could also help with quantitative precipitation estimation, microphysical retrievals, and comparison to in-situ data, where K_{DP} estimates are used.

7.1.3 Chapter 6: Comparison between radar forward operator output and radar observations of K_{DP}.

The final chapter looked at how output from a radar forward operator compared to observations taken from NXPol-1. Being able to accurately replicate polarimetric radar observables, such as K_{DP}, from model data can help improve microphysical schemes within the model (Ryzhkov et al. 2020), and assimilate radar data to improve the initial conditions used (Sun and Crook 1997; Gao and Stensrud 2012; Wang et al. 2013). The CR-SIM operator (Oue et al. 2020) was used to convert data from the WRF model to estimations of radar observables. The model was run three times for one case study using different double-moment bulk microphysical schemes: Thompson (Thompson et al. 2008), Milbrant (Milbrandt and Yau 2005a,b), and Morrison (Morrison et al. 2009). The WRF model run used a double-nested domain, with the domains centred over the location of the radar at Chilbolton Observatory, and the smallest domain using 400m horizontal grid spacing.

Visually accounting for the model getting the timing of the front wrong by about 30 minutes, the reflectivity and K_{DP} estimated by the forward operator look realistic around the front when compared to the radar observations. However, the values of reflectivity estimated from the Morrison and Thompson schemes were a little higher than the radar measurements, which is surprising given the lower rainfall amounts predicted by the model compared to the amount observed by a weather station at Chilbolton Observatory (lower reflectivity would be expected for lower rainfall). The output from these two microphysical schemes also resulted in higher K_{DP} estimations than from the Milbrant scheme; however, estimated values of K_{DP} from all three schemes fell into the range of values estimated by the Rainbow software from the observed Total Differential Phase.

However, behind the front in the ice region of the cloud, deficiencies in the forward operator result in significant deviations from the radar measurements. Microphysics schemes and forward operators rarely distinguish between different ice habits, and in CR-SIM all ice is treated as being at -30 °C. This generalisation of ice appears to con-

tribute to the model and forward operator missing an example of potential secondary ice production in this case study, where an area of elevated K_{DP} is present in the radar observations where the temperature is around -8 °C but not in the CR-SIM output. Secondary ice production is an important mechanism in explaining the difference between expected and observed ice particle concentrations, which play a key role in the development and evolution of clouds (Hallett and Mossop 1974; Field et al. 2017). Further cases need to be studied to confirm this deficiency in the forward operator, looking at times where both high and low values of K_{DP} are estimated from radar observations, and particularly at times when in-situ measurements are available from aircraft flights, such as liquid and ice water content and hydrometeor imaging.

To improve the estimations of the radar forward operators, more ice habits need to be represented to fully capture the polarimetric signatures, such as identifying areas of secondary ice production, that are seen in radar measurements. This could either be through including more ice habits in microphsyics schemes, which becomes computationally expensive, or through taking environmental information from the model and assume a dominant habit type or ice regime based on work such as that by Bailey and Hallett (2009). The inclusion of melting hydrometeors in the forward operator has been shown to improve the accuracy of forward operator estimations around the radar bright band (Jung et al. 2008; Dawson et al. 2014), and including further ice habit types may help to represent other radar signatures in ice, such as the dendritic growth zone (Kennedy and Rutledge 2011).

Improving forward operators has two key benefits. Weather surveillance radars provide a lot of information and measurements that are useful for constraining and improving microphysical schemes, provided the uncertainty in the measurements and operators are reduced and accounted for (Ryzhkov et al. 2020). Data from operational weather surveillance radars can also be used to help initialise NWP models. It has previously been shown that assimilating reflectivity can help reduce spin up time (Gao and Stensrud 2012) and improve precipitation forecasts (Jung et al. 2012); however, reflectivity alone is not sufficient to analyse all the variables in microphysics schemes (Jung et al. 2008). An accurate polarimetric radar forward operator could be used to assimilate dual-polarisation radar quantities, such as K_{DP}, to improve the forecast model initial conditions.

7.2 Summary

The aim of this thesis was to study uncertainty in Specific Differential Phase (K_{DP}) estimations from dual-polarisation radars, and the following key results have been identified:

- There is a lack of consistency between different methods of estimating K_{DP} from an artificial and a measured Ψ_{DP} profile. This inconsistency means that any retrieval relation derived for one method will not have the desired accuracy if used with another method, or potentially with another radar than that from which the original data came. Where data is available, relations should be tweaked and adjusted for each radar.

- None of the methods account well for the presence of non-negligible backscatter differential phase and noise in the Ψ_{DP} measurements. Extra steps should be taken to remove these before using any of these K_{DP} estimation methods, including consideration of radar settings such as pulse repetition frequency to minimise noise in the collected data.

- Interpolating the Ψ_{DP} measurements between individual missing data points improves the estimated K_{DP}; however, interpolating through noisy Ψ_{DP} decreases the quality of estimated K_{DP}. Therefore, removal of noise in the measurements should be done before any interpolation of Ψ_{DP}.

- Observations have been presented that confirm the theoretically derived equation in Schneebeli et al. (2013) and Lu et al. (2015) on how K_{DP} is affected by the radar elevation angle, and therefore the viewing geometry of hydrometeors.

- Using the equation relating K_{DP} and radar elevation angle, the output from a hydrometeor classification algorithm can be improved for elevation angles above 20°. For elevation angles above 70°, including reflectivity and temperature data may help to further improve the adjustment of K_{DP}; however, this needs to be tested through further observations and modelling.

- Polarimetric radar forward operators have the potential to unlock further uses of dual-polarisation radar data alongside numerical weather prediction output, but large inaccuracies exist, shown especially in the ice region of a frontal weather event, due to different ice habits not being distinguished between in models and forward operators.

- The generalisation of ice in numerical weather prediction models (NWP) and polarimetric radar forward operators contributes to polarimetric radar signatures, such as the increase in K_{DP} observed in areas of secondary ice production, not being replicated. Better representation of ice will result in better identification of these signatures, which can result in polarimetric measurements such as K_{DP} being used in data assimilation schemes to improve forecasting.

While there is promise in the use of K_{DP} for quantitative precipitation estimation, microphysical retrievals, and radar data assimilation based on the theory of K_{DP}, in practice there are issues regarding the accuracy of K_{DP} estimations, and a deficiency in the representation of ice in NWP models and forward operators, which have been highlighted and addressed in this thesis; however, this still much to be done before the full potential of K_{DP} will be realised.

References

Amitai, E., 2000: Systematic Variation of Observed Radar Reflectivity-Rainfall Rate Relations in the Tropics. *Journal of Applied Meteorology*, **39 (12)**, 2198–2208, doi: 10.1175/1520-0450(2001)040⟨2198:svoorr⟩2.0.co;2.

Andrić, J., M. R. Kumjian, D. S. Zrnić, J. M. Straka, and V. M. Melnikov, 2013: Polarimetric Signatures above the Melting Layer in Winter Storms: An Observational and Modeling Study. *Journal of Applied Meteorology and Climatology*, **52 (3)**, 682–700, doi:10.1175/jamc-d-12-028.1.

Austin, P. M., and A. C. Bemis, 1950: A QUANTITATIVE STUDY OF THE "BRIGHT BAND" IN RADAR PRECIPITATION ECHOES. *Journal of Meteorology*, **7 (2)**, 145–151, doi:10.1175/1520-0469(1950)007⟨0145:aqsotb⟩2.0.co;2.

Aydin, K., V. N. Bringi, and L. Liu, 1995: Rain-Rate Estimation in the Presence of Hail Using S-Band Specific Differential Phase and Other Radar Parameters. *Journal of Applied Meteorology*, **34 (2)**, 404–410, doi:10.1175/1520-0450-34.2.404.

Aydin, K., V. Giridhar, and Y. Zhao, 1991: Polarimetric C-band radar observables in melting hail: A computational study. *Preprints, 25th International Conference on Radar Meteorology*, American Meteorological Society, Paris, France, 733–736.

Aydin, K., T. A. Seliga, and V. Balaji, 1986: Remote Sensing of Hail with a Dual Linear Polarization Radar. *Journal of Climate and Applied Meteorology*, **25 (10)**, 1475–1484, doi:10.1175/1520-0450(1986)025⟨1475:rsohwa⟩2.0.co;2.

Aydin, K., and Y. Zhao, 1990: A computational study of polarimetric radar observables in hail. *IEEE Transactions on Geoscience and Remote Sensing*, **28 (4)**, 412–422, doi: 10.1109/tgrs.1990.572906.

Bailey, M. P., and J. Hallett, 2009: A Comprehensive Habit Diagram for Atmospheric Ice Crystals: Confirmation from the Laboratory, AIRS II, and Other Field Studies. *Journal of the Atmospheric Sciences*, **66 (9)**, 2888–2899, doi:10.1175/2009jas2883.1.

Baki, H., S. Chinta, C. Balaji, and B. Srinivasan, 2021: A sensitivity study of wrf model microphysics and cumulus parameterization schemes for the simulation of tropical cyclones using gpm radar data. *Journal of Earth System Science*, **130 (4)**, doi:10.1007/s12040-021-01682-3.

Ballard, S. P., Z. Li, D. Simonin, and J.-F. Caron, 2015: Performance of 4D-Var NWP-based nowcasting of precipitation at the Met Office for summer 2012. *Quarterly Journal of the Royal Meteorological Society*, **142 (694)**, 472–487, doi:10.1002/qj.2665.

Bao, J.-W., S. A. Michelson, and E. D. Grell, 2019: Microphysical process comparison of three microphysics parameterization schemes in the wrf model for an idealized squall-line case study. *Monthly Weather Review*, **147 (9)**, 3093–3120, doi:10.1175/mwr-d-18-0249.1.

Bebbington, D., R. McGuinness, and A. Holt, 1987: Correction of propagation effects in s-band circular polarisation-diversity radars. *IEE Proceedings H Microwaves, Antennas and Propagation*, **134 (5)**, 431, doi:10.1049/ip-h-2.1987.0087.

Bechini, R., L. Baldini, and V. Chandrasekar, 2013: Polarimetric Radar Observations in the Ice Region of Precipitating Clouds at C-Band and X-Band Radar Frequencies. *Journal of Applied Meteorology and Climatology*, **52 (5)**, 1147–1169, doi:10.1175/jamc-d-12-055.1.

Bechini, R., L. Baldini, R. Cremonini, and E. Gorgucci, 2008: Differential Reflectivity Calibration for Operational Radars. *J. Atmos. Oceanic Technol.*, **25**, 1542–1555, doi:10.1175/2008JTECHA1037.1.

Bennett, L., 2020: NCAS mobile X-band radar scan data from 1st November 2016 to 4th June 2018 deployed on long-term observations at the Chilbolton Facility for Atmospheric and Radio Research (CFARR), Hampshire, UK. Centre for Environmental Data Analysis, doi:10.5285/ffc9ed384aea471dab35901cf62f70be.

Bodas-Salcedo, A., M. J. Webb, M. E. Brooks, M. A. Ringer, K. D. Williams, S. F. Milton, and D. R. Wilson, 2008: Evaluating cloud systems in the met office global forecast model using simulated cloudsat radar reflectivities. *Journal of Geophysical*

Research, **113**, doi:10.1029/2007jd009620.

Boerner, W.-M., M. El-Arini, C.-Y. Chan, and P. Mastoris, 1981: Polarization dependence in electromagnetic inverse problems. *IEEE Transactions on Antennas and Propagation*, **29 (2)**, 262–271, doi:10.1109/tap.1981.1142585.

Boodoo, S., D. Hudak, N. Donaldson, and M. Leduc, 2010: Application of Dual-Polarization Radar Melting-Layer Detection Algorithm. *Journal of Applied Meteorology and Climatology*, **49 (8)**, 1779–1793, doi:10.1175/2010jamc2421.1.

Borowska, L., and D. Zrnic, 2012: Use of Ground Clutter to Monitor Polarimetric Radar Calibration. *Journal of Atmospheric and Oceanic Technology*, **29 (2)**, 159–176, doi:10.1175/jtech-d-11-00036.1.

Botta, G., K. Aydin, and J. Verlinde, 2013: Variability in millimeter wave scattering properties of dendritic ice crystals. *Journal of Quantitative Spectroscopy and Radiative Transfer*, **131**, 105–114, doi:10.1016/j.jqsrt.2013.05.009.

Bouniol, D., and Coauthors, 2010: Using continuous ground-based radar and lidar measurements for evaluating the representation of clouds in four operational models. *Journal of Applied Meteorology and Climatology*, **49 (9)**, 1971–1991, doi:10.1175/2010jamc2333.1.

Brandes, E. A., G. Zhang, and J. Vivekanandan, 2002: Experiments in Rainfall Estimation with a Polarimetric Radar in a Subtropical Environment. *Journal of Applied Meteorology*, **41 (6)**, 674–685, doi:10.1175/1520-0450(2002)041⟨0674:eirewa⟩2.0.co;2.

Bringi, V., K. Mishra, M. Thurai, P. Kennedy, and T. Raupach, 2020: Retrieval of lower-order moments of the drop size distribution using CSU-CHILL X-band polarimetric radar: a case study. *Atmospheric Measurement Techniques*, **13 (9)**, 4727–4750, doi:10.5194/amt-13-4727-2020.

Bringi, V., M. Thurai, and R. Hannesen, 2007: Dual-Polarization Weather Radar Handbook 2nd Edition. Selex-Gematronik.

Brotzge, J. A., K. Droegemeier, and D. J. McLaughlin, 2006: Collaborative Adaptive Sensing of the Atmosphere. *Transportation Research Record: Journal of the Transportation Research Board*, **1948 (1)**, 144–151, doi:10.1177/0361198106194800116.

Bukovčić, P., A. Ryzhkov, D. Zrnić, and G. Zhang, 2018: Polarimetric Radar Relations for Quantification of Snow Based on Disdrometer Data. *Journal of Applied*

Meteorology and Climatology, **57 (1)**, 103–120, doi:10.1175/jamc-d-17-0090.1.

Chen, H., V. Chandrasekar, and R. Bechini, 2017: An Improved Dual-Polarization Radar Rainfall Algorithm (DROPS2.0): Application in NASA IFloodS Field Campaign. *Journal of Hydrometeorology*, **18 (4)**, 917–937, doi:10.1175/jhm-d-16-0124.1.

Connolly, P. J., A. J. Heymsfield, and T. W. Choularton, 2006: Modelling the influence of rimer surface temperature on the glaciation of intense thunderstorms: The rime-splinter mechanism of ice multiplication. *Quarterly Journal of the Royal Meteorological Society*, **132 (621C)**, 3059–3077, doi:10.1256/qj.05.45.

Dawson, D. T., E. R. Mansell, Y. Jung, L. J. Wicker, M. R. Kumjian, and M. Xue, 2014: Low-Level ZDR Signatures in Supercell Forward Flanks: The Role of Size Sorting and Melting of Hail. *Journal of the Atmospheric Sciences*, **71 (1)**, 276–299, doi:10.1175/jas-d-13-0118.1.

Dietrich, F., and D. West, 1988: An experimental radome panel evaluation. *IEEE Transactions on Antennas and Propagation*, **36 (11)**, 1566–1570, doi:10.1109/8.9706.

Doviak, R. J., V. Bringi, A. Ryzhkov, A. Zahrai, and D. Zrnic, 2000: Considerations for Polarimetric Upgrades to Operational WSR-88D Radars. *Journal of Atmospheric and Oceanic Technology*, **17 (3)**, 257–278, doi:10.1175/1520-0426(2000)017⟨0257:cfputo⟩2.0.co;2.

Doviak, R. J., and D. S. Zrnić, 1993: *Doppler Radar and Weather Observations*. Academic Press, 562 pp.

Dowell, D. C., L. J. Wicker, and C. Snyder, 2011: Ensemble Kalman Filter Assimilation of Radar Observations of the 8 May 2003 Oklahoma City Supercell: Influences of Reflectivity Observations on Storm-Scale Analyses. *Monthly Weather Review*, **139 (1)**, 272–294, doi:10.1175/2010mwr3438.1.

ECMWF, 2021: About our forecasts. Accessed 30 December 2021, https://www.ecmwf.int/en/forecasts/documentation-and-support#Atmospheric.

Fabry, F., 2015: *Radar Meteorology: Principles and Practice*. Cambridge University Press, 256 pp.

Fan, J., and Coauthors, 2017: Cloud-resolving model intercomparison of an MC3E squall line case: Part I-Convective updrafts. *Journal of Geophysical Research: Atmospheres*, **122 (17)**, 9351–9378, doi:10.1002/2017jd026622.

Fang, M., R. J. Doviak, and V. Melnikov, 2004: Spectrum Width Measured by WSR-88D: Error Sources and Statistics of Various Weather Phenomena. *Journal of Atmospheric and Oceanic Technology*, **21 (6)**, 888–904, doi:10.1175/1520-0426(2004)021⟨0888:swmbwe⟩2.0.co;2.

Field, P. R., R. Wood, P. R. A. Brown, P. H. Kaye, E. Hirst, R. Greenaway, and J. A. Smith, 2003: Ice Particle Interarrival Times Measured with a Fast FSSP. *Journal of Atmospheric and Oceanic Technology*, **20 (2)**, 249–261, doi:10.1175/1520-0426(2003)020⟨0249:ipitmw⟩2.0.co;2.

Field, P. R., and Coauthors, 2017: Chapter 7. Secondary Ice Production - current state of the science and recommendations for the future. *Meteorological Monographs*, doi:10.1175/amsmonographs-d-16-0014.1.

Gao, J., and D. J. Stensrud, 2012: Assimilation of Reflectivity Data in a Convective-Scale, Cycled 3DVAR Framework with Hydrometeor Classification. *Journal of the Atmospheric Sciences*, **69 (3)**, 1054–1065, doi:10.1175/jas-d-11-0162.1.

Gao, Y., L. R. Leung, C. Zhao, and S. Hagos, 2017: Sensitivity of U.S. summer precipitation to model resolution and convective parameterizations across gray zone resolutions. *Journal of Geophysical Research: Atmospheres*, **122 (5)**, 2714–2733, doi:10.1002/2016jd025896.

Goddard, J., M. Thurai, and J. Eastment, 1994: The Chilbolton Advanced Meteorological Radar: a tool for multidisciplinary atmospheric research. *Electronics & Communication Engineering Journal*, **6 (2)**, 77–86, doi:10.1049/ecej:19940205.

Gorgucci, E., G. Scarchilli, and V. Chandrasekar, 1992: Calibration of radars using polarimetric techniques. *IEEE Trans. Geosci. Remote Sens*, **30**, 853–858, doi:10.1109/36.175319.

Gorgucci, E., G. Scarchilli, and V. Chandrasekar, 1999a: A procedure to calibrate multiparameter weather radar using properties of the rain medium. *IEEE Transactions on Geoscience and Remote Sensing*, **37 (1)**, 269–276, doi:10.1109/36.739161.

Gorgucci, E., G. Scarchilli, and V. Chandrasekar, 1999b: Specific Differential Phase Estimation in the Presence of Nonuniform Rainfall Medium along the Path. *Journal of Atmospheric and Oceanic Technology*, **16 (11)**, 1690–1697, doi:10.1175/1520-0426(1999)016⟨1690:sdpeit⟩2.0.co;2.

Gourley, J. J., A. J. Illingworth, and P. Tabary, 2009: Absolute Calibration of Radar Reflectivity Using Redundancy of the Polarization Observations and Implied Constraints on Drop Shapes. *Journal of Atmospheric and Oceanic Technology*, **26 (4)**, 689–703, doi:10.1175/2008jtecha1152.1.

Gourley, J. J., P. Tabary, and J. Parent du Chatelet, 2006: Data Quality of the Meteo-France C-Band Polarimetric Radar. *Journal of Atmospheric and Oceanic Technology*, **23 (10)**, 1340–1356, doi:10.1175/jtech1912.1.

Grabowski, W. W., H. Morrison, S.-I. Shima, G. C. Abade, P. Dziekan, and H. Pawlowska, 2019: Modeling of Cloud Microphysics: Can We Do Better? *Bulletin of the American Meteorological Society*, **100 (4)**, 655–672, doi:10.1175/bams-d-18-0005.1.

Griffin, E. M., T. J. Schuur, and A. V. Ryzhkov, 2018: A Polarimetric Analysis of Ice Microphysical Processes in Snow, Using Quasi-Vertical Profiles. *Journal of Applied Meteorology and Climatology*, **57 (1)**, 31–50, doi:10.1175/jamc-d-17-0033.1.

Gu, J.-Y., A. Ryzhkov, P. Zhang, P. Neilley, M. Knight, B. Wolf, and D.-I. Lee, 2011: Polarimetric Attenuation Correction in Heavy Rain at C Band. *Journal of Applied Meteorology and Climatology*, **50 (1)**, 39–58, doi:10.1175/2010jamc2258.1.

Hallett, J., and S. C. Mossop, 1974: Production of secondary ice particles during the riming process. *Nature*, **249 (5452)**, 26–28, doi:10.1038/249026a0.

Harrington, J. Y., K. Sulia, and H. Morrison, 2013: A Method for Adaptive Habit Prediction in Bulk Microphysical Models. Part I: Theoretical Development. *Journal of the Atmospheric Sciences*, **70 (2)**, 349–364, doi:10.1175/jas-d-12-040.1.

Harrison, D., K. Norman, T. Darlington, D. Adams, N. Husnoo, C. Sandford, and S. Best, 2015: The evolution of the Met Office radar data quality control and product generation system: Radarnet. *Preprints, 37th International Conference on Radar Meteorology*, American Meteorological Society, Norman, USA.

Hawkness-Smith, L. D., and D. Simonin, 2021: Radar reflectivity assimilation using hourly cycling 4D-Var in the Met Office Unified Model. *Quarterly Journal of the Royal Meteorological Society*, **147 (736)**, 1516–1538, doi:10.1002/qj.3977.

Heistermann, M., S. Jacobi, and T. Pfaff, 2013: Technical Note: An open source library for processing weather radar data (wradlib). *Hydrology and Earth System Sciences*,

17 (2), 863–871, doi:10.5194/hess-17-863-2013.

Helmus, J. J., and S. M. Collis, 2016: The Python ARM Radar Toolkit (Py-ART), a Library for Working with Weather Radar Data in the Python Programming Language. *Journal of Open Research Software*, **4**, doi:10.5334/jors.119.

Hogan, R. J., N. Gaussiat, and A. J. Illingworth, 2005: Stratocumulus Liquid Water Content from Dual-Wavelength Radar. *Journal of Atmospheric and Oceanic Technology*, **22 (8)**, 1207–1218, doi:10.1175/jtech1768.1.

Holt, A. R., and R. McGuinness, 1990: *Rainrate Measurements Using a Circular Polarisation-Diversity Radar*, 304–313. Springer Netherlands, Dordrecht, doi:10.1007/978-94-009-0551-1_35.

Houser, J. L., H. B. Bluestein, and J. C. Snyder, 2016: A Finescale Radar Examination of the Tornadic Debris Signature and Weak-Echo Reflectivity Band Associated with a Large, Violent Tornado. *Monthly Weather Review*, **144 (11)**, 4101–4130, doi:10.1175/mwr-d-15-0408.1.

Huang, H., G. Zhang, K. Zhao, S. Liu, L. Wen, G. Chen, and Z. Yang, 2019: Uncertainty in Retrieving Raindrop Size Distribution from Polarimetric Radar Measurements. *Journal of Atmospheric and Oceanic Technology*, **36 (4)**, 585–605, doi:10.1175/jtech-d-18-0107.1.

Huang, Y., Y. Wang, L. Xue, X. Wei, L. Zhang, and H. Li, 2020: Comparison of three microphysics parameterization schemes in the wrf model for an extreme rainfall event in the coastal metropolitan city of guangzhou, china. *Atmospheric Research*, **240**, 104 939, doi:10.1016/j.atmosres.2020.104939.

Hubbert, J., and V. N. Bringi, 1995: An Iterative Filtering Technique for the Analysis of Copolar Differential Phase and Dual-Frequency Radar Measurements. *Journal of Atmospheric and Oceanic Technology*, **12 (3)**, 643–648, doi:10.1175/1520-0426(1995)012⟨0643:aiftft⟩2.0.co;2.

Huynen, J., 1970: Phenomenological theory of radar targets. Ph.D. thesis, Delft University of Technology, Delft, Netherlands, URL https://repository.tudelft.nl/islandora/object/uuid:e4a140a0-c175-45a7-ad41-29b28361b426.

Igel, A. L., M. R. Igel, and S. C. van den Heever, 2015: Make It a Double? Sobering Results from Simulations Using Single-Moment Microphysics Schemes. *Journal of*

the Atmospheric Sciences, **72 (2)**, 910–925, doi:10.1175/jas-d-14-0107.1.

Ilotoviz, E., A. Khain, A. V. Ryzhkov, and J. C. Snyder, 2018: Relationship between Aerosols, Hail Microphysics, and ZDR Columns. *Journal of the Atmospheric Sciences*, **75 (6)**, 1755–1781, doi:10.1175/jas-d-17-0127.1.

Istok, M. J., and R. J. Doviak, 1986: Analysis of the Relation Between Doppler Spectral Width and Thunderstorm Turbulence. *Journal of the Atmospheric Sciences*, **43 (20)**, 2199–2214, doi:10.1175/1520-0469(1986)043⟨2199:aotrbd⟩2.0.co;2.

Jameson, A., 1992: The Effect of Temperature on Attenuation-Correction Schemes in Rain Using Polarization Propagation Differential Phase Shift. *Journal of Applied Meteorology and Climatology*, **31 (9)**, 1106–1118, doi:10.1175/1520-0450(1992)031⟨1106:TEOTOA⟩2.0.CO;2.

Jung, Y., M. Xue, and M. Tong, 2012: Ensemble Kalman Filter Analyses of the 29-30 May 2004 Oklahoma Tornadic Thunderstorm Using One- and Two-Moment Bulk Microphysics Schemes, with Verification against Polarimetric Radar Data. *Monthly Weather Review*, **140 (5)**, 1457–1475, doi:10.1175/mwr-d-11-00032.1.

Jung, Y., G. Zhang, and M. Xue, 2008: Assimilation of Simulated Polarimetric Radar Data for a Convective Storm Using the Ensemble Kalman Filter. Part I: Observation Operators for Reflectivity and Polarimetric Variables. *Monthly Weather Review*, **136 (6)**, 2228–2245, doi:10.1175/2007mwr2083.1.

Kain, J. S., 2004: The Kain-Fritsch Convective Parameterization: An Update. *Journal of Applied Meteorology*, **43 (1)**, 170–181, doi:10.1175/1520-0450(2004)043⟨0170:tkcpau⟩2.0.co;2.

Kennaugh, E., 1952: Polarization Properties of Radar Reflections. M.S. thesis, The Ohio State University, URL https://etd.ohiolink.edu/apexprod/rws_etd/send_file/send?accession=osu1235238411&disposition=inline.

Kennedy, P. C., and S. A. Rutledge, 2011: S-Band Dual-Polarization Radar Observations of Winter Storms. *Journal of Applied Meteorology and Climatology*, **50 (4)**, 844–858, doi:10.1175/2010jamc2558.1.

Kerns, B. W., and S. S. Chen, 2014: ECMWF and GFS model forecast verification during DYNAMO: Multiscale variability in MJO initiation over the equatorial Indian Ocean. *Journal of Geophysical Research: Atmospheres*, **119 (7)**, 3736–3755, doi:

10.1002/2013jd020833.

Khain, A., A. Pokrovsky, M. Pinsky, A. Seifert, and V. Phillips, 2004: Simulation of Effects of Atmospheric Aerosols on Deep Turbulent Convective Clouds Using a Spectral Microphysics Mixed-Phase Cumulus Cloud Model. Part I: Model Description and Possible Applications. *Journal of the Atmospheric Sciences*, **61 (24)**, 2963–2982, doi:10.1175/jas-3350.1.

Kim, T.-J., H.-H. Kwon, and K. B. Kim, 2021: Calibration of the reflectivity-rainfall rate (Z-R) relationship using long-term radar reflectivity factor over the entire South Korea region in a Bayesian perspective. *Journal of Hydrology*, **593**, 125 790, doi: 10.1016/j.jhydrol.2020.125790.

Knievel, J. C., D. A. Ahijevych, and K. W. Manning, 2004: Using Temporal Modes of Rainfall to Evaluate the Performance of a Numerical Weather Prediction Model. *Monthly Weather Review*, **132 (12)**, 2995–3009, doi:10.1175/mwr2828.1.

Korolev, A., and Coauthors, 2017: Mixed-Phase Clouds: Progress and Challenges. *Meteorological Monographs*, **58**, 5.1–5.50, doi:10.1175/amsmonographs-d-17-0001.1.

Kouketsu, T., and Coauthors, 2015: A Hydrometeor Classification Method for X-Band Polarimetric Radar: Construction and Validation Focusing on Solid Hydrometeors under Moist Environments. *Journal of Atmospheric and Oceanic Technology*, **32 (11)**, 2052–2074, doi:10.1175/jtech-d-14-00124.1.

Kumjian, M., 2013: Principles and applications of dual-polarization weather radar. Part I: Description of the polarimetric radar variables. *Journal of Operational Meteorology*, **1 (19)**, 226–242, doi:10.15191/nwajom.2013.0119.

Kumjian, M. R., Y. P. Richardson, T. Meyer, K. A. Kosiba, and J. Wurman, 2018: Resonance Scattering Effects in Wet Hail Observed with a Dual-X-Band-Frequency, Dual-Polarization Doppler on Wheels Radar. *Journal of Applied Meteorology and Climatology*, **57 (12)**, 2713–2731, doi:10.1175/jamc-d-17-0362.1.

Ladd, D., and Coauthors, 2017: Technical description of a novel sensor network architecture and results of radar and optical sensors contributing to a UK cueing experiment. *Proceedings of the Advanced Maui Optical and Space Surveillance (AMOS) Conference*, Maui, USA, https://amostech.com/TechnicalPapers/2017/Poster/Ladd.pdf.

Lang, T., B. Dolan, N. Guy, C. Gerlach, and J. Hardin, 2019: CSU-Radarmet/CSU_RadarTools: CSU_RadarTools v1.3. Zenodo, URL https://doi.org/10.5281/zenodo.2562063, doi:10.5281/zenodo.2562063.

Lang, T. J., and Coauthors, 2016: Observations of two sprite-producing storms in Colorado. *Journal of Geophysical Research: Atmospheres*, **121 (16)**, 9675–9695, doi:10.1002/2016jd025299.

Le, M., V. Chandrasekar, and S. Biswas, 2016: Evaluation and Validation of GPM Dual-Frequency Classification Module after Launch. *Journal of Atmospheric and Oceanic Technology*, **33 (12)**, 2699–2716, doi:10.1175/jtech-d-15-0253.1.

Li, Z., and G. Zhang, 2022: Differences in Spectrum Width Estimates Between Electronic Scans and Mechanical Scans With a Phased Array Weather Radar. *IEEE Geoscience and Remote Sensing Letters*, **19**, 1–5, doi:10.1109/lgrs.2022.3186666.

Lim, S., and V. Chandrasekar, 2016: A Robust Attenuation Correction System for Reflectivity and Differential Reflectivity in Weather Radars. *IEEE Transactions on Geoscience and Remote Sensing*, **54 (3)**, 1727–1737, doi:10.1109/tgrs.2015.2487984.

Lin, Y.-L., R. D. Farley, and H. D. Orville, 1983: Bulk Parameterization of the Snow Field in a Cloud Model. *Journal of Climate and Applied Meteorology*, **22 (6)**, 1065–1092, doi:10.1175/1520-0450(1983)022⟨1065:bpotsf⟩2.0.co;2.

Liu, H., and V. Chandrasekar, 2000: Classification of Hydrometeors Based on Polarimetric Radar Measurements: Development of Fuzzy Logic and Neuro-Fuzzy Systems, and In Situ Verification. *Journal of Atmospheric and Oceanic Technology*, **17 (2)**, 140–164, doi:10.1175/1520-0426(2000)017⟨0140:cohbop⟩2.0.co;2.

Lloyd, G., and Coauthors, 2015: The origins of ice crystals measured in mixed-phase clouds at the high-alpine site Jungfraujoch. *Atmospheric Chemistry and Physics*, **15 (22)**, 12 953–12 969, doi:10.5194/acp-15-12953-2015.

Loftus, A., and W. Cotton, 2014: A triple-moment hail bulk microphysics scheme. Part II: Verification and comparison with two-moment bulk microphysics. *Atmospheric Research*, **150**, 97–128, doi:10.1016/j.atmosres.2014.07.016.

Loftus, A., W. Cotton, and G. Carrió, 2014: A triple-moment hail bulk microphysics scheme. Part I: Description and initial evaluation. *Atmospheric Research*, **149**, 35–57, doi:10.1016/j.atmosres.2014.05.013.

Louf, V., A. Protat, R. A. Warren, S. M. Collis, D. B. Wolff, S. Raunyiar, C. Jakob, and W. A. Petersen, 2019: An Integrated Approach to Weather Radar Calibration and Monitoring Using Ground Clutter and Satellite Comparisons. *Journal of Atmospheric and Oceanic Technology*, **36 (1)**, 17–39, doi:10.1175/jtech-d-18-0007.1.

Lu, Y., K. Aydin, E. E. Clothiaux, and J. Verlinde, 2015: Retrieving Cloud Ice Water Content Using Millimeter- and Centimeter-Wavelength Radar Polarimetric Observables. *J. Appl. Meteor. Climatol.*, **54**, 596–604, doi:10.1175/JAMC-D-14-0169.1.

Lynch, P., 2006: *The Emergence of Numerical Weather Prediction*. Cambridge University Press, 279 pp.

Maesaka, T., K. Iwanami, and M. Maki, 2012: Non-negative KDP Estimation by Monotone Increasing PHIDP Assumption below Melting Layer. *The Seventh European Conference on Radar in Meteorology and Hydrology*, European Conference on Radar in Meteorology and Hydrology, Toulouse, France.

Mancini, A., J. L. Salazar, R. M. Lebrón, and B. L. Cheong, 2018: A Novel Instrument for Real-Time Measurement of Attenuation of Weather Radar Radome Including Its Outer Surface. Part I: The Concept. *Journal of Atmospheric and Oceanic Technology*, **35 (5)**, 953–973, doi:10.1175/jtech-d-17-0083.1.

Marks, D. A., D. B. Wolff, L. D. Carey, and A. Tokay, 2011: Quality Control and Calibration of the Dual-Polarization Radar at Kwajalein, RMI. *Journal of Atmospheric and Oceanic Technology*, **28 (2)**, 181–196, doi:10.1175/2010jtecha1462.1.

Marshall, J. S., and W. M. K. Palmer, 1948: THE DISTRIBUTION OF RAINDROPS WITH SIZE. *Journal of Meteorology*, **5 (4)**, 165–166, doi:10.1175/1520-0469(1948)005⟨0165:tdorws⟩2.0.co;2.

Matrosov, S. Y., R. Cifelli, P. C. Kennedy, S. W. Nesbitt, S. A. Rutledge, V. N. Bringi, and B. E. Martner, 2006: A Comparative Study of Rainfall Retrievals Based on Specific Differential Phase Shifts at X- and S-Band Radar Frequencies. *Journal of Atmospheric and Oceanic Technology*, **23 (7)**, 952–963, doi:10.1175/jtech1887.1.

Matrosov, S. Y., D. E. Kingsmill, B. E. Martner, and F. M. Ralph, 2005: The Utility of X-Band Polarimetric Radar for Quantitative Estimates of Rainfall Parameters. *Journal of Hydrometeorology*, **6 (3)**, 248–262, doi:10.1175/jhm424.1.

Matrosov, S. Y., R. F. Reinking, R. A. Kropfli, B. E. Martner, and B. W. Bartram,

2001: On the Use of Radar Depolarization Ratios for Estimating Shapes of Ice Hydrometeors in Winter Clouds. *Journal of Applied Meteorology*, **40 (3)**, 479–490, doi:10.1175/1520-0450(2001)040⟨0479:otuord⟩2.0.co;2.

McFarquhar, G. M., J. Um, M. Freer, D. Baumgardner, G. L. Kok, and G. Mace, 2007: Importance of small ice crystals to cirrus properties: Observations from the Tropical Warm Pool International Cloud Experiment (TWP-ICE). *Geophysical Research Letters*, **34 (13)**, L13 803, doi:10.1029/2007gl029865.

Melnikov, V. M., R. J. Doviak, D. S. Zrnic, and D. J. Stensrud, 2011: Mapping Bragg Scatter with a Polarimetric WSR-88D. *Journal of Atmospheric and Oceanic Technology*, **28 (10)**, 1273–1285, doi:10.1175/jtech-d-10-05048.1.

Melnikov, V. M., M. J. Istok, and J. K. Westbrook, 2015: Asymmetric Radar Echo Patterns from Insects. *Journal of Atmospheric and Oceanic Technology*, **32 (4)**, 659–674, doi:10.1175/jtech-d-13-00247.1.

Meneghini, R., 1978: Rain-rate estimates for an attenuating radar. *Radio Science*, **13 (3)**, 459–470, doi:10.1029/rs013i003p00459.

Met Office, 2016: NWP-UKV: Met Office UK Atmospheric High Resolution Model data. Centre for Environmental Data Analysis, https://catalogue.ceda.ac.uk/uuid/f47bc62786394626b665e23b658d385f.

Met Office, 2019: History of numerical weather prediction. Accessed 3 November 2021, https://www.metoffice.gov.uk/weather/learn-about/how-forecasts-are-made/computer-models/history-of-numerical-weather-prediction.

Met Office, 2021: Supercomputing leap in weather and climate forecasting. Accessed 5 November 2021, https://www.metoffice.gov.uk/about-us/press-office/news/corporate/2021/met-office-and-microsoft-announce-supercomputer-project.

Milbrandt, J. A., and M. K. Yau, 2005a: A Multimoment Bulk Microphysics Parameterization. Part I: Analysis of the Role of the Spectral Shape Parameter. *Journal of the Atmospheric Sciences*, **62 (9)**, 3051–3064, doi:10.1175/jas3534.1.

Milbrandt, J. A., and M. K. Yau, 2005b: A Multimoment Bulk Microphysics Parameterization. Part II: A Proposed Three-Moment Closure and Scheme Description. *Journal of the Atmospheric Sciences*, **62 (9)**, 3065–3081, doi:10.1175/jas3535.1.

Milbrandt, J. A., and M. K. Yau, 2006a: A Multimoment Bulk Microphysics Parame-

terization. Part III: Control Simulation of a Hailstorm. *Journal of the Atmospheric Sciences*, **63 (12)**, 3114–3136, doi:10.1175/jas3816.1.

Milbrandt, J. A., and M. K. Yau, 2006b: A Multimoment Bulk Microphysics Parameterization. Part IV: Sensitivity Experiments. *Journal of the Atmospheric Sciences*, **63 (12)**, 3137–3159, doi:10.1175/jas3817.1.

Milbrandt, J. A., M. K. Yau, J. Mailhot, and S. Bélair, 2008: Simulation of an Orographic Precipitation Event during IMPROVE-2. Part I: Evaluation of the Control Run Using a Triple-Moment Bulk Microphysics Scheme. *Monthly Weather Review*, **136 (10)**, 3873–3893, doi:10.1175/2008mwr2197.1.

Mishchenko, M. I., 2000: Calculation of the amplitude matrix for a nonspherical particle in a fixed orientation. *Applied Optics*, **39 (6)**, 1026, doi:10.1364/ao.39.001026.

Moisseev, D. N., S. Lautaportti, J. Tyynela, and S. Lim, 2015: Dual-polarization radar signatures in snowstorms: Role of snowflake aggregation. *Journal of Geophysical Research: Atmospheres*, **120 (24)**, 12 644–12 655, doi:10.1002/2015jd023884.

Morrison, H., J. A. Curry, and V. I. Khvorostyanov, 2005: A New Double-Moment Microphysics Parameterization for Application in Cloud and Climate Models. Part I: Description. *Journal of the Atmospheric Sciences*, **62 (6)**, 1665–1677, doi:10.1175/jas3446.1.

Morrison, H., J. A. Milbrandt, G. H. Bryan, K. Ikeda, S. A. Tessendorf, and G. Thompson, 2015: Parameterization of Cloud Microphysics Based on the Prediction of Bulk Ice Particle Properties. Part II: Case Study Comparisons with Observations and Other Schemes. *Journal of the Atmospheric Sciences*, **72 (1)**, 312–339, doi:10.1175/jas-d-14-0066.1.

Morrison, H., G. Thompson, and V. Tatarskii, 2009: Impact of Cloud Microphysics on the Development of Trailing Stratiform Precipitation in a Simulated Squall Line: Comparison of One- and Two-Moment Schemes. *Monthly Weather Review*, **137 (3)**, 991–1007, doi:10.1175/2008mwr2556.1.

Morrison, H., and Coauthors, 2020: Confronting the challenge of Modeling Cloud and precipitation microphysics. *Journal of Advances in Modeling Earth Systems*, **12 (8)**, doi:10.1029/2019ms001689.

Nam, C. C. W., and J. Quaas, 2012: Evaluation of clouds and precipitation in the

echam5 general circulation model using calipso and cloudsat satellite data. *Journal of Climate*, **25 (14)**, 4975–4992, doi:10.1175/jcli-d-11-00347.1.

NCEP, 2022: NCEP Operational HWRF Forecasting System. Accessed 8 February 2022, https://www.emc.ncep.noaa.gov/gc_wmb/vxt/HWRF/.

Neely III, R. R., and Coauthors, 2018: The NCAS mobile dual-polarisation Doppler X-band weather radar (NXPol). *Atmospheric Measurement Techniques*, **11 (12)**, 6481–6494, doi:10.5194/amt-11-6481-2018.

Oue, M., M. R. Kumjian, Y. Lu, Z. Jiang, E. E. Clothiaux, J. Verlinde, and K. Aydin, 2015: X-Band Polarimetric and Ka-Band Doppler Spectral Radar Observations of a Graupel-Producing Arctic Mixed-Phase Cloud. *Journal of Applied Meteorology and Climatology*, **54 (6)**, 1335–1351, doi:10.1175/jamc-d-14-0315.1.

Oue, M., A. Tatarevic, P. Kollias, D. Wang, K. Yu, and A. M. Vogelmann, 2020: The Cloud-resolving model Radar SIMulator (CR-SIM) Version 3.3: description and applications of a virtual observatory. *Geoscientific Model Development*, **13 (4)**, 1975–1998, doi:10.5194/gmd-13-1975-2020.

Overeem, A., H. de Vries, H. Al Sakka, R. Uijlenhoet, and H. Leijnse, 2021: Rainfall-induced attenuation correction for two operational dual-polarization C-band radars in the Netherlands. *Journal of Atmospheric and Oceanic Technology*, doi:10.1175/jtech-d-20-0113.1.

Paulitsch, H., F. Teschl, and W. L. Randeu, 2009: Dual-polarization C-band weather radar algorithms for rain rate estimation and hydrometeor classification in an alpine region. *Advances in Geosciences*, **20**, 3–8, doi:10.5194/adgeo-20-3-2009.

Picca, J., and A. Ryzhkov, 2012: A Dual-Wavelength Polarimetric Analysis of the 16 May 2010 Oklahoma City Extreme Hailstorm. *Monthly Weather Review*, **140 (4)**, 1385–1403, doi:10.1175/mwr-d-11-00112.1.

Pickering, B. S., R. R. Neely III, and D. Harrison, 2019: The Disdrometer Verification Network (DiVeN): a UK network of laser precipitation instruments. *Atmospheric Measurement Techniques*, **12 (11)**, 5845–5861, doi:10.5194/amt-12-5845-2019.

Richardson, L. F., and P. Lynch, 2007: *Weather Prediction by Numerical Process*. 2nd ed., Cambridge Mathematical Library, Cambridge University Press, 236 pp., doi:10.1017/CBO9780511618291.

Rinehart, R. E., and E. T. Garvey, 1978: Three-dimensional storm motion detection by conventional weather radar. *Nature*, **273**, 287–289, doi:10.1038/273287a0.

Roberto, N., L. Baldini, E. Adirosi, L. Facheris, F. Cuccoli, A. Lupidi, and A. Garzelli, 2017: A Support Vector Machine Hydrometeor Classification Algorithm for Dual-Polarization Radar. *Atmosphere*, **8 (12)**, 134, doi:10.3390/atmos8080134.

Rogers, R., 2010: Convective-Scale Structure and Evolution during a High-Resolution Simulation of Tropical Cyclone Rapid Intensification. *Journal of the Atmospheric Sciences*, **67 (1)**, 44–70, doi:10.1175/2009jas3122.1.

Ryzhkov, A., M. Diederich, P. Zhang, and C. Simmer, 2014: Potential Utilization of Specific Attenuation for Rainfall Estimation, Mitigation of Partial Beam Blockage, and Radar Networking. *Journal of Atmospheric and Oceanic Technology*, **31 (3)**, 599–619, doi:10.1175/jtech-d-13-00038.1.

Ryzhkov, A., M. Pinsky, A. Pokrovsky, and A. Khain, 2011: Polarimetric Radar Observation Operator for a Cloud Model with Spectral Microphysics. *Journal of Applied Meteorology and Climatology*, **50 (4)**, 873–894, doi:10.1175/2010jamc2363.1.

Ryzhkov, A., and D. Zrnić, 1998a: Beamwidth Effects on the Differential Phase Measurements of Rain. *Journal of Atmospheric and Oceanic Technology*, **15 (3)**, 624–634, doi:10.1175/1520-0426(1998)015⟨0624:beotdp⟩2.0.co;2.

Ryzhkov, A. V., S. E. Giangrande, V. M. Melnikov, and T. J. Schuur, 2005a: Calibration Issues of Dual-Polarization Radar Measurements. *Journal of Atmospheric and Oceanic Technology*, **22 (8)**, 1138–1155, doi:10.1175/jtech1772.1.

Ryzhkov, A. V., T. J. Schuur, D. W. Burgess, P. L. Heinselman, S. E. Giangrande, and D. S. Zrnic, 2005b: The Joint Polarization Experiment: Polarimetric Rainfall Measurements and Hydrometeor Classification. *Bulletin of the American Meteorological Society*, **86 (6)**, 809–824, doi:10.1175/bams-86-6-809.

Ryzhkov, A. V., T. J. Schuur, D. W. Burgess, and D. S. Zrnic, 2005c: Polarimetric Tornado Detection. *Journal of Applied Meteorology*, **44 (5)**, 557–570, doi:10.1175/jam2235.1.

Ryzhkov, A. V., J. Snyder, J. T. Carlin, A. Khain, and M. Pinsky, 2020: What Polarimetric Weather Radars Offer to Cloud Modelers: Forward Radar Operators and Microphysical/Thermodynamic Retrievals. *Atmosphere*, **11 (4)**, 362, doi:

10.3390/atmos11040362.

Ryzhkov, A. V., and D. S. Zrnić, 1998b: Discrimination between Rain and Snow with a Polarimetric Radar. *Journal of Applied Meteorology*, **37 (10)**, 1228–1240, doi: 10.1175/1520-0450(1998)037⟨1228:dbrasw⟩2.0.co;2.

Ryzhkov, A. V., and D. S. Zrnić, 2019: *Radar Polarimetry for Weather Observations*. Springer Atmospheric Sciences, 486 pp., doi:10.1007/978-3-030-05093-1.

Ryzhkov, A. V., D. S. Zrnić, and B. A. Gordon, 1998: Polarimetric Method for Ice Water Content Determination. *Journal of Applied Meteorology*, **37 (2)**, 125–134, doi:10.1175/1520-0450(1998)037⟨0125:pmfiwc⟩2.0.co;2.

Sandford, C., A. Illingworth, and R. Thompson, 2017: The Potential Use of the Linear Depolarization Ratio to Distinguish between Convective and Stratiform Rainfall to Improve Radar Rain-Rate Estimates. *Journal of Applied Meteorology and Climatology*, **56 (11)**, 2927–2940, doi:10.1175/jamc-d-17-0014.1.

Sarabandi, K., and F. Ulaby, 1990: A convenient technique for polarimetric calibration of single-antenna radar systems. *IEEE Transactions on Geoscience and Remote Sensing*, **28 (6)**, 1022–1033, doi:10.1109/36.62627.

Schneebeli, M., N. Dawes, M. Lehning, and A. Berne, 2013: High-Resolution Vertical Profiles of X-Band Polarimetric Radar Observables during Snowfall in the Swiss Alps. *Journal of Applied Meteorology and Climatology*, **52 (2)**, 378–394, doi:10.1175/jamc-d-12-015.1.

Schneebeli, M., J. Grazioli, and A. Berne, 2014: Improved Estimation of the Specific Differential Phase Shift Using a Compilation of Kalman Filter Ensembles. *IEEE Transactions on Geoscience and Remote Sensing*, **52 (8)**, 5137–5149, doi:10.1109/tgrs.2013.2287017.

Schneebeli, M., J. Sakuragi, T. Biscaro, C. F. Angelis, I. Carvalho da Costa, C. Morales, L. Baldini, and L. A. T. Machado, 2012: Polarimetric X-band weather radar measurements in the tropics: radome and rain attenuation correction. *Atmospheric Measurement Techniques*, **5 (9)**, 2183–2199, doi:10.5194/amt-5-2183-2012.

Schuur, T., A. Ryzhkov, and D. Clabo, 2005: Climatological analysis of DSDs in Oklahoma as revealed by 2D-video disdrometer and polarimetric WSR-88D radar. *Preprints, 32nd Conference on Radar Meteorology*, American Meteorological Society,

Albuquerque, USA.

Seliga, T. A., and V. N. Bringi, 1978: Differential reflectivity and differential phase shift: Applications in radar meteorology. *Radio Science*, **13 (2)**, 271–275, doi:10.1029/rs013i002p00271.

Simmons, K. M., and D. Sutter, 2005: WSR-88D Radar, Tornado Warnings, and Tornado Casualties. *Weather and Forecasting*, **20 (3)**, 301–310, doi:10.1175/waf857.1.

Sinclair, V. A., D. Moisseev, and A. von Lerber, 2016: How dual-polarization radar observations can be used to verify model representation of secondary ice. *Journal of Geophysical Research: Atmospheres*, **121 (18)**, 10 954–10 970, doi:10.1002/2016jd025381.

Skamarock, W., and Coauthors, 2021: A Description of the Advanced Research WRF Model Version 4. https://opensky.ucar.edu/islandora/object/technotes:588, doi:10.5065/1dfh-6p97.

Smith, J. A., and W. F. Krajewski, 1993: A modeling study of rainfall rate-reflectivity relationships. *Water Resources Research*, **29 (8)**, 2505–2514, doi:10.1029/93wr00962.

Smyth, T. J., and A. J. Illingworth, 1998: Radar estimates of rainfall rates at the ground in bright band and non-bright band events. *Quarterly Journal of the Royal Meteorological Society*, **124 (551)**, 2417–2434, doi:10.1002/qj.49712455112.

Snook, N., Y. Jung, J. Brotzge, B. Putnam, and M. Xue, 2016: Prediction and Ensemble Forecast Verification of Hail in the Supercell Storms of 20 May 2013. *Weather and Forecasting*, **31 (3)**, 811–825, doi:10.1175/waf-d-15-0152.1.

Snyder, J. C., H. B. Bluestein, G. Zhang, and S. J. Frasier, 2010: Attenuation Correction and Hydrometeor Classification of High-Resolution, X-band, Dual-Polarized Mobile Radar Measurements in Severe Convective Storms. *Journal of Atmospheric and Oceanic Technology*, **27 (12)**, 1979–2001, doi:10.1175/2010jtecha1356.1.

Sokol, Z., J. Minářová, and O. Fišer, 2020: Hydrometeor Distribution and Linear Depolarization Ratio in Thunderstorms. *Remote Sensing*, **12 (13)**, 2144, doi:10.3390/rs12132144.

Stout, G. E., and E. A. Mueller, 1968: Survey of Relationships Between Rainfall Rate and Radar Reflectivity in the Measurement of Precipitation. *Journal of Applied Me-*

teorology, **7 (3)**, 465–474, doi:10.1175/1520-0450(1968)007⟨0465:sorbrr⟩2.0.co;2.

Straka, J. M., and E. R. Mansell, 2005: A Bulk Microphysics Parameterization with Multiple Ice Precipitation Categories. *Journal of Applied Meteorology*, **44 (4)**, 445–466, doi:10.1175/jam2211.1.

Sun, J., and N. A. Crook, 1997: Dynamical and Microphysical Retrieval from Doppler Radar Observations Using a Cloud Model and Its Adjoint. Part I: Model Development and Simulated Data Experiments. *Journal of the Atmospheric Sciences*, **54 (12)**, 1642–1661, doi:10.1175/1520-0469(1997)054⟨1642:damrfd⟩2.0.co;2.

Sánchez-Diezma, R., I. Zawadzki, and D. Sempere-Torres, 2000: Identification of the bright band through the analysis of volumetric radar data. *Journal of Geophysical Research: Atmospheres*, **105 (D2)**, 2225–2236, doi:10.1029/1999jd900310.

Tabary, P., A.-A. Boumahmoud, H. Andrieu, R. J. Thompson, A. J. Illingworth, E. Le Bouar, and J. Testud, 2011: Evaluation of two "integrated" polarimetric Quantitative Precipitation Estimation (QPE) algorithms at C-band. *Journal of Hydrology*, **405 (3-4)**, 248–260, doi:10.1016/j.jhydrol.2011.05.021.

Testud, J., E. Le Bouar, E. Obligis, and M. Ali-Mehenni, 2000: The Rain Profiling Algorithm Applied to Polarimetric Weather Radar. *Journal of Atmospheric and Oceanic Technology*, **17 (3)**, 332–356, doi:10.1175/1520-0426(2000)017⟨0332:trpaat⟩2.0.co;2.

Thompson, E. J., S. A. Rutledge, B. Dolan, V. Chandrasekar, and B. L. Cheong, 2014: A Dual-Polarization Radar Hydrometeor Classification Algorithm for Winter Precipitation. *Journal of Atmospheric and Oceanic Technology*, **31 (7)**, 1457–1481, doi:10.1175/jtech-d-13-00119.1.

Thompson, G., P. R. Field, R. M. Rasmussen, and W. D. Hall, 2008: Explicit Forecasts of Winter Precipitation Using an Improved Bulk Microphysics Scheme. Part II: Implementation of a New Snow Parameterization. *Monthly Weather Review*, **136 (12)**, 5095–5115, doi:10.1175/2008mwr2387.1.

Thompson, G., R. M. Rasmussen, and K. Manning, 2004: Explicit Forecasts of Winter Precipitation Using an Improved Bulk Microphysics Scheme. Part I: Description and Sensitivity Analysis. *Monthly Weather Review*, **132 (2)**, 519–542, doi:10.1175/1520-0493(2004)132⟨0519:efowpu⟩2.0.co;2.

Thompson, P., 1983: A History of Numerical Weather Prediction in the United

States. *Bulletin of the American Meteorological Society*, **64 (7)**, 755–764, doi:10.1175/1520-0477(1983)064⟨0730:ahopia⟩2.0.co;2.

Timothy, K. I., T. Iguchi, Y. Ohsaki, H. Horie, H. Hanado, and H. Kumagai, 1999: Test of the Specific Differential Propagation Phase Shift (KDP) Technique for Rain-Rate Estimation with a Ku-Band Rain Radar. *Journal of Atmospheric and Oceanic Technology*, **16 (8)**, 1077–1091, doi:10.1175/1520-0426(1999)016⟨1077:totsdp⟩2.0.co;2.

Trabal, J. M., E. Gorgucci, V. Chandrasekar, and D. J. McLaughlin, 2014: Evaluation of the Self-Consistency Principle for Calibration of the CASA Radar Network Using Properties of the Observed Precipitation Medium. *IEEE Transactions on Geoscience and Remote Sensing*, **52 (1)**, 149–162, doi:10.1109/tgrs.2012.2237406.

Trapp, R. J., and Coauthors, 2020: Multiple-Platform and Multiple-Doppler Radar Observations of a Supercell Thunderstorm in South America during RELAMPAGO. *Monthly Weather Review*, **148 (8)**, 3225–3241, doi:10.1175/mwr-d-20-0125.1.

Trömel, S., M. R. Kumjian, A. V. Ryzhkov, C. Simmer, and M. Diederich, 2013: Backscatter Differential Phase - Estimation and Variability. *Journal of Applied Meteorology and Climatology*, **52 (11)**, 2529–2548, doi:10.1175/jamc-d-13-0124.1.

Vaisala, 2020: Radiosonde RS41-SGP. Accessed 31 December 2021, https://www.vaisala.com/sites/default/files/documents/RS41-SGP-Datasheet-B211444EN.pdf.

Vivekanandan, J., V. Bringi, M. Hagen, and P. Meischner, 1994: Polarimetric radar studies of atmospheric ice particles. *IEEE Transactions on Geoscience and Remote Sensing*, **32 (1)**, 1–10, doi:10.1109/36.285183.

Vulpiani, G., M. Montopoli, L. D. Passeri, A. G. Gioia, P. Giordano, and F. S. Marzano, 2012: On the Use of Dual-Polarized C-Band Radar for Operational Rainfall Retrieval in Mountainous Areas. *Journal of Applied Meteorology and Climatology*, **51 (2)**, 405–425, doi:10.1175/jamc-d-10-05024.1.

Vulpiani, G., P. Tabary, J. Parent du Chatelet, and F. S. Marzano, 2008: Comparison of Advanced Radar Polarimetric Techniques for Operational Attenuation Correction at C Band. *Journal of Atmospheric and Oceanic Technology*, **25 (7)**, 1118–1135, doi:10.1175/2007jtecha936.1.

Wang, H., J. Sun, X. Zhang, X.-Y. Huang, and T. Auligné, 2013: Radar Data As-

similation with WRF 4D-Var. Part I: System Development and Preliminary Testing. *Monthly Weather Review*, **141 (7)**, 2224–2244, doi:10.1175/mwr-d-12-00168.1.

Wang, T., J. Zhu, H. Lei, Y. Shi, J. Guo, and Z. Gao, 2022: Comparison of microphysics parameterization schemes on cloud macrophysics forecasts for mixed convective-stratiform cloud events. *Atmospheric Research*, **277**, 106 284, doi:10.1016/j.atmosres.2022.106284.

Westbrook, C. D., A. J. Illingworth, E. J. O'Connor, and R. J. Hogan, 2010: Doppler lidar measurements of oriented planar ice crystals falling from supercooled and glaciated layer clouds. *Quarterly Journal of the Royal Meteorological Society*, **136 (646)**, 260–276, doi:10.1002/qj.528.

Willmarth, W. W., N. E. Hawk, and R. L. Harvey, 1964: Steady and Unsteady Motions and Wakes of Freely Falling Disks. *Physics of Fluids*, **7 (2)**, 197, doi:10.1063/1.1711133.

Wolfensberger, D., D. Scipion, and A. Berne, 2016: Detection and characterization of the melting layer based on polarimetric radar scans. *Quarterly Journal of the Royal Meteorological Society*, **142**, 108–124, doi:10.1002/qj.2672.

Xiao, Q., and Coauthors, 2008: Doppler Radar Data Assimilation in KMA's Operational Forecasting. *Bulletin of the American Meteorological Society*, **89 (1)**, 39–44, doi:10.1175/bams-89-1-39.

Yin, J., P. Hoogeboom, C. Unal, H. Russchenberg, F. van der Zwan, and E. Oudejans, 2019: UAV-Aided Weather Radar Calibration. *IEEE Transactions on Geoscience and Remote Sensing*, **57 (12)**, 10 362–10 375, doi:10.1109/tgrs.2019.2933912.

Zhang, G., and Coauthors, 2019: Current Status and Future Challenges of Weather Radar Polarimetry: Bridging the Gap between Radar Meteorology/Hydrology/Engineering and Numerical Weather Prediction. *Advances in Atmospheric Sciences*, **36 (6)**, 571–588, doi:10.1007/s00376-019-8172-4.

Zrnic, D. S., and A. Ryzhkov, 1996: Advantages of Rain Measurements Using Specific Differential Phase. *Journal of Atmospheric and Oceanic Technology*, **13 (2)**, 454–464, doi:10.1175/1520-0426(1996)013⟨0454:aormus⟩2.0.co;2.

Zrnić, D. S., N. Balakrishnan, C. L. Ziegler, V. N. Bringi, K. Aydin, and T. Matejka, 1993: Polarimetric Signatures in the Stratiform Region of a Mesoscale Con-

vective System. *Journal of Applied Meteorology*, **32 (4)**, 678–693, doi:10.1175/1520-0450(1993)032⟨0678:psitsr⟩2.0.co;2.

Appendix A

WRF options

Global attributes from WRF out file for each domain, including all the namelist options specified. Only the Thompson microphysics scheme run is shown (:MP_PHYSICS = 8), however all runs share the same options, with the exception of the microphysics.

Domain 1:

:TITLE = " OUTPUT FROM WRF V4.2.2 MODEL"
:START_DATE = "2018-01-24_00:00:00"
:SIMULATION_START_DATE = "2018-01-24_00:00:00"
:WEST-EAST_GRID_DIMENSION = 351
:SOUTH-NORTH_GRID_DIMENSION = 351
:BOTTOM-TOP_GRID_DIMENSION = 81
:DX = 10000.f
:DY = 10000.f
:AERCU_OPT = 0
:AERCU_FCT = 1.f
:IDEAL_CASE = 0
:DIFF_6TH_SLOPEOPT = 0
:AUTO_LEVELS_OPT = 2
:DIFF_6TH_THRESH = 0.1f
:DZBOT = 50.f
:DZSTRETCH_S = 1.3f
:DZSTRETCH_U = 1.1f
:SKEBS_ON = 0
:SPEC_BDY_FINAL_MU = 1
:USE_Q_DIABATIC = 0

:GRIDTYPE = ”C”
:DIFF_OPT = 1
:KM_OPT = 4
:DAMP_OPT = 0
:DAMPCOEF = 0.2f
:KHDIF = 0.f
:KVDIF = 0.f
:MP_PHYSICS = 8
:RA_LW_PHYSICS = 1
:RA_SW_PHYSICS = 1
:SF_SFCLAY_PHYSICS = 1
:SF_SURFACE_PHYSICS = 2
:BL_PBL_PHYSICS = 1
:CU_PHYSICS = 1
:SF_LAKE_PHYSICS = 0
:SURFACE_INPUT_SOURCE = 1
:SST_UPDATE = 0
:GRID_FDDA = 0
:GFDDA_INTERVAL_M = 0
:GFDDA_END_H = 0
:GRID_SFDDA = 0
:SGFDDA_INTERVAL_M = 0
:SGFDDA_END_H = 0
:HYPSOMETRIC_OPT = 2
:USE_THETA_M = 1
:GWD_OPT = 0
:SF_URBAN_PHYSICS = 1
:SF_SURFACE_MOSAIC = 0
:SF_OCEAN_PHYSICS = 1
:SHCU_PHYSICS = 0
:MFSHCONV = 0
:FEEDBACK = 1
:SMOOTH_OPTION = 0
:SWRAD_SCAT = 1.f
:W_DAMPING = 0
:DT = 30.f
:RADT = 30.f

:BLDT = 0.f
:CUDT = 5.f
:AER_OPT = 0
:SWINT_OPT = 0
:AER_TYPE = 1
:AER_AOD550_OPT = 1
:AER_ANGEXP_OPT = 1
:AER_SSA_OPT = 1
:AER_ASY_OPT = 1
:AER_AOD550_VAL = 0.12f
:AER_ANGEXP_VAL = 1.3f
:AER_SSA_VAL = 0.85f
:AER_ASY_VAL = 0.9f
:MOIST_ADV_OPT = 1
:SCALAR_ADV_OPT = 1
:TKE_ADV_OPT = 1
:DIFF_6TH_OPT = 0
:DIFF_6TH_FACTOR = 0.12f
:OBS_NUDGE_OPT = 0
:BUCKET_MM = -1.f
:BUCKET_J = -1.f
:PREC_ACC_DT = 0.f
:ISFTCFLX = 0
:ISHALLOW = 0
:ISFFLX = 1
:ICLOUD = 1
:ICLOUD_CU = 0
:TRACER_PBLMIX = 1
:SCALAR_PBLMIX = 0
:YSU_TOPDOWN_PBLMIX = 0
:GRAV_SETTLING = 0
:DFI_OPT = 0
:NTASKS_X = 8
:NTASKS_Y = 8
:NTASKS_TOTAL = 64
:SIMULATION_INITIALIZATION_TYPE = ”REAL-DATA CASE”
:WEST-EAST_PATCH_START_UNSTAG = 1

:WEST-EAST_PATCH_END_UNSTAG = 350
:WEST-EAST_PATCH_START_STAG = 1
:WEST-EAST_PATCH_END_STAG = 351
:SOUTH-NORTH_PATCH_START_UNSTAG = 1
:SOUTH-NORTH_PATCH_END_UNSTAG = 350
:SOUTH-NORTH_PATCH_START_STAG = 1
:SOUTH-NORTH_PATCH_END_STAG = 351
:BOTTOM-TOP_PATCH_START_UNSTAG = 1
:BOTTOM-TOP_PATCH_END_UNSTAG = 80
:BOTTOM-TOP_PATCH_START_STAG = 1
:BOTTOM-TOP_PATCH_END_STAG = 81
:GRID_ID = 1
:PARENT_ID = 0
:I_PARENT_START = 1
:J_PARENT_START = 1
:PARENT_GRID_RATIO = 1
:CEN_LAT = 51.145f
:CEN_LON = -1.44101f
:TRUELAT1 = 51.145f
:TRUELAT2 = 51.145f
:MOAD_CEN_LAT = 51.145f
:STAND_LON = -1.441f
:POLE_LAT = 90.f
:POLE_LON = 0.f
:GMT = 0.f
:JULYR = 2018
:JULDAY = 24
:MAP_PROJ = 1
:MAP_PROJ_CHAR = ”Lambert Conformal”
:MMINLU = ”MODIFIED_IGBP_MODIS_NOAH”
:NUM_LAND_CAT = 21
:ISWATER = 17
:ISLAKE = 21
:ISICE = 15
:ISURBAN = 13
:ISOILWATER = 14
:HYBRID_OPT = 2

:ETAC = 0.2f

Domain 2:

:TITLE = " OUTPUT FROM WRF V4.2.2 MODEL"
:START_DATE = "2018-01-24_00:00:00"
:SIMULATION_START_DATE = "2018-01-24_00:00:00"
:WEST-EAST_GRID_DIMENSION = 401
:SOUTH-NORTH_GRID_DIMENSION = 401
:BOTTOM-TOP_GRID_DIMENSION = 81
:DX = 2000.f
:DY = 2000.f
:AERCU_OPT = 0
:AERCU_FCT = 1.f
:IDEAL_CASE = 0
:DIFF_6TH_SLOPEOPT = 0
:AUTO_LEVELS_OPT = 2
:DIFF_6TH_THRESH = 0.1f
:DZBOT = 50.f
:DZSTRETCH_S = 1.3f
:DZSTRETCH_U = 1.1f
:SKEBS_ON = 0
:SPEC_BDY_FINAL_MU = 1
:USE_Q_DIABATIC = 0
:GRIDTYPE = "C"
:DIFF_OPT = 1
:KM_OPT = 4
:DAMP_OPT = 0
:DAMPCOEF = 0.2f
:KHDIF = 0.f
:KVDIF = 0.f
:MP_PHYSICS = 8
:RA_LW_PHYSICS = 1
:RA_SW_PHYSICS = 1
:SF_SFCLAY_PHYSICS = 1
:SF_SURFACE_PHYSICS = 2
:BL_PBL_PHYSICS = 1

:CU_PHYSICS = 0
:SF_LAKE_PHYSICS = 0
:SURFACE_INPUT_SOURCE = 1
:SST_UPDATE = 0
:GRID_FDDA = 0
:GFDDA_INTERVAL_M = 0
:GFDDA_END_H = 0
:GRID_SFDDA = 0
:SGFDDA_INTERVAL_M = 0
:SGFDDA_END_H = 0
:HYPSOMETRIC_OPT = 2
:USE_THETA_M = 1
:GWD_OPT = 0
:SF_URBAN_PHYSICS = 1
:SF_SURFACE_MOSAIC = 0
:SF_OCEAN_PHYSICS = 1
:SHCU_PHYSICS = 0
:MFSHCONV = 0
:FEEDBACK = 1
:SMOOTH_OPTION = 0
:SWRAD_SCAT = 1.f
:W_DAMPING = 0
:DT = 6.f
:RADT = 30.f
:BLDT = 0.f
:CUDT = 5.f
:AER_OPT = 0
:SWINT_OPT = 0
:AER_TYPE = 1
:AER_AOD550_OPT = 1
:AER_ANGEXP_OPT = 1
:AER_SSA_OPT = 1
:AER_ASY_OPT = 1
:AER_AOD550_VAL = 0.12f
:AER_ANGEXP_VAL = 1.3f
:AER_SSA_VAL = 0.85f
:AER_ASY_VAL = 0.9f

:MOIST_ADV_OPT = 1
:SCALAR_ADV_OPT = 1
:TKE_ADV_OPT = 1
:DIFF_6TH_OPT = 0
:DIFF_6TH_FACTOR = 0.12f
:OBS_NUDGE_OPT = 0
:BUCKET_MM = -1.f
:BUCKET_J = -1.f
:PREC_ACC_DT = 0.f
:ISFTCFLX = 0
:ISHALLOW = 0
:ISFFLX = 1
:ICLOUD = 1
:ICLOUD_CU = 0
:TRACER_PBLMIX = 1
:SCALAR_PBLMIX = 0
:YSU_TOPDOWN_PBLMIX = 0
:GRAV_SETTLING = 0
:DFI_OPT = 0
:NTASKS_X = 8
:NTASKS_Y = 8
:NTASKS_TOTAL = 64
:SIMULATION_INITIALIZATION_TYPE = ”REAL-DATA CASE”
:WEST-EAST_PATCH_START_UNSTAG = 1
:WEST-EAST_PATCH_END_UNSTAG = 400
:WEST-EAST_PATCH_START_STAG = 1
:WEST-EAST_PATCH_END_STAG = 401
:SOUTH-NORTH_PATCH_START_UNSTAG = 1
:SOUTH-NORTH_PATCH_END_UNSTAG = 400
:SOUTH-NORTH_PATCH_START_STAG = 1
:SOUTH-NORTH_PATCH_END_STAG = 401
:BOTTOM-TOP_PATCH_START_UNSTAG = 1
:BOTTOM-TOP_PATCH_END_UNSTAG = 80
:BOTTOM-TOP_PATCH_START_STAG = 1
:BOTTOM-TOP_PATCH_END_STAG = 81
:GRID_ID = 2
:PARENT_ID = 1

:I_PARENT_START = 135
:J_PARENT_START = 135
:PARENT_GRID_RATIO = 5
:CEN_LAT = 51.05497f
:CEN_LON = -1.584106f
:TRUELAT1 = 51.145f
:TRUELAT2 = 51.145f
:MOAD_CEN_LAT = 51.145f
:STAND_LON = -1.441f
:POLE_LAT = 90.f
:POLE_LON = 0.f
:GMT = 0.f
:JULYR = 2018
:JULDAY = 24
:MAP_PROJ = 1
:MAP_PROJ_CHAR = ”Lambert Conformal”
:MMINLU = ”MODIFIED_IGBP_MODIS_NOAH”
:NUM_LAND_CAT = 21
:ISWATER = 17
:ISLAKE = 21
:ISICE = 15
:ISURBAN = 13
:ISOILWATER = 14
:HYBRID_OPT = 2
:ETAC = 0.2f

Domain 3:

:TITLE = “ OUTPUT FROM WRF V4.2.2 MODEL”
:START_DATE = ”2018-01-24_00:00:00”
:SIMULATION_START_DATE = ”2018-01-24_00:00:00”
:WEST-EAST_GRID_DIMENSION = 501
:SOUTH-NORTH_GRID_DIMENSION = 501
:BOTTOM-TOP_GRID_DIMENSION = 81
:DX = 400.f
:DY = 400.f
:AERCU_OPT = 0

:AERCU_FCT = 1.f
:IDEAL_CASE = 0
:DIFF_6TH_SLOPEOPT = 0
:AUTO_LEVELS_OPT = 2
:DIFF_6TH_THRESH = 0.1f
:DZBOT = 50.f
:DZSTRETCH_S = 1.3f
:DZSTRETCH_U = 1.1f
:SKEBS_ON = 0
:SPEC_BDY_FINAL_MU = 1
:USE_Q_DIABATIC = 0
:GRIDTYPE = ”C”
:DIFF_OPT = 1
:KM_OPT = 4
:DAMP_OPT = 0
:DAMPCOEF = 0.2f
:KHDIF = 0.f
:KVDIF = 0.f
:MP_PHYSICS = 8
:RA_LW_PHYSICS = 1
:RA_SW_PHYSICS = 1
:SF_SFCLAY_PHYSICS = 1
:SF_SURFACE_PHYSICS = 2
:BL_PBL_PHYSICS = 1
:CU_PHYSICS = 0
:SF_LAKE_PHYSICS = 0
:SURFACE_INPUT_SOURCE = 1
:SST_UPDATE = 0
:GRID_FDDA = 0
:GFDDA_INTERVAL_M = 0
:GFDDA_END_H = 0
:GRID_SFDDA = 0
:SGFDDA_INTERVAL_M = 0
:SGFDDA_END_H = 0
:HYPSOMETRIC_OPT = 2
:USE_THETA_M = 1
:GWD_OPT = 0

:SF_URBAN_PHYSICS = 1
:SF_SURFACE_MOSAIC = 0
:SF_OCEAN_PHYSICS = 1
:SHCU_PHYSICS = 0
:MFSHCONV = 0
:FEEDBACK = 1
:SMOOTH_OPTION = 0
:SWRAD_SCAT = 1.f
:W_DAMPING = 0
:DT = 1.2f
:RADT = 30.f
:BLDT = 0.f
:CUDT = 5.f
:AER_OPT = 0
:SWINT_OPT = 0
:AER_TYPE = 1
:AER_AOD550_OPT = 1
:AER_ANGEXP_OPT = 1
:AER_SSA_OPT = 1
:AER_ASY_OPT = 1
:AER_AOD550_VAL = 0.12f
:AER_ANGEXP_VAL = 1.3f
:AER_SSA_VAL = 0.85f
:AER_ASY_VAL = 0.9f
:MOIST_ADV_OPT = 1
:SCALAR_ADV_OPT = 1
:TKE_ADV_OPT = 1
:DIFF_6TH_OPT = 0
:DIFF_6TH_FACTOR = 0.12f
:OBS_NUDGE_OPT = 0
:BUCKET_MM = -1.f
:BUCKET_J = -1.f
:PREC_ACC_DT = 0.f
:ISFTCFLX = 0
:ISHALLOW = 0
:ISFFLX = 1
:ICLOUD = 1

:ICLOUD_CU = 0
:TRACER_PBLMIX = 1
:SCALAR_PBLMIX = 0
:YSU_TOPDOWN_PBLMIX = 0
:GRAV_SETTLING = 0
:DFI_OPT = 0
:NTASKS_X = 8
:NTASKS_Y = 8
:NTASKS_TOTAL = 64
:SIMULATION_INITIALIZATION_TYPE = ”REAL-DATA CASE”
:WEST-EAST_PATCH_START_UNSTAG = 1
:WEST-EAST_PATCH_END_UNSTAG = 500
:WEST-EAST_PATCH_START_STAG = 1
:WEST-EAST_PATCH_END_STAG = 501
:SOUTH-NORTH_PATCH_START_UNSTAG = 1
:SOUTH-NORTH_PATCH_END_UNSTAG = 500
:SOUTH-NORTH_PATCH_START_STAG = 1
:SOUTH-NORTH_PATCH_END_STAG = 501
:BOTTOM-TOP_PATCH_START_UNSTAG = 1
:BOTTOM-TOP_PATCH_END_UNSTAG = 80
:BOTTOM-TOP_PATCH_START_STAG = 1
:BOTTOM-TOP_PATCH_END_STAG = 81
:GRID_ID = 3
:PARENT_ID = 2
:I_PARENT_START = 150
:J_PARENT_START = 150
:PARENT_GRID_RATIO = 5
:CEN_LAT = 51.03695f
:CEN_LON = -1.61264f
:TRUELAT1 = 51.145f
:TRUELAT2 = 51.145f
:MOAD_CEN_LAT = 51.145f
:STAND_LON = -1.441f
:POLE_LAT = 90.f
:POLE_LON = 0.f
:GMT = 0.f
:JULYR = 2018

:JULDAY = 24
:MAP_PROJ = 1
:MAP_PROJ_CHAR = ”Lambert Conformal”
:MMINLU = ”MODIFIED_IGBP_MODIS_NOAH”
:NUM_LAND_CAT = 21
:ISWATER = 17
:ISLAKE = 21
:ISICE = 15
:ISURBAN = 13
:ISOILWATER = 14
:HYBRID_OPT = 2
:ETAC = 0.2f